공학박사 학위논문

Development of Dynamic LES-SPH Method for Thermal Ablation Analysis with Turbulent Natural Convection

전이 및 난류 자연 대류 유동을 동반한 열적 침식 해석을 위한 입자법 기반 동적 대와류 모델 개발

2023 년 8 월

서울대학교 대학원

에너지시스템공학부

최 태 수

Development of Dynamic LES-SPH Method for Thermal Ablation Analysis with Turbulent Natural Convection

전이 및 난류 자연 대류 유동을 동반한 열적 침식 해석을 위한
입자법 기반 동적 대와류 모델 개발

지도 교수 김 응 수

이 논문을 공학박사 학위논문으로 제출함

2023 년 8 월

서울대학교 대학원

에너지시스템공학부

최 태 수

최태수의 박사 학위논문을 인준함

2023 년 8 월

위 원 장 조 형 규 (인)

부위원장 김 응 수 (인)

위 원 박 현 선 (인)

위 원 정 재 호 (인)

위 원 이 연 건 (인)

Abstract

Development of Dynamic LES-SPH Method for Thermal Ablation Analysis with Turbulent Natural Convection

Tae Soo Choi
Department of Energy System Engineering
The Graduate School
Seoul National University

The primary objective in nuclear severe accident mitigation strategies is to retain and efficiently cool corium to prevent the release of fission products. However, the decay heat generated from corium can lead to thermal ablation of the pressure boundary, compromising structural integrity and potentially leading to the release of fission product into the environment. Prominent examples include RPV ablation in IVR-ERVC strategy, concrete structure breaching in MCCI and thermal erosion of sacrificial material caused by corium jet impingement above core-catcher. The extent of thermal ablation is determined by the flow characteristics of corium and heat flux at boundary. Therefore, a comprehensive understanding of thermal ablation and the behavior of corium is crucial from a severe accident mitigation perspective.

The analysis of turbulent natural convection behavior of corium and thermal ablation has been based on empirical approaches using simulant experiments or conventional computational fluid dynamics (CFD). Researches has been conducted to refine and validate of turbulence models for analyzing the behavior of corium flow, and recently, comprehensive analysis incorporating grid-based phase

change analysis has been carried out. Numerical assumptions have been introduced, to simulate phenomena such as transient interface tracking between corium layers and domain deformation due to phase change.

With advancements in hardware and software for large-scale parallel computing, particle-based CFD methods, such as Smoothed Particle Hydrodynamics (SPH), have been applied to nuclear safety analysis. The particle-based CFD methods analyze flow using moving particles with physical quantities making it suitable for analyzing multi-phase, multi-fluid, free surface and phase change effectively.

Thermal ablation and corium thermal flow involve solid-liquid phase change and multi-fluid heat transfer analysis, making the particle-based CFD an effective framework by utilizing advanced phase change model. However, there has been no cases of analysis using sophisticated turbulence models based on particle-based CFD, and therefore, no research on thermal ablation accompanied by turbulent thermal flow.

Therefore, in this study, a turbulence model applicable to transient laminar, transitional, and turbulent flow conditions was developed based on Smoothed Particle Hydrodynamics (SPH), which is a representative particle-based fluid analysis method. By combining the common features of SPH, which uses spatial weight functions, and Large Eddy Simulation (LES), which utilizes spatial filter functions for modeling turbulent flow, a dynamic LES-SPH framework was developed without additional filtering processes. Numerical corrections were applied to SPH discretization to ensure the LES models' numerical accuracy when analyzing low Prandtl number fluids, such as corium and liquid metals. Turbulent Prandtl number modeling and the dynamic Vreman model were introduced for this purpose. The capabilities of the developed dynamic LES-SPH model to analyze thermal flow under transitional and turbulent conditions were validated through comparisons with various numerical and experimental studies.

Furthermore, an advanced phase change model based on the Enthalpy-

Porosity Model (EPM) was developed to analyze thermal ablation using the SPH method. By incorporating the assumption of porosity effects in the momentum equation, the EPM enabled the analysis of phase change without the need for numerical modification related to viscosity and other properties. The developed SPH phase change model was validated through comparisons with various numerical and experimental studies, confirming its capability to analyze phase interfaces and heat transfer.

To demonstrate the utility of the developed LES-SPH with phase change model, an analysis was conducted on the behavior of corium pool and the thermal ablation of the pressure vessel under in-vessel retention conditions. The thermal ablation of the pressure vessel at different times and locations was compared to CFD and previous SPH approaches. The analysis results confirmed that the dynamic LES-SPH and phase change models developed in this study effectively analyze turbulent corium flow accompanied by thermal ablation.

The particle-based LES-SPH phase change framework developed in this study provides an analysis methodology for phenomena that were difficult to analyze using conventional CFD in the context of nuclear severe accidents. It is expected to complement conventional CFD methods and provide a more comprehensive understanding. Furthermore, rigorous validation and analysis of the developed LES-SPH and phase change models will be conducted to ensure their reliability. This will facilitate the improvement and proposal of correlations in areas without experimental data related to nuclear severe accidents, contributing to the field of nuclear safety.

Keywords : Smoothed Particle Hydrodynamics, Dynamic Large Eddy Simulation, Thermal Ablation, Turbulence, Phase Change
Student Number : 2015-21333

List of Contents

List of Tables

List of Figures

Chapter 1 Introduction

1.1. Background and Motivation

Thermal ablation is a crucial physical phenomenon that requires accurate understanding for maintaining structural integrity in the event of a severe nuclear accident. Decay heat generated in the corium is transferred to the boundaries through corium thermal flow, resulting phase changes within the corium retention structure. Notable safety issues related to thermal ablation include the Reactor Pressure Vessel (RPV) ablation in the In-Vessel Retention and External Reactor Vessel Cooling (IVR-ERVC) strategy, thermal ablation of the concrete basemat due to decay heat and chemical reactions in Molten Core Concrete Interaction (MCCI) phenomena, and core-catcher thermal ablation resulting from corium jet impingement in the Sodium Fast Reactor (SFR) and European PWRs during severe accident scenario.

Thermal ablation in the IVR-ERVC strategy directly contributes to the degradation of RPV integrity, which is highlighted as a significant factor for the success of the IVR-ERVC strategy in the Phenomena Identification and Ranking Table (PIRT) proposed by the IVMR project (Fichot, 2020). The heat flux at the boundaries, which leads to RPV ablation, is highly dependent on the composition and flow characteristics of the corium flow (Rempe, 2008), and the governing parameter which determine the flow characteristics include the Rayleigh number (Ra), Prandtl number (Pr), and aspect ratio (Park, 2012). Under fully developed corium natural convection, the Ra number for the oxide pool ranges from 10^{15} to 10^{16}, and for the metal layer, it ranges from 10^{9} to 10^{10}. Experimental studies

conducted under these high *Ra* conditions have confirmed the presence of non-uniform eddies of varying size, position, and number over time, resulting from buoyancy-driven natural convection induced by the internal heat source. (Jahn, 1974).

In MCCI, thermal ablation occurs due to decay heat from the corium pool and chemical reactions with concrete, leading to breaches in the concrete structure and potential release of corium. The heat transfer mechanism within the corium pool during MCCI is influenced by the agitation of the corium pool by gas bubbles generated from chemical reactions. Additionally, the heat transfer coefficient between concrete and corium depends on the flow conditions in the gas film between them (Bradley, 1992).

In the event of a severe accident in Sodium Fast Reactor (SFR) and European PWRs, the core catcher, which is introduced to prevent re-criticality and maintain the structural integrity of the vessel, can experience thermal ablation due to the impingement of turbulent corium jet. To improve the core catcher's ability to withstand extreme heat fluxes from corium, a sacrificial material layer is placed on the device surface (Czarny, 2022) and the extent of ablation is determined by the heat transfer characteristics and crust formation during the turbulent corium jet's laminarization process (Saito, 1990).

Therefore, accurate modeling and comprehensive analysis of thermal ablation and corium flow are essential to enhance the understanding of these nuclear safety issues.

Particle based Computational Fluid Dynamics (CFD) method have demonstrated their capabilities in analyzing complex phenomena characterized by large domain deformations, including multi-phase flow, phase change and free

surface analysis. These strengths have prompted their application in the field of nuclear safety (Jo et al., 2019; Park et al., 2020; Jo et al., 2021). However, despite their potential, the utilization of particle-based CFD method for addressing the nuclear safety issues such as IVR-ERVC and MCCI is confronted with certain limitations. These limitations stem from the absence of sophisticated turbulence models capable of capturing corium flow under high *Ra* number condition, as well as the large computational cost associated with particle based CFD method.

Motivated by the need to overcome these challenges, this study aims to develop an advanced turbulence model based on particle-based CFD, coupled with a phase change model. This integrated approach is intended to effectively resolve the intricacies of transition and turbulent natural convection, thereby providing a robust framework for analyzing thermal ablation phenomena. To accomplish this objective, an in-house code was developed by integrating the Lagrangian-based Smoothed Particle Hydrodynamics (SPH) method with dynamic LES model and phase change model.

The developed LES-SPH model is expected to complement conventional CFD method, which face difficulties in analyzing flows with significant deformation. Furthermore, it can expand the range of flow phenomena that can be analyzed using particle-based CFD, such as turbulence and phase change. Moreover, this validated LES-SPH model will contribute to the field of thermal hydrodynamics modeling for severe accident analysis by conducting numerical experiments under conditions that are difficult to be carried out at the laboratory scale.

1.2. Previous Researches

1.2.1. Numerical Studies on Phase Change

The research of phase change and thermal ablation using conventional CFD and SPH method has been summarized in Table 1.1. In conventional CFD approaches, the enthalpy-porosity model has been introduced to simulate phase change interface with a fixed computational domain. Furthermore, in order to calculate the heat flux transferred by turbulent thermal flow at the phase boundary, the Low Reynolds Number (LRN) Reynolds-Averaged Navier-Stokes (RANS) models have been employed. (Amidu, 2021; Harish, 2022; Najafabadi, 2022)

On the other hand, in research employing the SPH method for phase change analysis, the phase of particles is determined based on their temperature or enthalpy. Farrokhpanah (2017) proposed a temperature-based phase change model and accounted for latent heat by modeling the heat capacity. On the other hand, Wang (2020) proposed an enthalpy-based method to determine the phase of SPH particles. This research focused on the thermal ablation analysis accompanied by laminar natural convection in 2D rectangular geometry. Other research, such as those by Russel (2018) and Cummins (2021), investigated the behavior of molten metal induced by laser fusion, while Jeske (2022) studied the solidification process of liquid droplets.

However, these studies analyze the behavior of particles undergoing phase change by modeling properties such as viscosity and thermal conductivity based on the extent of phase change. Additionally, it is important to note that these studies were limited to analyzing ablation with laminar thermal flow, as SPH method lacked a LRN turbulence model.

1.2.2. Turbulent-SPH Model

Turbulent flow modeling studies using the SPH method have been conducted in the field of ocean engineering, specifically in areas such as the dam break, wave breaking, and solitary wave analysis. Table 1.2 provides a list of some studies employing the turbulent-SPH model.

All the studies utilizing the Reynolds Averaged Navier Stokes (RANS) model employed the Standard k-ε model. Violeau (2007), Lopez (2010), and Ran (2015) conducted single-phase flow analysis, including the free surface. Fonty (2020) conducted a two-phase analysis to investigate air entrainment. Studies using the Large Eddy Simulation (LES) model employed the standard Smagorinsky model. Darlymple (2006) and Tripepi (2020) performed three-dimensional analysis of dam-break and solitary waves. Zhang (2021) focused on the analysis of landslide-generated waves and validated the results through pressure and velocity against experimental measurements.

However, the standard k-ε and Smagorinsky model have limitations in modeling the turbulent effect in laminar/transition flows and directly resolving the flow within boundary layers, as well as in capturing the turbulence characteristics in turbulent natural convection with high Ra number condition.

On the other hand, in the mesh-based CFD method, sophisticated turbulence models have been introduced and verified. In the study of Dinh (1997), the LRN k-ε model was used to analyze the flow of COPO experiments (Kymalainen, 1994), and the analysis revealed an underprediction of the upward heat transfer rate and an overprediction of lateral heat transfer rate. Due to the assumption of isotropic turbulence, the vertical turbulent effects are overdamped when temperature and flow stratify in high Ra number condition, while the lateral turbulent effects are amplified.

By incorporating turbulent heat transfer modeling based on the local Richardson number (Ri), an improved LRN k-ε model was able to achieve accurate analysis. In Fukasawa's study (2008) on BALI experiment (Bonnet, 1994), a flow field stratified by buoyancy force, the Murakami-Kato-Chikamoto (MKC) model or Abe-Nagano-Kondo (ANK) model, which is a k-ε model based on the Kolmogorov velocity scale rather than the friction velocity scale, was employed to capture the vertical turbulent effects that are over-damped by buoyancy.

In the research using LES models, Lau's study (2012) validated the performance of various Sub-Grid Scale (SGS) models for turbulent natural convection occurring in a tall cavity. The center of tall cavity exhibits strong stratification of temperature and flow filed, while near the heated/cooled walls, a complex transient flow of laminar-to-turbulent transition and re-laminarization occurs on the top lid. The analysis results using the dynamic Vreman model and dynamic Smagorinsky model demonstrated universality and accuracy compared to the standard Smagorinsky model. Another study on tall cavity natural convection by Whang (2021) also confirmed the accuracy of the dynamic Vreman model compared to the standard Smagorinsky model in terms of heat transfer characteristics near the heated wall and development of turbulent flow.

Therefore, for the development of turbulence-SPH model, it is necessary to utilize an advanced RANS or LES model that is suitable for analyzing high Ra natural convection and transient flow structure, and integrate it effectively with SPH method.

1.3. Objective and Scope

The purpose of this study is to develop a turbulence SPH code with phase change model which can handle the thermal ablation accompanying transition and

turbulent natural convection. Through the development of a discretization method for the dynamic LES model, a dynamic LES-SPH code capable of analyzing a wide range of flow conditions was developed. The development and improvement of a phase change model optimized for the explicit SPH solver was carried out, and integration with the dynamic LES-SPH model was achieved. The developed code was applied to the analysis of corium behavior and RPV ablation under IVR-ERVC condition.

Chapter 2 describes the SPH method, and its numerical scheme and algorithm used in this study. Chapter 3 covers the developments and validation of the dynamic LES-SPH model. In Chapter 4, the development and refinement of phase change model using SPH method are described. Finally, in Chapter 5, simulation results and discussions for the corium behavior and RPV ablation under IVR-ERVC are covered.

Table 1.1 CFD researches on Thermal Ablation and Phase change

Author	CFD Methodology	Dim	Turbulence Model	Mushy zone Treatment
Liang (2020)	Mesh-based CFD	2D	$k - l_m$	X
Amidu (2021)	Mesh-based CFD	2D	SST $k - \omega$	Enthalpy-Porosity
Harish (2022)	Mesh-based CFD	3D	LRN Lam-Bremhorst $k - \varepsilon$	Enthalpy -porosity
Najafabadi (2022)	Mesh-based CFD	3D	LRN $k - \varepsilon$	Enthalpy -porosity
Farrokhpanah (2017)	SPH	2D/3D	X	X
Russel (2018)	SPH	2D	X	X
Wang (2020)	SPH	2D	X	X
Cummins (2021)	SPH	3D	X	X
Jeske (2022)	SPH	3D	X	Enthalpy -porosity

Table 1.2. Previous SPH researches on turbulence model

Author	Phenomenon	Dim	Turbulence Model
Violeau (2007)	Channel Flow	3D	Standard Smagorinsky Model
	Dam-Break	2D/3D	Standard $k-\varepsilon$ model
Lopez (2010)	Hydraulic Jump	2D	Standard $k-\varepsilon$ model
Ran (2015)	Wave breaking Dam-break	2D	Standard $k-\varepsilon$ model
Fonty (2020)	Air entrainment	3D	Standard $k-\varepsilon$ model
Dalrymple (2006)	Flow overtopping Dam-break	3D	Standard Smagorinsky Model
Tripepi (2020)	Solitary wave	3D	Standard Smagorisnky Model
Zhang (2021)	Landslide generated waves	2D	Standard Smagorisnky Model

Chapter 2 Smoothed Particle Hydrodynamics

2.1. Smoothed Particle Hydrodynamics

Smoothed Particle Hydrodynamics (SPH) is a particle based computational fluid analysis (CFD) method widely used for flow analysis. SPH method analyzes the flow with SPH particles moving with fluid properties, making it particularly suitable for multi-phase and multi-fluid analysis involving large deformations and instantaneous phase interface changes as shown in Figure 2.1. After initial application to astrophysics field (Gingold, 1977), SPH method has been utilized in various fields such as marine engineering (Roger, 2008), structure analysis (Chen, 1996), and nuclear engineering (Jo, 2019) due to its ability to handle complex flow phenomena.

2.1.1. Basic Concept of SPH

The SPH method is an interpolation approach that utilizes neighboring particles and volume weighting function to discretize any function f in SPH formulation. This method is derived from approximating the integral of the Dirac delta function in the continuum, as shown in Figure 2.2. The integral interpolant of a function f is represented by Equation 2.1. This equation incorporates the bell-shaped kernel function W, known as the weighting function, and kernel length h.

$$f(\boldsymbol{r}) = \int f(\boldsymbol{r}')W(\boldsymbol{r} - \boldsymbol{r}', h)d\boldsymbol{r}' \tag{2.1}$$

2.1.2. SPH Discretization

As the analysis domain can be discretized into finite SPH particles, the integral interpolant of the SPH method can be written as Equation 2.2. Where subscript i and j denote the center and neighbor particle, respectively, while m and ρ represent the mass and density of an SPH particle.

$$f(\boldsymbol{r_i}) = \sum_j \frac{m_j}{\rho_j} f(\boldsymbol{r}_j) W(\boldsymbol{r}_i - \boldsymbol{r_j}, h) \tag{2.2}$$

The first and second spatial derivative forms of the arbitrary function f are approximated by the spatial gradient of the kernel function (Monaghan, 1992). The governing equations are discretized into SPH formulation in terms of Equation 2.3 and 2.4. Where $\nabla W_{ij} = \partial W(\boldsymbol{r_i} - \boldsymbol{r_j}, h)/\partial \boldsymbol{r_i}$, and $\boldsymbol{r}_{ij} = \boldsymbol{r}_i - \boldsymbol{r}_j$, which is the position vector of the neighbor particle.

$$\nabla f(\boldsymbol{r}_i) = \sum_j \frac{m_j}{\rho_j} \{f(\boldsymbol{r}_j) + f(\boldsymbol{r}_i)\} \nabla W_{ij} \tag{2.3}$$

$$\nabla^2 f(\boldsymbol{r_i}) = \sum_j 2 \frac{m_j}{\rho_j} \left(f(\boldsymbol{r}_i) - f(\boldsymbol{r}_j)\right) \frac{\boldsymbol{r_{ij}} \cdot \nabla W_{ij}}{\left|\boldsymbol{r}_{ij}\right|^2} \tag{2.4}$$

2.1.3. SPH Consistency and Accuracy

The accuracy of SPH discretization depends on factors such as particle distribution, the type of kernel function, and spatial resolution. (Fatehi, 2011) When the following conditions are met, the SPH discretization inherently achieves second-order accuracy:

- *Compactness condition*: The kernel function assigns weighting value within compact domain
- *Unity condition*: The integral of the weighing value within a compact domain should be equal to 1.0.
- *Symmetric condition*: The kernel function should exhibit symmetry.
- *Monotonically decaying*: The weights assigned by the kernel function should monotonically decrease as the distance from the center SPH particle increases.
- *Regular SPH particle distribution*: The SPH particles should be distributed in a regular manner across the analysis domain.

2.1.4. Nearest Neighboring Particle Searching (NNPS)

In SPH method, the flow analysis is carried out by using the position and physical quantities of neighbor particles. Therefore, the searching process for nearby particles are necessary at each time step, and employing a more efficient approach for Nearest Neighboring Particle Searching (NNPS) can result in significant computational cost saving. Since the kernel function has limited support domain, only a finite number of particles exist within the support domain of the center particle and contribute the SPH interpolation. In this study, the linked-list search algorithm is utilized for NNPS (Mao, 2017). To implement this algorithm, a cell structure is superimposed on the analysis domain as depicted in Figure 2.3. The linked-list algorithm enables the assignment of each SPH particles to a specific cell. For a given center particle i, its NNPS can only include particles within the same cell or in adjacent cells.

2.2. Governing Equation

The governing equations for analyzing incompressible turbulent thermal flow are comprised of the momentum and energy transfer equations. Since the flow is analyzed by utilizing moving SPH particles with physical quantities, the governing equations are discretized from a Lagrangian perspective.

2.2.1. Momentum Equation

The Navier-Stokes equation, as shown in Equation 2.5, is used for analyzing incompressible flow, where f_b represents the body force. The right-hand side (RHS) of the Equation 2.5 is discretized as Equation 2.6 and 2.7, where superscripts fp and fv denote pressure gradient force and viscous force. $\boldsymbol{u}_{ij}$ is the relative velocity between a center and neighbor particle.

$$\frac{D\boldsymbol{u}}{Dt} = -\frac{\nabla P}{\rho} + \frac{\mu_{eff}}{\rho}\nabla^2\boldsymbol{u} + \boldsymbol{f_b} \tag{2.5}$$

$$\left(\frac{d\boldsymbol{u}}{dt}\right)_i^{fp} = -\sum_j \frac{m_j}{\rho_i\rho_j}(P_i + P_j)\nabla W_{ij} \tag{2.6}$$

$$\left(\frac{d\boldsymbol{u}}{dt}\right)_i^{fv} = -\sum_j \frac{m_j}{\rho_i\rho_j}\frac{4\mu_{i,eff}\mu_{j,eff}}{\mu_{i,eff} + \mu_{j,eff}}\boldsymbol{u}_{ij}\frac{\boldsymbol{r}_{ij}\cdot\nabla W_{ij}}{|\boldsymbol{r}_{ij}|^2} \tag{2.7}$$

$\mu_{i,eff}$ is effective dynamic viscosity that consist of dynamic viscosity(μ_i) and eddy viscosity ($\mu_{i,t}$) as Equation 2.8

$$\mu_{i,eff} = \mu_i + \mu_{t,i} \tag{2.8}$$

2.2.2. Energy Equation

In this study, the analysis includes enthalpy-based phase change models. The energy transfer equation is given by Equation 2.9.

$$\frac{Dh}{Dt} = \frac{k_{eff}}{\rho}\nabla^2 T + S_h \tag{2.9}$$

The SPH discretization for energy transfer equation is given by Equation 2.10. Where h, k, T and S_h denote the specific enthalpy, thermal conductivity, temperature, and heat source, respectively. Effective thermal conductivity is modelled with turbulent model and detailed turbulent models are described in Chapter 2.5.

$$\left(\frac{Dh}{Dt}\right)_i = \sum_j \frac{m_j}{\rho_i \rho_j} \frac{4k_{i,eff}k_{j,eff}}{k_{i,eff} + k_{j,eff}} (T_i - T_j) \frac{\boldsymbol{r}_{ij} \cdot \nabla W_{ij}}{\left|\boldsymbol{r}_{ij}\right|^2} + S_h \tag{2.10}$$

2.3. Explicit Incompressible SPH

The Explicit Incompressible SPH (EISPH) is an approach that explicitly analyze the Pressure Poisson Equation (PPE), offering advantages such as no large-scale matrix operation and ease of parallelization calculation using GPGPUs. Compared to Weakly Compressible SPH (WCSH), EISPH enables stable pressure field computation even with larger time steps, making it effective in reducing the computational load (Daly, 2016) of LES-SPH methods that demand high spatial resolutions.

2.3.1. Projection Time Integration

The EISPH solver utilizes the projection time integration method

(Cummins, 1999) to analyze PPE and obtain the pressure field. The Navier-stokes equation is divided into projection and correction step as Equation 2.11. During projection step, the momentum updates caused by accelerations other than pressure gradient force are computed to determine the projected position and velocity as indicated in Equation 2.12 and 2.13, Here, the superscripts pr, n, and $n+1$ denote the projection step, current time step, and next time step, respectively.

$$\frac{Du}{Dt} = \frac{D(u^{n+1} - u^{pr}) + (u^{pr} - u^{n})}{Dt} = -\frac{1}{\rho}\nabla P + \nu\nabla^2 u + f_b \tag{2.11}$$

$$\boldsymbol{u^{pr}} = \boldsymbol{u^{n}} + \Delta t\left\{\left(\frac{d\boldsymbol{u}}{dt}\right)_i^{fv} + \left(\frac{d\boldsymbol{u}}{dt}\right)_i^{fb}\right\} \tag{2.12}$$

$$\boldsymbol{r^{pr}} = \boldsymbol{r^{n}} + \Delta t\boldsymbol{u}^{pr} \tag{2.13}$$

Based on the projection velocity and position, the PPE is solved to obtain the pressure field that guarantees incompressibility of the SPH particles as shown in Equation 2.14 and 2.15.

$$\frac{D\left(\boldsymbol{u^{n+1}} - \boldsymbol{u^{pr}}\right)}{Dt} = \left(\frac{d\boldsymbol{u}}{dt}\right)_i^{fp} \tag{2.14}$$

$$\frac{-\nabla \cdot \boldsymbol{u^{pr}}}{\Delta t} = -\frac{1}{\rho}\nabla^2 P \tag{2.15}$$

By calculating the pressure gradient force term from the pressure field ensuring incompressibility, the position and velocity of SPH particles are updated in the correction step, as given Equation 2.16 and 2.17.

$$\nabla \boldsymbol{u}^{\boldsymbol{n+1}} = \boldsymbol{u}^{\boldsymbol{pr}} + \Delta t \left(\frac{d\boldsymbol{u}}{dt}\right)_i^{fp} \tag{2.16}$$

$$\boldsymbol{r}^{\boldsymbol{n+1}} = \boldsymbol{r}^{\boldsymbol{n}} + \Delta t\left(\boldsymbol{u}^{\boldsymbol{n}} + \boldsymbol{u}^{\boldsymbol{n+1}}\right)/2 \tag{2.17}$$

2.3.2. Explicit PPE Analysis in SPH Formulation

In the Explicit Incompressible SPH (EISPH) solver, the Pressure Poisson Equation (PPE) represented in Equation 2.18 is discretized using the SPH formulation, resulting in the explicit analysis of the pressure field as given in Equation 2.19, where matrix coefficient preceding the pressure term is denoted as A_{ij}, and the source term on the RHS is referred to as b_i(Barcarolo, 2013). With these notations, the particle pressure can be computed as shown in Equation 2.20.

$$\nabla^2 P^{n+1} = \rho \frac{\nabla \cdot u^{pr}}{\Delta t} \tag{2.18}$$

$$\sum_{j=1}^{N} 2 \frac{r_{ij} \cdot \nabla W_{ij}}{\left\| r_{ij} \right\|^2} \frac{m_j}{\rho_j} (P_i^{n+1} - P_j^n) = \left\langle \rho \frac{\nabla \cdot u^{pr}}{\Delta t} \right\rangle \tag{2.19}$$

$$P_i^{n+1} = \left\{ b_i - \sum_j A_{ij} P_j^n \right\} \Big/ \sum_j A_{ij} \tag{2.20}$$

Here, the detailed formulations of A_{ij} and b_i are given in Equation 2.21 and 2.22.

$$A_{ij} = 2 \frac{m_j}{\rho_j} \frac{r_{ij} \cdot \nabla W\left(x_{ij}, h\right)}{r_{ij}^2} \tag{2.21}$$

$$b_i = \frac{\rho(\nabla \cdot u^{pr})}{\Delta t} \tag{2.22}$$

The source term, b_i, acts as a source for the PPE and can be expressed as Eq. 2.22, which are discretized into the Divergence Free (DF) and Density Invariance (DI) forms as Equations 2.23 and 2.24, respectively (Hosseini, 2007). To ensure incompressibility of the fluid, the source term in this study is composed of both DF and DI terms, as shown in Eq. 2.25, where γ is a weighting factor between 0 and 1.

$$b_{i,DF} = \frac{\rho_i \sum_j \frac{m_j}{\rho_j} \left(\boldsymbol{u}_j^{pr} - \boldsymbol{u}_i^{pr}\right) \cdot \left(\boldsymbol{\nabla} W(\boldsymbol{r}_{ij}, h)\right)}{\Delta t} \tag{2.23}$$

$$b_{i,DI} = \frac{\rho_i \left[1 - \frac{\sum_j \frac{m_j}{\rho_j} \cdot \left(W\left(\boldsymbol{r}_{ij}^{pr}, h\right)\right)}{\sum_j \frac{m_j}{\rho_j} \cdot \left(W\left(r_{ij}^{n}, h\right)\right)}\right]}{\Delta t^2} \tag{2.24}$$

$$b_i = \gamma b_{i,DF} + (1 - \gamma)\, b_{i,DI} \tag{2.25}$$

2.4. Numerical Scheme for SPH Accuracy

To perform accurate fluid analysis using SPH method, numerical accuracy in the discretization scheme and proper boundary treatment are essential. In this section, the numerical correction method for SPH derivative and the boundary condition are described.

2.4.1. SPH Derivative Correction

The numerical accuracy of the SPH derivative discretization method

depends on various factors : 1) uniformity of particle distribution, 2) spatial resolution and 3) satisfaction of the unity condition and so on (Fatehi, 2011).

In the vicinity of the boundary, as shown in Figure 2.4, the fluid particles suffer from a significant decrease in the accuracy of SPH derivative discretization methods due to insufficient and asymmetric distribution within the compact domain of fluid particles. To address this issue, numerical correction methods have been proposed by Bonet (1999), Fatehi (2011) and Duan (2022) for the 1st and 2nd order derivative. For the 1st order derivative correction, the kernel gradient correction (KGC) method (Bonet,1999) and corrective matrix method (Duan, 2022) have been introduced.

The KGC method is described in Equation 2.26 and 2.27, where $L(\boldsymbol{r_{ij}})$ denotes correction matrix.

$$\langle \nabla f \rangle_i = \sum_j \frac{m_j}{\rho_j} \{ f(\boldsymbol{r_j}) - f(\boldsymbol{r_i}) \} L(\boldsymbol{r_{ij}}) \cdot \nabla_i W_{ij}, \tag{2.26}$$

$$, \ L(\boldsymbol{r_{ij}}) = \left[\sum_j \begin{bmatrix} x_{ji} \frac{\partial W_{ij}}{\partial x_i} & y_{ji} \frac{\partial W_{ij}}{\partial x_i} & z_{ji} \frac{\partial W_{ij}}{\partial x_i} \\ x_{ji} \frac{\partial W_{ij}}{\partial y_i} & y_{ji} \frac{\partial W_{ij}}{\partial y_i} & z_{ji} \frac{\partial W_{ij}}{\partial y_i} \\ x_{ji} \frac{\partial W_{ij}}{\partial z_i} & y_{ji} \frac{\partial W_{ij}}{\partial z_i} & z_{ji} \frac{\partial W_{ij}}{\partial z_i} \end{bmatrix} \right]^{-1} \tag{2.27}$$

The corrective matrix method is described from Equation 2.28 to 2.31, where N, M and $\boldsymbol{A}$ denote the matrix for numerical correction and d_0 is the particle size.

$$\langle \nabla f \rangle_i = \begin{bmatrix} N_i^1 \\ N_i^2 \\ N_i^3 \end{bmatrix} = \sum_j \frac{m_j}{\rho_j} \frac{f_{ij}}{|r_{ij}|} \begin{bmatrix} A_i^1 \\ A_i^2 \\ A_i^3 \end{bmatrix} \cdot M_{ij} \nabla_i W_{ij} \tag{2.28}$$

$$A_i = \begin{bmatrix} (M_{ij}^1, M_{ij}^1) & \cdots & (M_{ij}^1, M_{ij}^9) \\ \vdots & \ddots & \vdots \\ (M_{ij}^1, M_{ij}^9) & \cdots & (M_{ij}^9, M_{ij}^9) \end{bmatrix}^{-1} \tag{2.29}$$

$$\left(M_{ij}^m, M_{ij}^n\right) = \sum_j \frac{m_j}{\rho_j} M_{ij}^m M_{ij}^n \nabla_i W_{ij} \tag{2.30}$$

$$M_{ij} = \left[\frac{\boldsymbol{x}_{ij}}{|\boldsymbol{r}_{ij}|} \quad \frac{\boldsymbol{y}_{ij}}{|\boldsymbol{r}_{ij}|} \quad \frac{\boldsymbol{z}_{ij}}{|\boldsymbol{r}_{ij}|} \quad \frac{1}{d_0}\frac{\boldsymbol{x}_{ij}^2}{|\boldsymbol{r}_{ij}|} \quad \frac{1}{d_0}\frac{\boldsymbol{y}_{ij}^2}{|\boldsymbol{r}_{ij}|} \quad \frac{1}{d_0}\frac{\boldsymbol{z}_{ij}^2}{|\boldsymbol{r}_{ij}|} \quad \frac{1}{d_0}\frac{\boldsymbol{x}_{ij}\boldsymbol{y}_{ij}}{|\boldsymbol{r}_{ij}|} \quad \frac{1}{d_0}\frac{\boldsymbol{y}_{ij}\boldsymbol{z}_{ij}}{|\boldsymbol{r}_{ij}|} \quad \frac{1}{d_0}\frac{\boldsymbol{z}_{ij}\boldsymbol{x}_{ij}}{|\boldsymbol{r}_{ij}|}\right]^T \tag{2.31}$$

2.4.2. Particle Shifting Scheme

To mitigate the degradation of numerical accuracy caused by the non-uniform distribution of particles, a particle shifting scheme has been proposed (Lind, 2012). Based on the particle number density, an adjustment vector $\delta \boldsymbol{r_i}$ is computed for achieving uniform particle distribution by analyzing the particle number density diffusion equation, similar to Fick's law, as shown in Equation 2.32 (Skillen, 2013), where R_s and q are constant parameters, set to 0.2 and 4.0. $\Delta \boldsymbol{r}$ is the initial spacing distance between particles.

$$\delta \boldsymbol{r_i} = -4|\boldsymbol{u_i}|h_i \Delta t \sum_j \frac{m_j}{\rho_j}\left(1 + R_s\left(\frac{W(\boldsymbol{r_{ij}}, h)}{W(\Delta \boldsymbol{r}, h)}\right)^q\right)\nabla W_{ij} \tag{2.32}$$

To prevent flow structure distortion caused by the particle shifting scheme, the particle position and physical quantities f are simultaneously updated using Equation 2.33 and 2.34. The superscript $\boldsymbol{a}$ denotes shifting scheme applied variable.

$$\boldsymbol{x_i^a} = \boldsymbol{x_i} + \delta \boldsymbol{x_i} \tag{2.33}$$

$$f_i^a = f_i + \nabla f_i \cdot \delta \boldsymbol{x_i} \tag{2.34}$$

2.4.3. Boundary Treatment

For the formulation of flow boundary in SPH method, dummy particles are utilized in this study, as depicted in Figure 2.5. To enforce the no-slip and pressure boundary conditions, the generalized boundary condition proposed by Adami (2012) has been adopted and calculate velocity and pressure of dummy particles.

The velocity and pressure of the dummy particles are calculated based on the velocity and pressure of neighboring fluid particles within the compact domain of the dummy particles, as expressed in Equation 2.35 and 2.36. Here, the subscript f means SPH fluid particles.

$$\boldsymbol{u}_i = -\sum_{j \in f} \frac{m_j}{\rho_j} \boldsymbol{u}_j W_{ij} \Big/ \sum_{j \in f} \frac{m_j}{\rho_j} W_{ij} \tag{2.35}$$

$$P_i = \left\{ \sum_{j \in f} \frac{m_j}{\rho_j} P_j W_{ij} \right\} \Big/ \sum_{j \in f} \frac{m_j}{\rho_j} W_{ij} \tag{2.36}$$

The entire algorithm for EISPH solver is shown in Figure 2.6

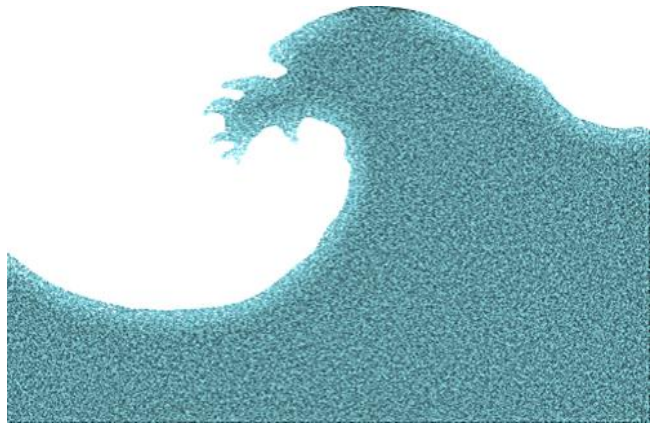

(a) Flow field for analysis

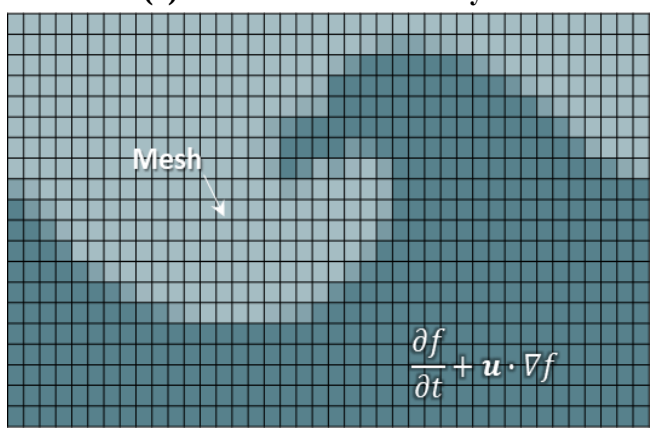

(b) Eulerian Specification

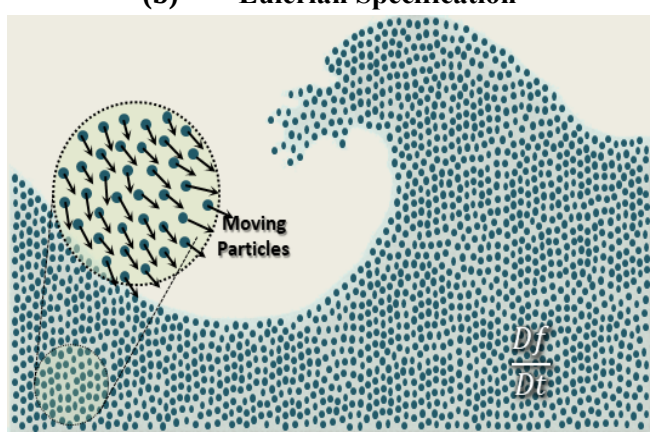

(c) Lagrangian Specification

Figure.2.1. Lagrangian and Eulerian specification

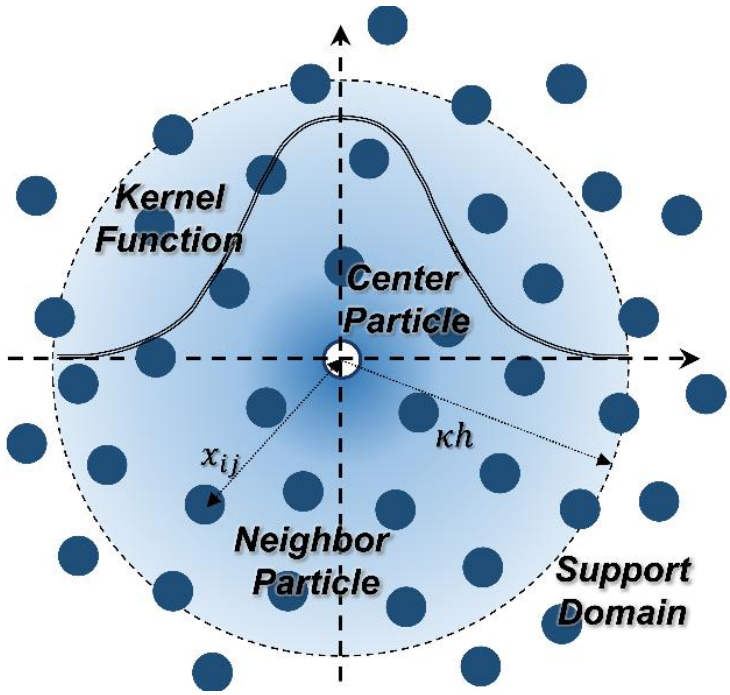

Figure. 2.2. SPH interpolation and kernel function

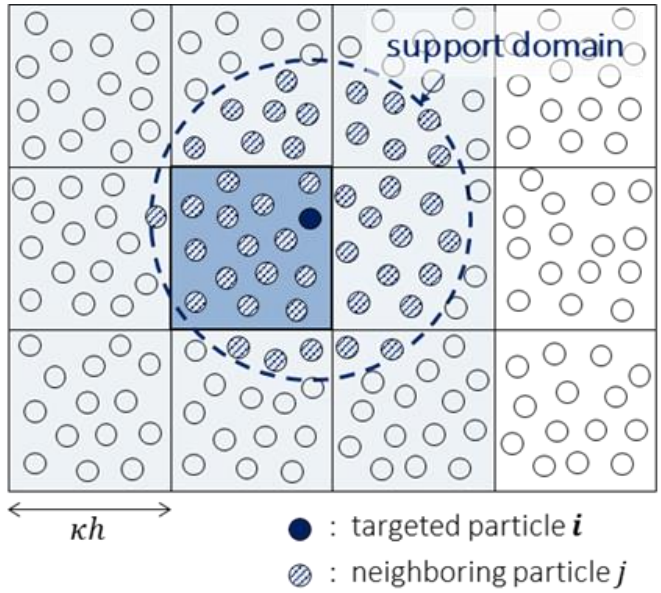

Figure.2.3. Link-list algorithm for NNPS

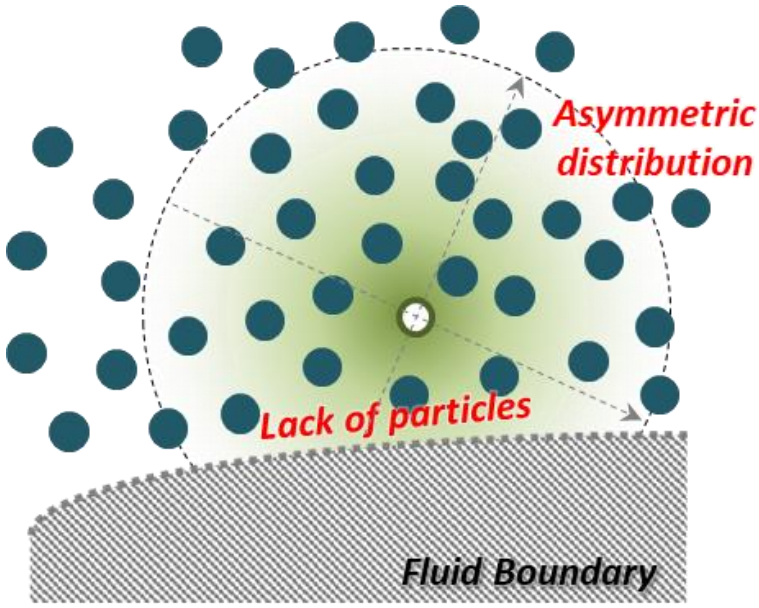

Figure.2.4. Dissatisfaction of unity condition near boundary

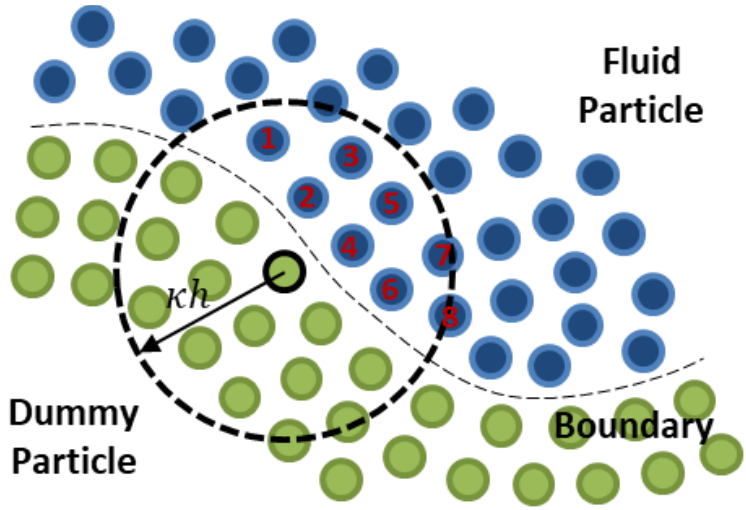

Figure. 2.5. Generalized boundary condition

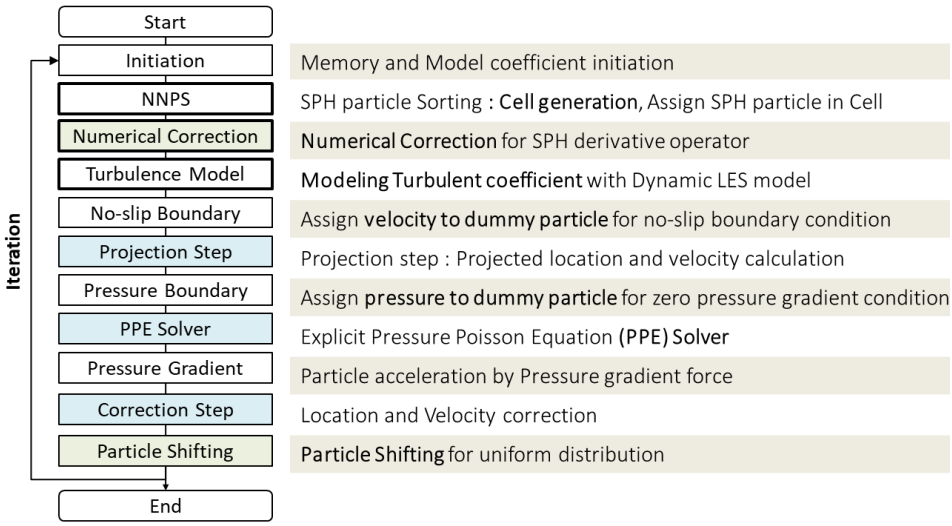

Figure.2.6. EISPH solver Algorithm

Chapter 3 Dynamic LES-SPH Model

In this study, a turbulent-SPH model has been developed to accurately analyze turbulent natural convection, which cause thermal ablation. The turbulent-SPH model should be capable of accurately analyzing various flow conditions, including laminar, transitional and turbulent regimes in natural convection, as well as enabling direct resolution of the boundary layer for accurate prediction of heat flux at phase interface. When analyzing natural convection with high *Ra* number, it is necessary to consider the influence of buoyancy on the turbulent flow. Therefore, validated RANS models such as ANK model, MKC model (Fukasawa, 2008), as well as dynamic Smagorinsky model (Germano, 1991), and dynamic Vreman model (You, 2007; You, 2009) were selected as candidate models to evaluate their compatibility with SPH model.

The evaluation criteria for candidate turbulence models consisted of: 1) Accuracy in analyzing transient eddy motion, 2) Integration feasibility with the SPH model, and 3) Additional computational load incurred by the introduction of the turbulence model.

Previous studies (Lau, 2012; Whang, 2021) have confirmed that dynamic LES models effectively analyze the development of transient flows and eddy motion in turbulent natural convection. Regarding the integration feasibility with SPH model, the spatial filter process performed in LES for SGS stress filtering can be readily implemented using the linked-list method, which is introduced in SPH method as the NNPS algorithm. Moreover, due to the numerical similarity between LES using spatial filter function and SPH using kernel function as a spatial weighting

function, the incorporation of LES model into SPH is facilitated. Finally, in terms of computational cost, for RANS models that cannot incorporate wall functions due to the characteristics of SPH discretization, the boundary layer should be fully resolved similar to LES model. However, modeling turbulent flows necessitates the additional analysis of transport equations, such as turbulent kinetic energy and turbulent dissipation rate, resulting in higher computational costs compared to LES. Therefore, for these reasons, a dynamic LES based SPH model was developed.

3.1. SPH Formulation for LES-SPH model

In the LES model, for modeling turbulent flow, a spatial filter function, which is a spatial weighting function, is utilized to decompose a physical quantity f into its spatial-filtered component $\overline{(f)}$ and the sub particle scale (SPS) component as Equation 3.1.

$$f_i = \bar{f}_i + f_i' \tag{3.1}$$

The filtering process using the spatial filter function G for the filtered component is described by Equation 3.2.

$$\bar{f}_i = \int G(\boldsymbol{x} - \boldsymbol{x}') f_j(\boldsymbol{x}) d\boldsymbol{x}' \tag{3.2}$$

This filtering process is mathematically identical to the SPH kernel interpolation presented in Equation 2.2. Consequently, unlike conventional CFD that require filtering process before flow analysis, the SPH method inherently incorporates the filtering process with governing equation discretization process.

3.1.1. Spatial weighting function for LES-SPH model

Due to the nature of LES modeling, which aims to model the effect of the SPS component, the SPS filtering process using the filter function is crucial for ensuring numerical accuracy in LES model. Therefore, in this study that employs SPH kernel function as spatial filter function, evaluating the performance of the kernel function as a filter is essential.

The filter function acts as a low-pass filter, thereby requiring a high attenuation capacity in the high-frequency range of the energy spectrum. The auto-covariance R_{11} and energy spectrum E_{11} are defined by Equation 3.3 and Equation 3.4, respectively. The energy spectrum of filtered auto-covariance is represented as the original energy spectrum multiplied by the attenuation factor $\left|\hat{G}(w)\right|^2$ of the filter which is the Fourier-transformed variable of spatial filter, where w denotes the frequency in energy spectrum.

$$R_{11} = u'(r)u'(r + r') \tag{3.3}$$

$$E_{11}(w) = \mathcal{F}(R_{11}) \tag{3.4}$$

$$\bar{E}_{11}(w) = \left|\hat{G}(w)\right|^2 E_{11}(w) \tag{3.5}$$

The attenuation factor for the Wendland C2/C4/C6 functions, which are being used as the SPH kernel, was examined and compared in Figure 3.1. The results indicated that the Wendland C2 kernel function outperforms the others as a low-pass filter. Therefore, for the LES-SPH model in this study, the Wendland 2 kernel function was utilized as the spatial weighting function. The Wendland2 kernel

function is represented in Equation 3.6 and 3.7.

$$W(R,h) = C(1-R)^4(1+4R) \tag{3.6}$$

$$C = \begin{cases} \dfrac{7}{2\pi \cdot 4h^2} & for\ 2D \\ \dfrac{21}{2\pi \cdot 8h^2} & for\ 3D \end{cases} \tag{3.7}$$

Where $\boldsymbol{R}$ is a non-dimensional distance, which is defined as $\boldsymbol{R} = \left|\boldsymbol{r_i} - \boldsymbol{r_j}\right|/2h$.

3.1.2. SPH Formulation for Filtering Operator

In the Dynamic LES models, turbulent model coefficients are calculated using single or double filtering value of the gradients of physical quantities such as velocity and temperature. Therefore, it is crucial to accurately perform SPH discretization for the derivative and filtering operators.

The equation representing the single filtered derivative operator is given by Equation 3.8. This equation corresponds to the SPH discretization method for the derivative when the unity and symmetric conditions of SPH are satisfied, as shown in Equation 2.3.

$$\overline{\nabla f_i} = \int G(\boldsymbol{x} - \boldsymbol{x}')\nabla f_j(\boldsymbol{x})d\boldsymbol{x}' \tag{3.8}$$

The double filtered derivative operator, utilizing two spatial filters with different filter lengths, namely the test filter and the grid filter, can be expressed as Equation 3.9. In this equation, G_1 and G_2 represents the grid and test filters. SPH

analysis domain and each filter are illustrated in Figure 3.2.

$$\widehat{\overline{\nabla f_i}} = \int G_2(\boldsymbol{x}-\boldsymbol{x}')\left\{\int G_1(\boldsymbol{x}-\boldsymbol{x}')\nabla f_j(\boldsymbol{x})d\boldsymbol{x}'\right\}d\boldsymbol{x}' \tag{3.9}$$

The SPH discretization of the double filtered derivative can be expressed using Equation (3.10) and Equation (3.11). The subscripts g and t in these equations represent the kernel functions corresponding to the grid filter and test filter, respectively.

$$\left(\widehat{\overline{\nabla f_i}}\right)_1 = \sum_j \frac{m_j}{\rho_j}\left\{\sum_j \frac{m_j}{\rho_j} f_j\, W_{ij,g}\right\}\nabla W_{ij,t} \tag{3.10}$$

$$\left\{\widehat{\overline{\nabla f_i}}\right\}_2 = \sum_j \frac{m_j}{\rho_j}\left\{\sum_j \frac{m_j}{\rho_j} f_j\, \nabla W_{ij,g}\right\} W_{ij,t} \tag{3.11}$$

When the double filtered derivative was discretized into SPH formulation, it is important to note that a commutation error can occur between the two filters with different length scales and the derivative operator. To ensure numerical accuracy, a benchmark was conducted for the distribution of physical quantities in a triangular function form, as shown in Figure 3.3. Reference value of double filtered derivative was calculated with Equation 3.12, and the Root Mean Square Error (RMSE) was calculated to evaluate the numerical accuracy of Equation 3.10 and 3.11.

$$\left\{\widehat{\overline{\nabla f}}\right\}_r = \sum_j \frac{m_j}{\rho_j}\left\{\sum_j \frac{m_j}{\rho_j} (\nabla f)_j\, W_{ij,g}\right\} W_{ij,t} \tag{3.11}$$

The benchmark results for the RMSE in each direction are listed in Table 3.1.

It was confirmed that the RMSE increases as spatial frequency of physical quantities increase. In this study, the discretization method described in Equation 3.11 is utilized for double filtered derivative value.

3.1.3. Improvement of Filtered derivative operator

In Dynamic LES models, the filtered first-order derivative of velocity and temperature are utilized for modeling turbulent viscosity and scalar diffusivity coefficients. Therefore, the accuracy of the 1st order derivative formulation in SPH method is crucial for dynamic LES-SPH modeling. The accuracy of the SPH discretization for the 1st order derivative depends on several factors, including 1) the uniformity of particle distribution, 2) spatial resolution, 3) numerical correction methodology, and 4) satisfaction of the unity condition. (Fatehi, 2011)

■ **Benchmark for the accuracy of SPH 1st order derivative**

a benchmark study (Duan,2022) was conducted to evaluate the numerical accuracy of the 1st order derivative with respect to the uniformity of particle distribution, spatial resolution, and numerical correction method. For a 2D square domain with side length 1.0, as shown in Figure 3.4, the distribution of the physical quantity was given by Equation 3.12. The numerical accuracy of the original SPH derivative operator, the KGC method (Bonet,1999) and the corrective matrix method (Duan,2022) was evaluated considering various spatial resolutions, particle distribution uniformity. Reference value of the 1st order derivative was calculated as Equation 3.13 and Equation 3.14, and RMSE was calculated to evaluate the numerical accuracy of each derivative method.

$$f(x,y) = 5x + 3y + 10x^2 + 30xy + 20y^2 + 15x^3 + 30x^2y + \qquad (3.12)$$

$$40xy^2 + 25y^3$$

$$\left\{\frac{\partial f}{\partial x}\right\}_r = \sum_j \frac{m_j}{\rho_j}\left(\frac{\partial f}{\partial x}\right)_j W_{ij} \tag{3.13}$$

$$\left(\frac{\partial f}{\partial x}\right) = 5 + 20x^2 + 30y + 45x^2 + 60xy + 40y^2 \tag{3.14}$$

The benchmark results are presented in Figure 3.5, which demonstrates that as the spatial resolution increases, applying the KGC correction and corrective matrix method leads to a decrease in RMSE. However, it was observed that the accuracy of the corrective matrix method significantly deteriorates when the irregularity of particle distribution exceeds approximately 1% of the particle size from the regular distribution. These results indicate that KGC is the most robust in particle distribution. Furthermore, the corrective matrix method requires large computational cost compared to KGC method as it involves 9×9 matrix operations for each SPH particle in 3D analysis. Therefore, in this study, the KGC method was utilized to improve the accuracy of the SPH 1st order derivative operator.

■ **Benchmark for the 1st order derivative near boundary**

To achieve accurate flow analysis in the boundary layer using the dynamic LES-SPH model, it is essential to compute the 1st order derivative of the physical quantities near the flow boundary. In order to evaluate the accuracy of the 1st order derivative in SPH formulation near flow boundaries where the unity condition is not satisfied, a benchmark validation as shown in Figure 3.6 was conducted.

In this benchmark, a 2D channel configuration was considered, where the velocity was distributed as a linear or fourth-order polynomial. The velocity gradients of fluid particles near the boundary were computed using the SPH

discretization of 1st order derivative with or without the inclusion of dummy particles, as shown in Figure 3.7(a). When dummy particles were included in the SPH interpolation, the velocity of dummy particles was either fixed at zero, or computed using the generalized boundary condition concept, where the velocity of the dummy particles was calculated by extrapolating the velocity of neighboring fluid particles using Equation 2.34, as shown in Figure 3.7(b). For case where, dummy particles were not included in the kernel interpolation, the 1st order velocity derivative of fluid particle near the boundary were computed using KGC correction.

The benchmark results, presented in Figure 3.8, indicate that for both cases, the most accurate rate of strain value was obtained by applying KGC without including the dummy particles in kernel interpolation. Therefore, when calculating the derivative near the wall, only fluid particles were utilized in the calculations, excluding the dummy particles.

3.2. Dynamic LES-SPH Model

3.2.1. Standard Smagorinsky Model

The Standard Smagorinsky model (Smagorinsky, 1963) is introduced in SPH method as a reference model. SSM is a methodology that models eddy viscosity with a filtered rate of strain and Smagorinsky constant as Equation 3.15 where l_s, C_s, h and $\bar{S}$ denote Smagorinsky length scale, Smagorinsky constant, filter length and filtered rate of strain.

$$\mu_{t,i} = \rho_i l_s^2 \bar{S} = \rho_i (C_s h)^2 \bar{S} \tag{3.15}$$

In this model, the Smagorinsky constant takes a constant value between 0.1 to 0.2 as a ratio between a turbulent component and particle size. The filtered rate of

strain is calculated with the filtered strain rate as Equation 3.16, 3.17 and 3.18, where subscripts a and b are directional signs (Violeau, 2007).

$$\bar{S} = \sqrt{2\bar{S}_{ab}\bar{S}_{ab}} \tag{3.16}$$

$$\bar{\boldsymbol{S}}_{ab} = \frac{1}{2}\left(\frac{\partial u_a}{\partial x_b} + \frac{\partial u_b}{\partial x_a}\right) \tag{3.17}$$

$$\bar{\boldsymbol{S}}_{ab} = \frac{1}{2}\left\{\sum_{j\in f}\frac{m_j}{\rho_j}(u_{a,j} - u_{a,i})\frac{\partial W_{ij}}{\partial x_b} + \sum_{j\in f}\frac{m_j}{\rho_j}(u_{b,j} - u_{b,i})\frac{\partial W_{ij}}{\partial x_a}\right\} \tag{3.18}$$

The spatial derivative term along a and b coordinates are a kernel gradient component corrected with a KGC matrix. Smagorinsky constant is 0.15 in this study.

3.2.2. Dynamic Smagorinsky Model

The dynamic Smagorinsky model (Germano, 1991) is a LES model that determines the Smagorinsky constant based on local equilibrium assumption. In this approach, the sub-particle scale stresses, denoted as τ_{ij} and T_{ij}, are filtered out using grid and test filters, as depicted in Figure 3.9. The filter length of grid and test filter is h and $2h$. These sub-particle scale stresses can be modeled using Equations 3.19 to 3.22. Since the modeling is performed for a local point, the same model coefficient, C_d, is utilized in Equations 3.19 and 3.21.

$$\tau_{ab} = 2C_d\alpha_{ab} \tag{3.19}$$

$$\alpha_{ab} = h^2|\bar{S}|\bar{S}_{ab} \tag{3.20}$$

$$T_{ab} = 2C_d\beta_{ab} \tag{3.21}$$

$$\beta_{ab} = \hat{h}^2 \left|\hat{\bar{S}}\right| \hat{\bar{S}}_{ab} \tag{3.22}$$

By utilizing Germano's identity (Germano, 1991), the relationship between the difference of the two sub-particle scale stresses and the filtered velocity field can be expressed in Equations 3.23 and 3.24. Consequently, turbulent model coefficient C_d can be modeled with volume averaging as shown in Equation 3.25. In Equation 3.25, the subscript *V* represents the volume average. For volume averaging operation, the values of neighboring particles within the kernel radius of the fluid particles were averaged as Equation 3.27.

For numerical stability, the values of C_d were clipped to the range of 0 to 0.23. In this context, the turbulent viscosity is defined as in Equation 3.26. The discretization methodology for each term at grid and test filter scales is summarized in Table 3.2 to 3.5.

$$L_{ij} = -2C_d(\beta_{ab} - \tilde{\alpha}_{ab}) = \widehat{\bar{u}_a\bar{u}_b} - \hat{\bar{u}}_a\hat{\bar{u}}_b = 2C_d\Delta^2 M_{ab}, \tag{3.23}$$

$$M_{ab} = (\hat{h}^2/\ h^2)\left|\hat{\bar{S}}\right|\hat{\bar{S}}_{ab} - \widehat{|\bar{S}|\bar{S}_{ab}} \tag{3.24}$$

$$C_d h^2 = \frac{1}{2}\frac{L_{ab}}{M_{ab}} = \frac{1}{2}\frac{L_{ab}M_{ab}}{M_{ab}M_{ab}} = \left\langle\frac{1}{2}\frac{L_{ab}M_{ab}}{M_{ab}M_{ab}}\right\rangle_{\boldsymbol{V}} \tag{3.25}$$

$$\nu_t = \boldsymbol{C_d} h^2|\bar{S}| \tag{3.26}$$

$$\langle f \rangle_V = \frac{\sum_j \frac{m_j}{\rho_j} f_j W_{ij}}{\sum_j \frac{m_j}{\rho_j} W_{ij}} \tag{3.27}$$

3.2.3. Dynamic Vreman Model

The dynamic Vreman model (You, 2007) calculate the model coefficient universally for various flow condition with numerical stability. Previous study has shown that DVM provide accurate results in turbulent natural circulation including laminar, turbulent, re-laminar flow compared to DSM (Whang, 2021).

Using grid and test filter, of which filtering length is h and $2h$ respectively, a model coefficient is calculated explicitly, and dissipation of sub-particle scale stress disappears in the laminar flow region. Equation 3.28 represents the single and double filtered velocity derivative terms. Equation 3.29 and 3.30 are used to calculate the filter scale-dependent coefficient, β. Equation. 3.31 calculates the product of the filter scale-dependent coefficient and the strain rate. Finally, Equation 3.32 calculates the turbulent viscosity, which is proportional to the product of the filter scale-dependent coefficient and the strain rate, normalized by the product of the single and double filtered velocity derivative terms. Subscript V is a volume averaging operator over the entire computational domain. In this study, CUDA library was utilized to calculate a volume averaging value. Therefore, turbulent viscosity is updated every time step and uniformly applied to the overall domain in a time step.

$$\bar{\alpha}_{ab} = \overline{\frac{\partial u_b}{\partial x_a}}, \qquad \hat{\bar{\alpha}}_{ab} = \widehat{\frac{\partial u_b}{\partial x_a}} \tag{3.28}$$

$$\beta_{ab}^{g} = \sum_{m=1}^{3} h^2 \, \bar{\alpha}_{ma} \bar{\alpha}_{mb}, \; \beta_{ab}^{t} = \sum_{m=1}^{3} (2h)^2 \, \hat{\bar{\alpha}}_{ma} \hat{\bar{\alpha}}_{mb} \tag{3.29}$$

$$B_\beta^{g(t)} = \beta_{11}^{g(t)}\beta_{22}^{g(t)} - \beta_{12}^{g(t)}\beta_{12}^{g(t)} + \beta_{11}^{g(t)}\beta_{33}^{g(t)} - \beta_{13}^{g(t)}\beta_{13}^{g(t)} + \beta_{22}^{g(t)}\beta_{33}^{g(t)} - \beta_{23}^{g(t)}\beta_{23}^{(t)} \tag{3.30}$$

$$\Pi^g = \sqrt{\frac{B_\beta^g}{\bar{\alpha}_{ab}\bar{\alpha}_{ab}}}, \quad \Pi^t = \sqrt{\frac{B_\beta^t}{\hat{\bar{\alpha}}_{ab}\hat{\bar{\alpha}}_{ab}}} \tag{3.31}$$

$$\nu_t^g = -\frac{\nu}{2}\cdot\frac{[\bar{\alpha}_{ab}\widetilde{\bar{\alpha}_{ab}} - \tilde{\bar{\alpha}}_{ab}\tilde{\bar{\alpha}}_{ab}]_V}{\left[\Pi^g\bar{S}_{ab}\widetilde{\bar{S}_{ab}} - \Pi^t\tilde{\bar{S}}_{ab}\tilde{\bar{S}}_{ab}\right]_V}\Pi^g \tag{3.32}$$

The DVM also provides modeling for turbulent diffusivity in scalar fields such as energy (You, 2009). In the case of temperature θ and thermal diffusivity α, the effective thermal diffusivity is modeled as Equation 3.33 and 3.34.

$$D_T{}' = \frac{\left\langle \nu_T^t\overline{\frac{\partial\widetilde{\theta}}{\partial x_a}}\overline{\frac{\partial\widetilde{\theta}}{\partial x_a}} - \nu_T^g\overline{\frac{\partial\widetilde{\theta}}{\partial x_a}}\overline{\frac{\partial\theta}{\partial x_a}}\right\rangle_V}{\left\langle\overline{\frac{\partial\widetilde{\theta}}{\partial x_a}}\overline{\frac{\partial\widetilde{\theta}}{\partial x_a}} - \overline{\frac{\partial\widetilde{\theta}}{\partial x_a}}\overline{\frac{\partial\widetilde{\theta}}{\partial x_a}}\right\rangle_V} \tag{3.33}$$

$$\alpha_{eff} = \alpha + \alpha\frac{\nu_T^g}{D_T{}'} \tag{3.34}$$

The discretization methods for each term at grid and test filter scales are summarized in Table 3.4 to 3.6.

3.2.4. Turbulent Prandtl Number Modeling

In standard and dynamic Smagorinsky based LES-SPH model, turbulent Prandtl number (Pr_t) is employed to model the turbulent energy diffusion, and the value of Pr_t is close to unity based on the Reynolds analogy. The effective thermal diffusivity is modeled as Equation 3.35.

$$\alpha_{eff} = \alpha + \frac{\nu_t}{Pr_t} \tag{3.35}$$

However, for low-Prandtl number fluids such as corium and liquid metal, where molecular diffusion dominates the energy transfer, the characteristics of turbulent heat transfer differ from those of ordinary fluids. This can be confirmed in DNS research, as shown in Figure 3.10. (Kawamura, 1999; Redjem-Saad, 2007). Figure 3.10 illustrates the non-linear distribution of the turbulent Prandtl number for low-Prandtl number fluids when non-dimensional distance y^+ is greater than 10.0. Therefore, using a constant turbulent Prandtl number close to unity leads to significantly over-predicted heat transfer trends compared to DNS results and correlations constructed from experimental data. Additionally, due to the dominance of conduction, the thermal boundary layers become much thicker than the flowing boundary layer, as depicted in Figure 3.11. Thus, accurate modeling of Pr_t under different flow conditions is essential for precise modeling in the viscous sub-layer and buffer layer.

In viscous sub-layer, where turbulent viscosity tends to zero, heat transfer is primarily governed by molecular heat transfer, rendering the corresponding Pr_t in this region meaningless (Myong, 1989). However, for an accurate heat transfer analysis in the buffer region, Pr_t modeling is required.

To address these issues, Pr_t modeling methods considering fluid properties and flow characteristics were suggested and can be broadly classified into global and local models. The global models involve Pr_t modeling through parameters such as Pr, Re or Peclet number Pe which specify the thermal flow conditions. The detailed global models are summarized in Table. 3.7.

On the other hand, the local model models Pr_t based on local spatial parameter such as y^+, turbulent Peclet number Pe_t or the ratio of turbulent viscosity to molecular viscosity (μ_t/μ). In this approach, Pr_t is modeled for each time step. The equations for the local models are summarized in Table 3.8.

Among the proposed global and local models, Cheng&Tak's model (Cheng, 2006) and Kay's model (Kay, 1994) have been found to predict accurate results for working fluids such as lead-bismuth, with the global model demonstrating superior accuracy (Lei, 2022).

In this study, for the simulation cases of thermal ablation in metals and the behavior of corium in IVR-ERV scenarios with application of standard or dynamic Smagorinsky models, Cheng & Tak's models will be used.

3.3. Validation and Verification

3.3.1 Benchmark of Lid-driven Flow

The transitional and turbulent lid-driven cavity flow analysis has been carried out as benchmark simulations. This benchmark aims to evaluate the performance of dynamic LES-SPH models for both transitional and turbulent flow regimes at *Re* of 5,000 and 12,000. Detailed geometry conditions are described in Figure 3.12. The lid velocity is determined as Equation 3.36 for numerical stability near corners of cavity. The characteristic velocity U_0 is set to 1.0 m/s.

The Reynolds number of the cavity flow is defined using Equation 3.37, with a reference density of 1,000 kg/m^3, and the no-slip condition is applied to every plane of the cavity.

$$U_x(x,y) = -U_0[1.0 - 2.0(0.5 - x)^{18.0}]^{2.0}[1.0 - 2.0(0.5 - y)^{18.0}]^{2.0} \qquad (3.36)$$

$$Re = \frac{\rho_{ref} U_0 L}{\mu} \qquad (3.37)$$

3.3.2 Transitional Lid-driven Flow

A cavity flow analysis with *Re*=5,000 has been conducted to evaluate the accuracy of dynamic LES models in the transitional flow region. The DSM and DVM analysis results theoretically exclude the effect of sub-particle scale stress in the laminar region, leading to different trends in flow damping compared to SSM analysis.

The velocity field of turbulent flow was analyzed by examining the time-

averaged velocity (Kato, 1992) and perturbation component (Samantary, 2018). The analysis results for time-averaged velocity distributions from SSM, DSM, and DVM were consistent with the finding of Prasad (1989), as shown in Figure 3.13, but the magnitude of the velocity of DVM result was smaller than that of SSM and DSM near the wall region. These results suggest that DVM predict sub-particle scale stress to be smaller than SSM and DSM in the vicinity of a wall and transition region. Additionally, the accuracy of the transient flow was evaluated by analyzing the velocity perturbation which is directly related to Reynolds stress, as shown in Figure 3.14. The DVM analysis results were found to exhibit a trend consistent with previous experimental research (Prasad, 1989) and CFD studies utilizing the DSM (Samantary, 2018).

The results of SSM and DSM show an excessive steady analysis in the central region of the cavity and the downward flow-dominated regions. The excessive modeling of turbulent viscosity in SSM leads to these results, particularly near the boundary and under transitional flow conditions. In the case of DSM, the analysis results are influenced by two factors: 1) the setting of the clipping range for model coefficients and 2) the volume averaging performed in the compact domain of the kernel function.

To evaluate the transient flow analysis capabilities of each LES model, the instantaneous streamline results were compared. Figures 3.15 to 3.17 show the streamlines of the LES models' analysis results at 100.0, 200.0, and 300.0 seconds. The DVM analysis results align with previous research indicating the occurrence of transient flow structures at Reynolds numbers above 2,000. Thus, the benchmark results demonstrate that the DVM is more accurate than the SSM and DSM in transient flow analysis using the SPH method.

3.3.3 Turbulent Lid-driven Flow

To evaluate the performance of SSM-SPH and DVM-SPH model in a developed turbulent flow, cavity flow analysis at Re=12,000 was conducted. Previous research (Leriche, 2000) suggested that the transient characteristics of flow intensify at *Re*=12,000, and the reignition and extinction of eddies with small length scales occur more frequently. Additionally, it is expected that the downward flow near the wall at x=1.0m is more developed.

Figure 3.18 shows the Reynolds-averaged velocity distribution at x=0.5m and z=0.5m lines on the symmetrical mid-plane. The overall velocity distributions are consistent with previous experimental (Prasad,1989) and numerical research (Leriche, 2000) for both SSM and DVM simulations. However, there are noticeable differences in the velocity distribution near the wall region. In Figure 3.18(a), the Reynolds averaged velocity distribution of the SSM-SPH is broadened within z=0.2m, whereas the result of DVM follows the trend of DNS (Leriche, 2000) and experiment (Samantary, 2018). Similarly, in Figure 3.18(b), the results of SSM overestimates the velocity distribution within x=0.3m, while DVM results are similar to previous researches.

To evaluate the accuracy of flow analysis in the boundary layer, skin friction factor at the bottom of the cavity was compared to the findings of Samantary (2018) and verified. The skin friction factor is defined as Equation 3.38.

$$C_f{}' = \frac{2}{Re}\left(\frac{\partial \bar{u}}{\partial z} + \frac{\partial \bar{v}}{\partial z}\right) \tag{3.38}$$

The analysis results are presented in Figure 3.19, revealing that the results

obtained using the DVM exhibits a similar trend to the results of Samantary (2018). However, for SSM, an excessive turbulence viscosity modeling in boundary layer led to underprediction of the skin friction factor.

These findings suggest that DVM outperforms SSM in accurately modeling the velocity distribution near the wall region in a developed turbulence structure.

In the magnitude of velocity fluctuation, Figure 3.20 (a) and (b) show the velocity fluctuation distribution at x=0.5m and z=0.5 line on a symmetrical mid plane.

The results of the DVM, as shown in Figure 3.20(a), exhibit a similar trend to previous studies in the central region of the cavity. On the other hand, the result of SSM shows excessive viscous damping throughout the flow. Figure 3.20(b) demonstrates that the analysis results of the DVM are highly accurate in the region dominated by downward flow, and they exhibit a similar trend to the DNS analysis results throughout the flow domain. The analysis results are further supported by the instantaneous velocity streamline at a symmetrical mid-plane. Figure 3.21 and 3.22 illustrate the streamlines of the SSM and DVM analysis results, respectively, at 100.s, 200.0s, and 300.0s. The SSM streamline has a noisy pattern in the lower left and right sides of the cavity, but the flow structure remains steady. In contrast, the DVM streamlines exhibit a highly unsteady flow structure.

Figures 3.23 and 3.24 present the results of spectral analysis conducted on the SSM and DVM simulation results. Turbulent kinetic energy was calculated using Equation 3.39, and four symmetrical mid-plane sampling points were selected.

$$TKE = \frac{1}{2}(u'_x u'_x + u'_y u'_y + u'_z u'_z) \tag{3.39}$$

Sampling points were positioned symmetrically with respect to the cavity center at coordinates P1 (0.25,0.0,0.25), P2 (0.25,0.0,0.75), P3 (0.75,0.0,0.25), and P4 (0.75,0.0,0.75). The black dotted line in each figure with a slope of -5/3 represents turbulent kinetic energy dissipation in the inertial-subrange. DVM analysis results at all sampling points followed the -5/3 slope well. However, the SSM results showed an energy flattening region in turbulent components with a small length scale.

Based on these benchmark results, it was confirmed that the DVM provides accurate analytical results under various flow conditions. However, for the DSM model, it was determined that it is not suitable for application in the SPH model due to the arbitrariness in setting the clipping range of model coefficients and the range of volume averaging.

3.3.4 Benchmark of Rayleigh-Benard Convection

To verify the turbulent energy transfer capacity of the DVM-SPH model, benchmark simulations have been conducted for cubical Rayleigh-Benard (RB) convection under two inversion parameter conditions : θ_m of 0.0 and 0.5.

The analysis schematic is shown in Figure 3.25, and the temperature-density ranges are specified in Figure 3.26. The working fluid is water, and the inversion parameter θ_m is defined as Equation 3.40, where T_h, T_c and T_m denote hot side temperature, cold side temperature and the temperature where the density of water is maximum. The density of water is calculated using Equation 3.41, where the coefficient is $\gamma = 9.297173 \times 10^{-6}$, the exponent is $q = 1.894816$ and the maximum density is $\rho_m = 999.972\ kg/m^3$.

$$\theta_m = \frac{T_m - T_c}{T_h - T_c} \tag{3.40}$$

$$\rho_i(T) = \rho_m(1 - \gamma|T_i - T_m|^q) \tag{3.41}$$

In the case of an inversion parameter $\theta_m = 0.0$, the flow is the typical natural convection phenomenon where the density decreases with increasing temperature. On the other hand, in the case of an inversion parameter $\theta_m = 0.5$, the temperature range includes T_m where water's maximum density occurs. In this case, a penetrative convection occurs where the fluid is heated in the lower hot region and rises, while the cooled fluid in the upper cold region does not descend due to buoyancy effects.

The key parameters that characterize the flow behavior are the inversion parameter θ_m, Rayleigh number *Ra*, and Prandtl number *Pr*. The specific analysis conditions are summarized in Table 3.10 and 3.11.

3.3.5 Turbulent Rayleigh-Benard Convection

The analysis results were verified by comparing the dimensionless spatially-averaged Nusselt number at the hot side surface with a previous study (Huang, 2018) in which the Wall-Adapting Local Eddy-viscosity (WALE) model was used. The non-dimensional temperature and time were defined using the reference values given in Equation 3.42 and 3.43, and the spatially-averaged Nusselt number was defined as Equation 3.44.

$$\theta_i = \frac{T_i - T_m}{T_h - T_c} \tag{3.42}$$

$$\tau_0 = H/\sqrt{g\gamma(T_h - T_c)^q H} \tag{3.43}$$

$$Nu = -\langle \frac{\partial \theta}{\partial Z} \rangle_A \tag{3.44}$$

For the cases with inversion parameter of 0.0 and 0.5, the *Nu* are shown in Figure 3.27 and 3.28. In the case where inversion parameter is 0.0, the flow instability due to buoyancy leads to the rapid upward movement of the fluid near the hot side. Consequently, in Figure 3.27, the *Nu* initially decreases sharply, then increases as the heated fluid rises, and eventually converges as the flow develops and turbulent heat transfer stabilizes within the cavity.

In case of simulation results with SSM, the initial fluid temperature in cavity was set to $\theta_i = 0.0$, and it was observed that the *Nu* does not converge until the non-dimensional time of 300.0. On the other hand, for the result of DVM, an initial fluid temperature in cavity was set as $\theta_i = 0.5$ to achieve fast convergence of turbulent heat transfer. After non-dimensional time 100.0, the Nusselt number converges to the averaged *Nu* suggested by the previous study (Huang, 2018).

In the case of the inversion parameter of 0.5, the flow instability due to temperature gradient is not as strong as in the case of an inversion parameter of 0.0. As a result, the fluid near the hot side stays in the lower region for about 40.0 non-dimensional time, causing *Nu* to decrease below 20 before the upward flow develops. On the other hand, due to the stability of the flow structure, the averaged *Nu* of SSM-SPH and DVM-SPH quickly converges.

The *Nu* number in the SSM-SPH analysis converges to a lower value than the average *Nu* number suggested by previous study (Huang, 2018), and this tendency is more pronounced as the flow develops. This is because the SSM predicts lower temperature gradient near the boundary due to excessive turbulent viscosity modeling. On the other hand, the DVM overpredicts the averaged *Nu* number

comparted to the value suggested by previous study (Huang, 2018) for both cases of $\theta_m = 0.0$ and 0.5. After 100.0 non-dimensional time, the time-spatial averaged Nu for DVM are 73.0682 and 42.0159.

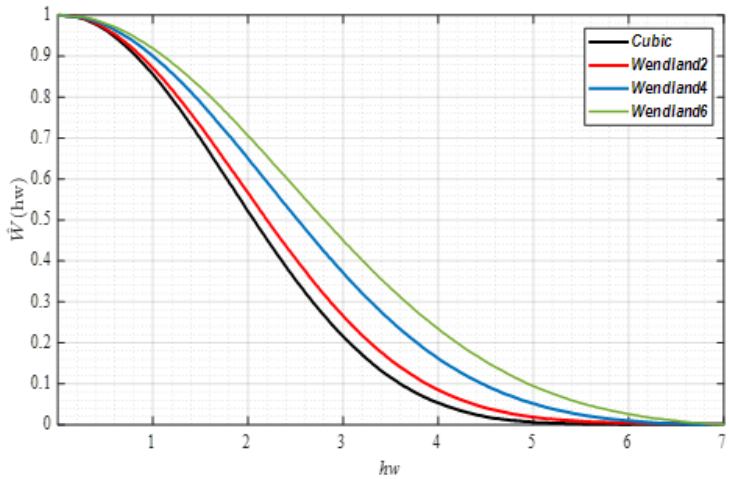

Figure. 3.1. Attenuation factor distribution
(Cubic, Wendland 2/4/6 functions)

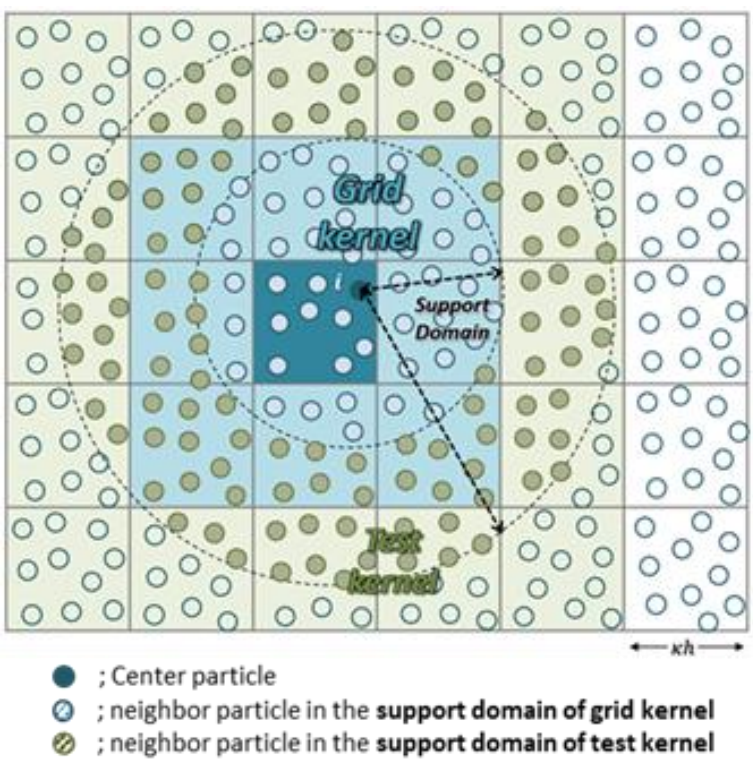

Figure. 3.2. Grid filter and Test filter concept in SPH

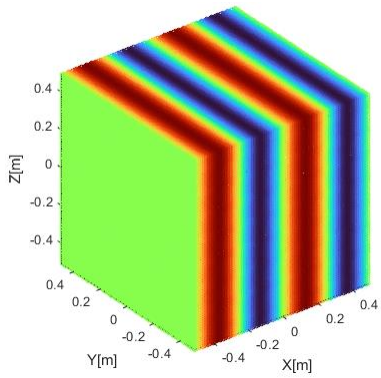

(a) $f_x = sin(4\pi x)$

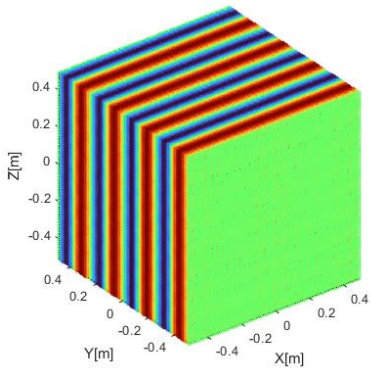

(b) $f_y = sin(8\pi y)$

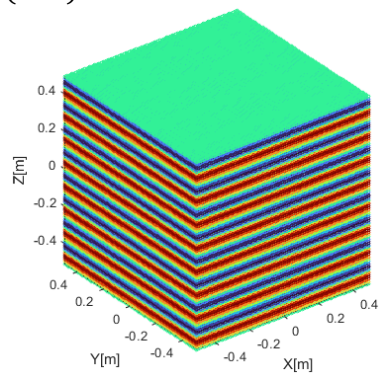

(c) $f_z = sin(8\pi z)$

Figure 3.3. Benchmark for double filtered derivative

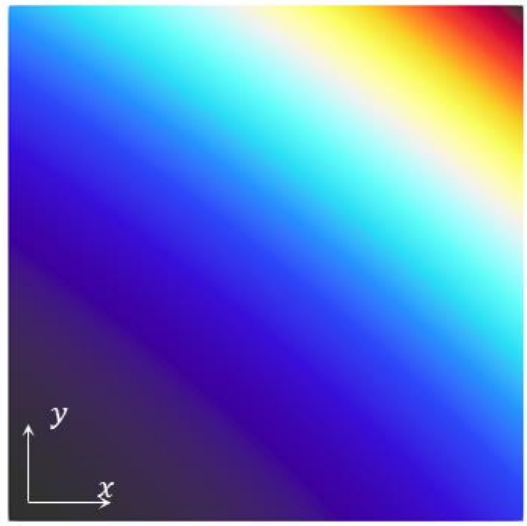

Figure. 3.4. Benchmark for the effect of numerical correction method, spatial resolution and particle distribution

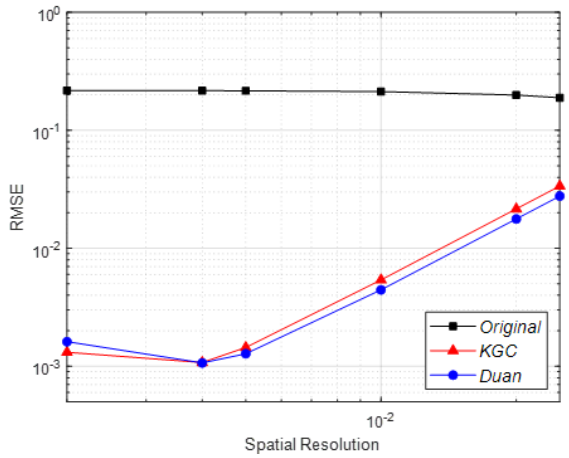

(a) RMSE with regular particle distribution

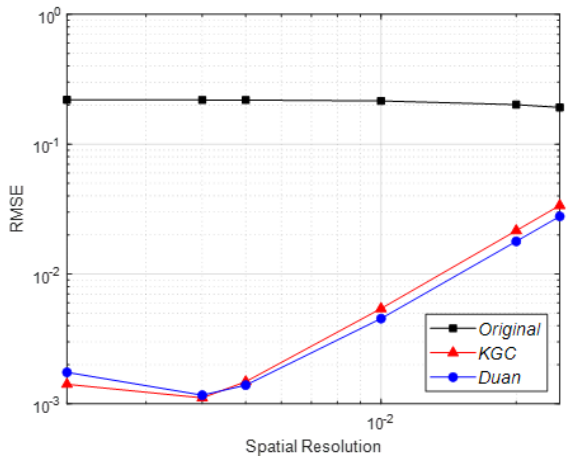

(b) RMSE with irregular distribution (0.1%)

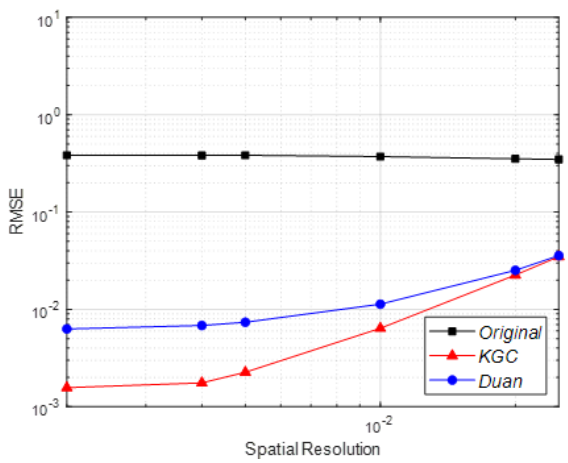

(c) RMSE with irregular distribution (1.0%)

Figure. 3.5 Benchmark for 1st order derivative accuracy

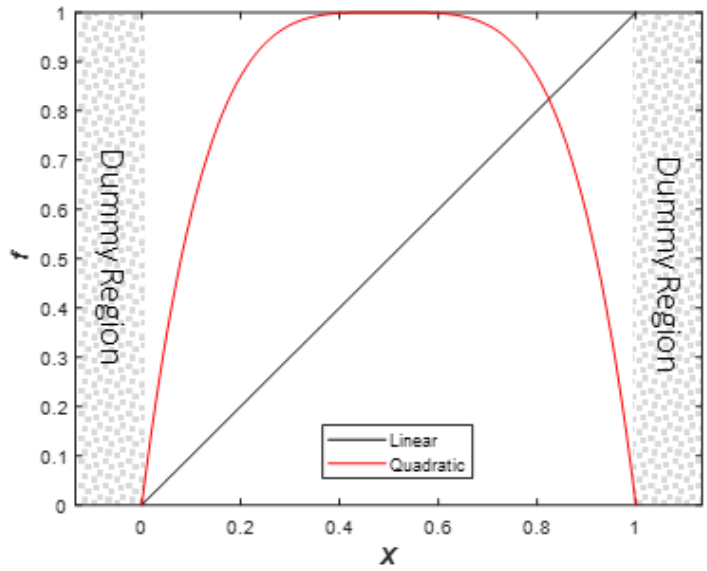

Figure. 3.6. Benchmark for derivative accuracy near boundary

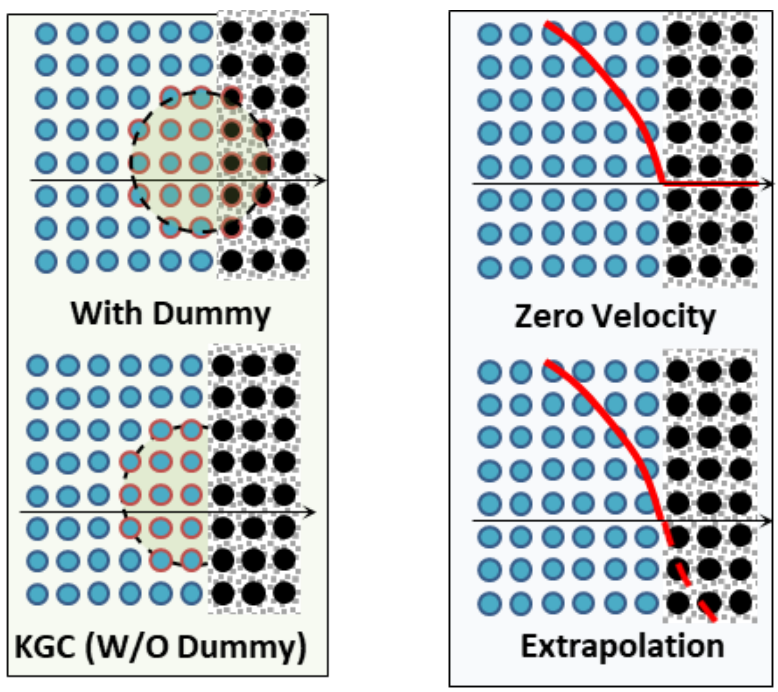

(a) Kernel interpolation range and KGC application

(b) Velocity calculation method in Dummy particle

Figure 3.7. SPH derivative discretization method near wall

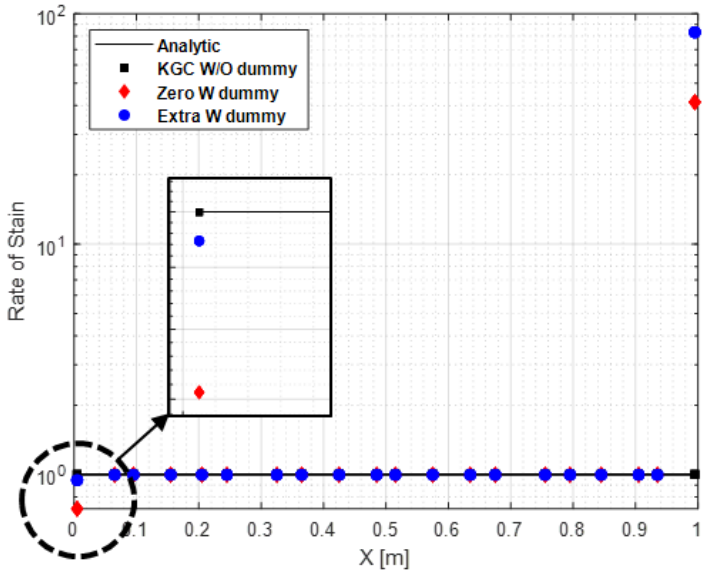

(a) Rate of strain (Linear velocity distribution)

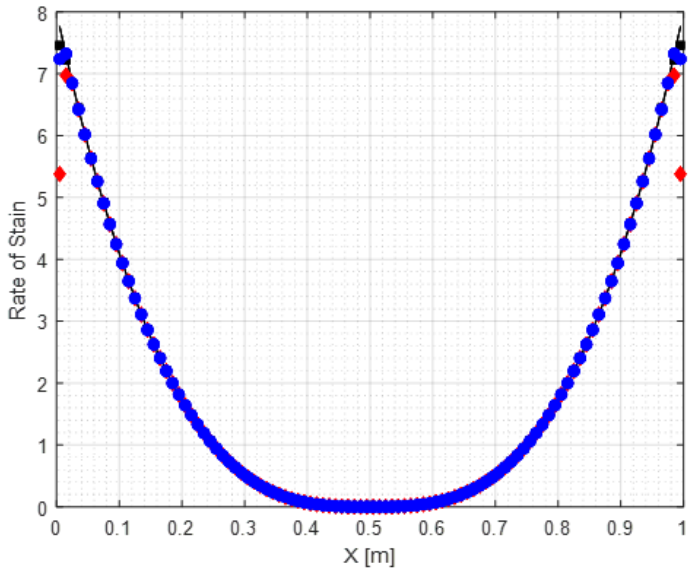

(b) Rate of strain (Quadratic Velocity distribution)

Figure. 3.8. Benchmark results (Rate of Strain)

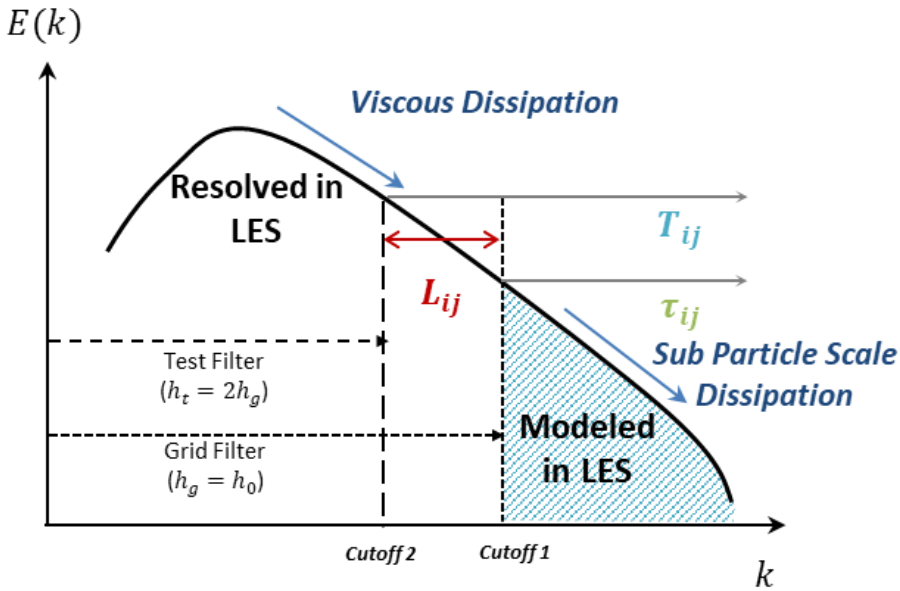

Figure. 3.9. DSM concept in energy spectrum

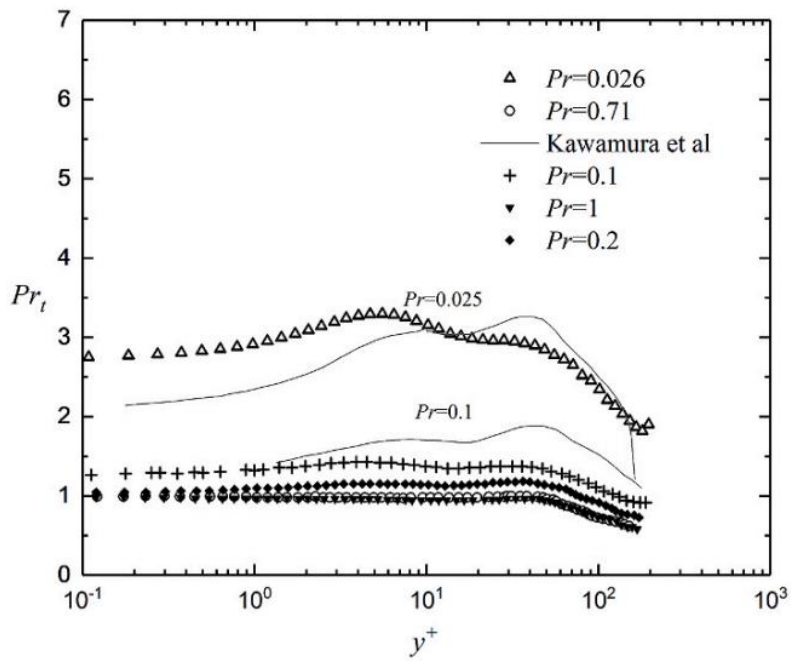

Figure. 3.10. Turbulent Prandtl number distribution of low-Prandtl number fluid (Redjem-Saad, 2007)

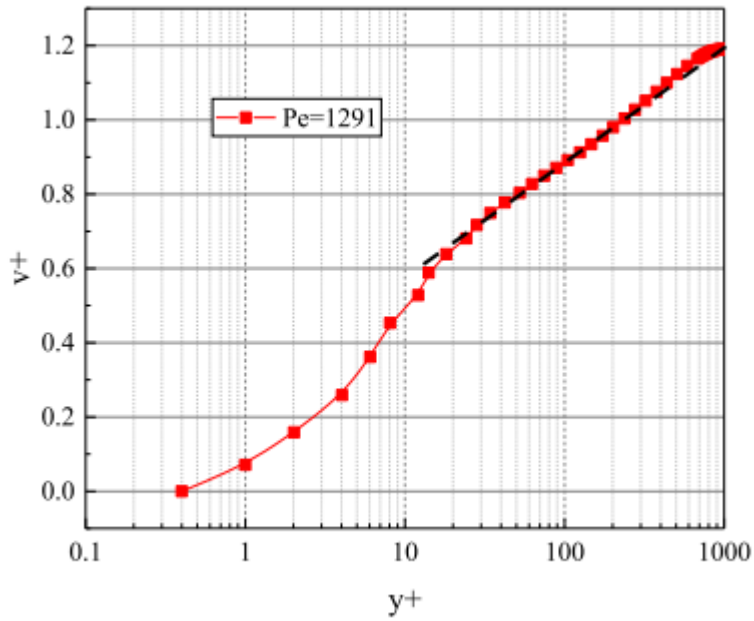

(a)Dimensionless velocity distribution

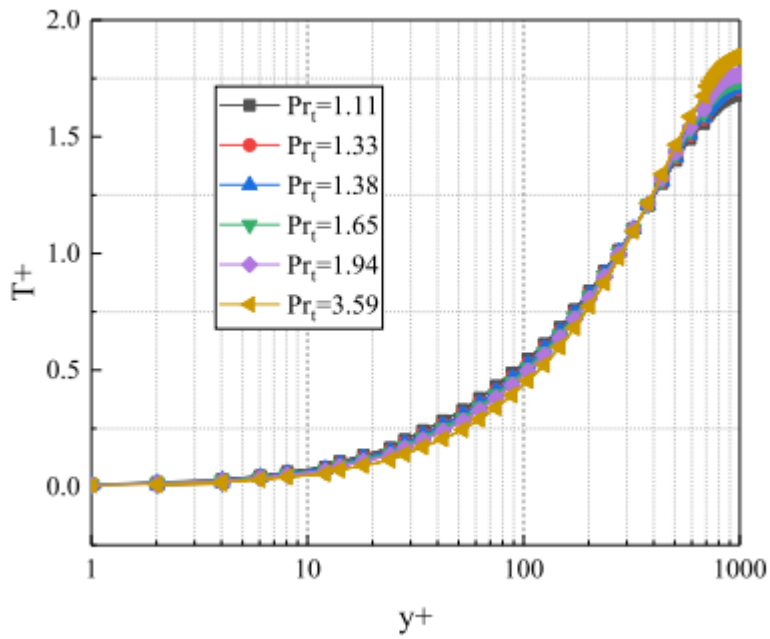

(b)Dimensionless temperature distribution

Figure. 3.11. Dimensionless velocity and temperature distribution in boundary later at different turbulent Pr number (Lei,2022)

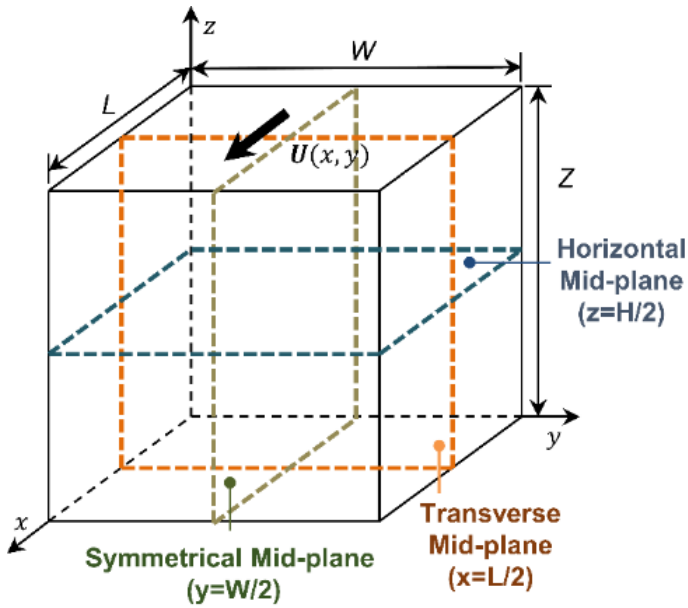

Figure. 3.12. Simulation geometry of cubical cavity flow

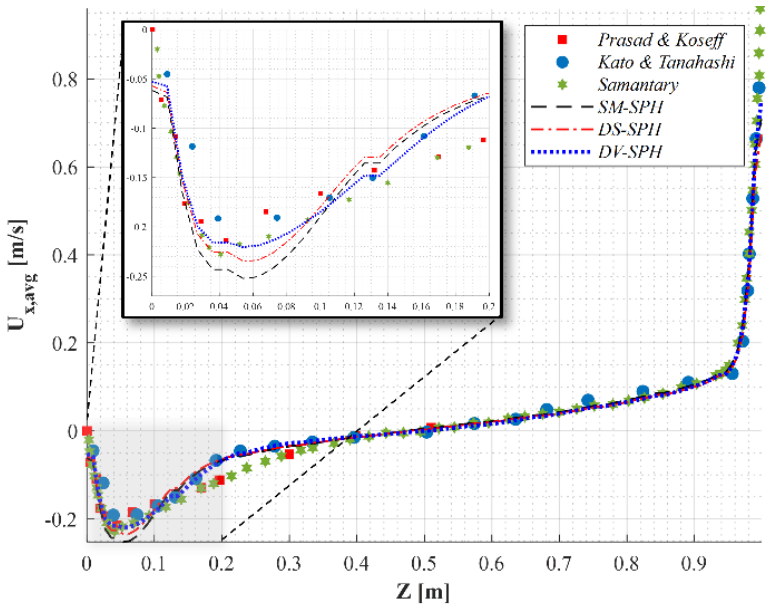

(a)Averaged x directinal velocity at z=Z/2 in transverse mid-plane

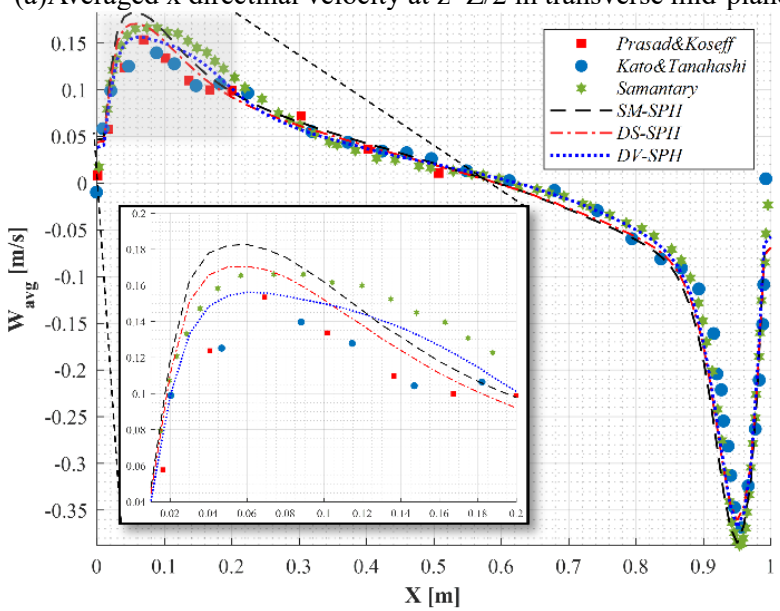

(b)Averaged z directinal velocity at x=L/2 in transverse mid-plane

Figure. 3.13. Averaged velocity profile at Re=5,000
(SM-SPH; Standard Smagorinsky model with SPH model, DS-SPH; Dynamic Smagorinsky model with SPH model, DV-SPH; Dynamic Vreman with SPH model)

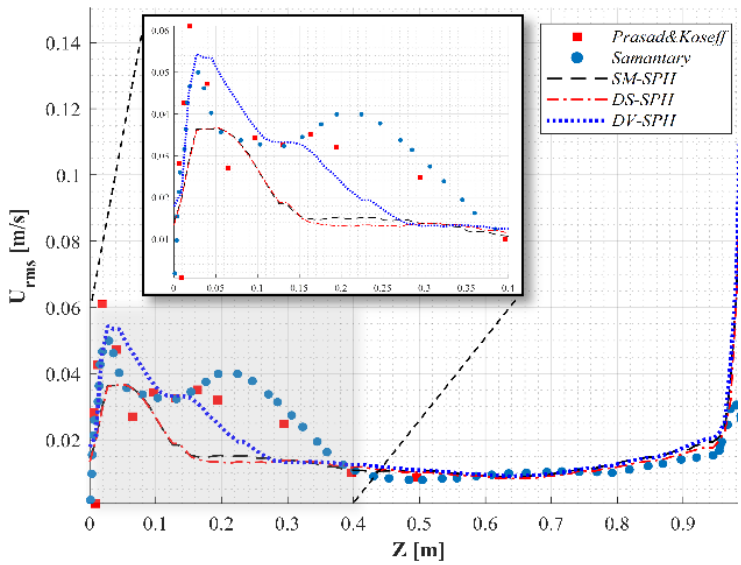

(a)Root mean square of x directinal velocity at z=Z/2 in transverse mid-plane

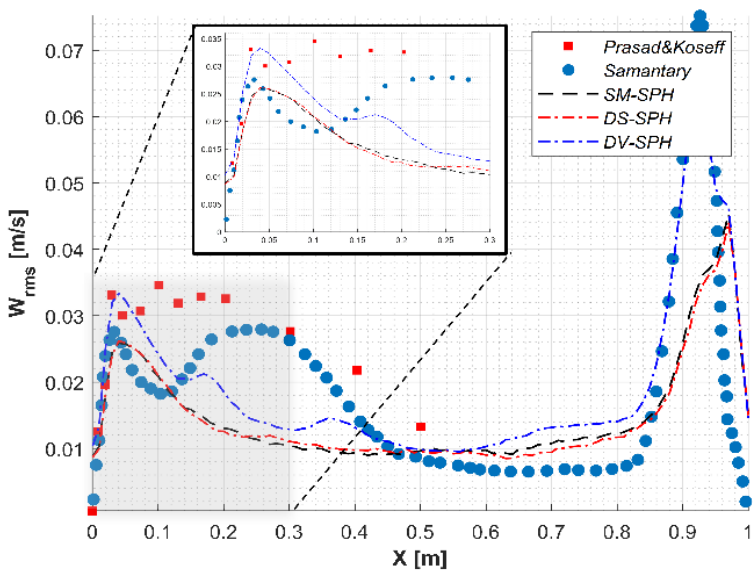

(b)Root mean square of z directinal velocity at x=L/2 in transverse mid-plane

Figure. 3.14. RMS velocity profile at Re=5,000
(SM-SPH; Standard Smagorinsky model with SPH model, DV-SPH; Dynamic Vreman with SPH model)

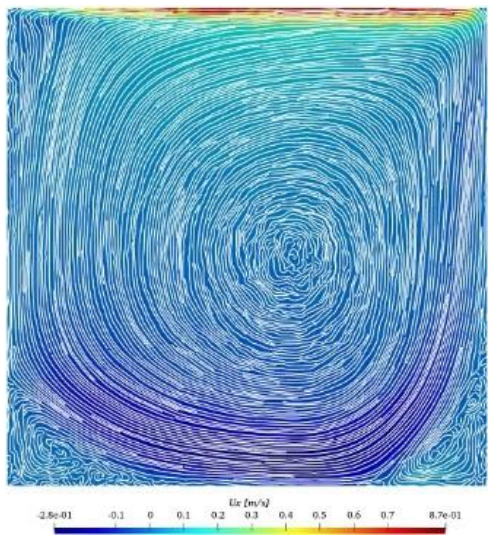

(a) t=100.0s

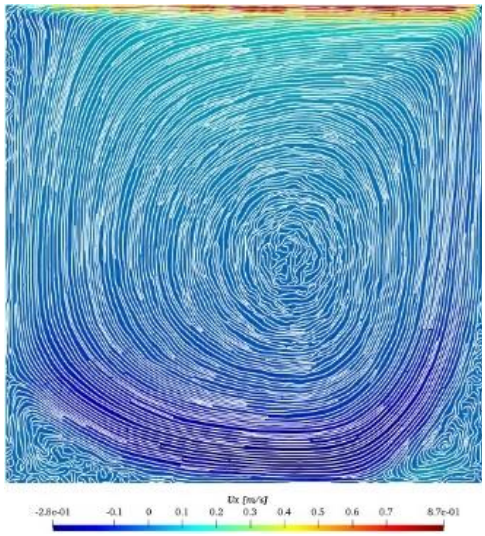

(b) t=200.0s

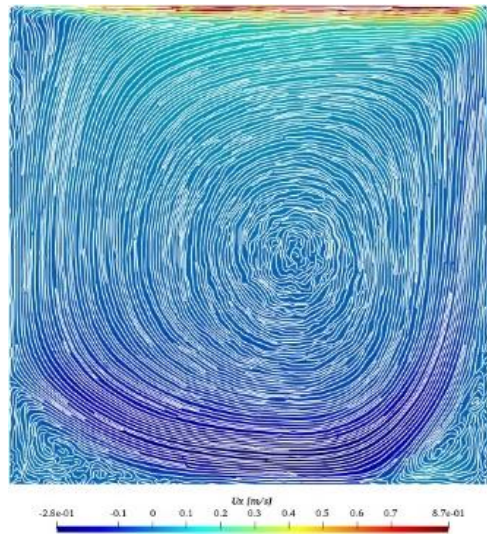

(c) t=300.0s

Figure. 3.15 Streamline with x-directional velocity (SSM)

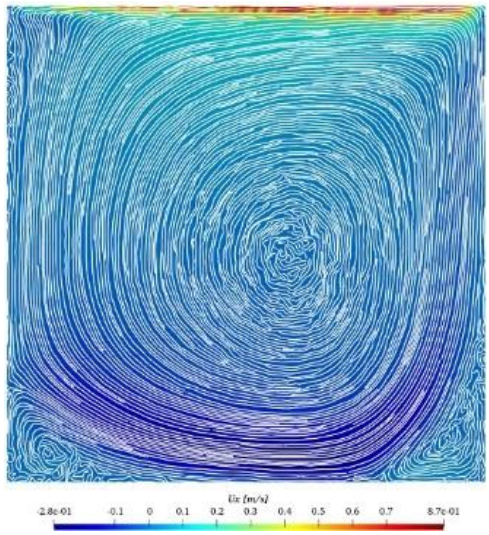

(a) t=100.0s

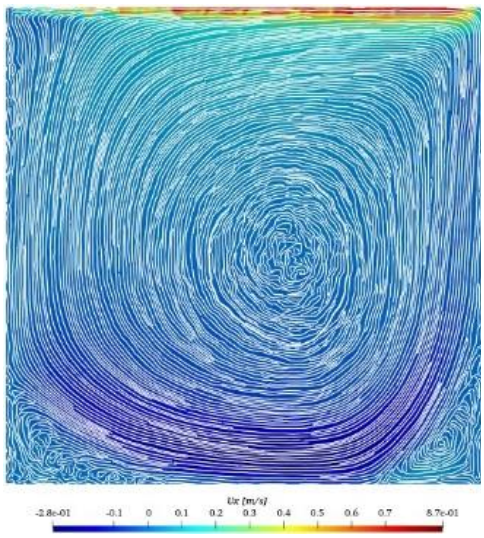

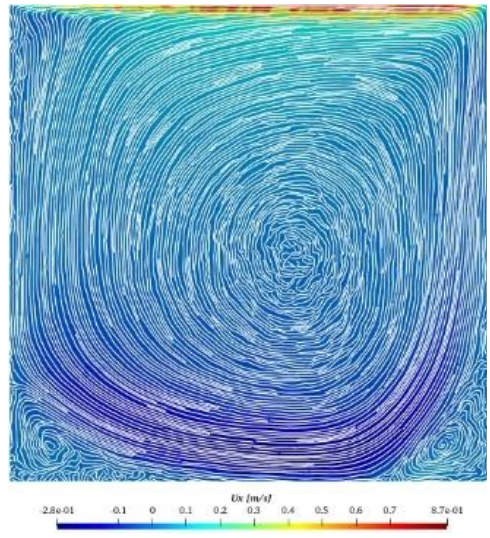

(b) t=200.0s (c) t=300.0s

Figure. 3.16 Streamline with x-directional velocity (DSM)

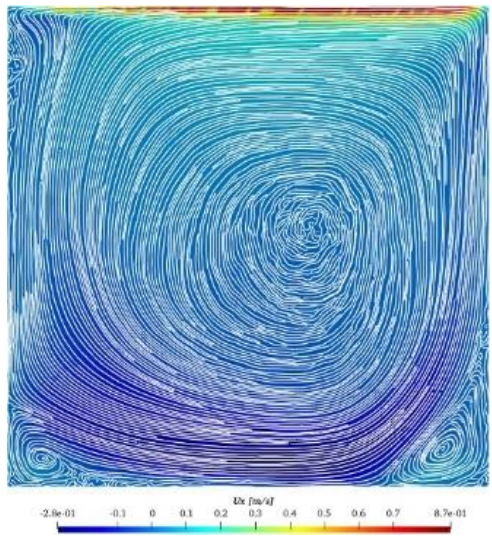

(a) t=100.0s

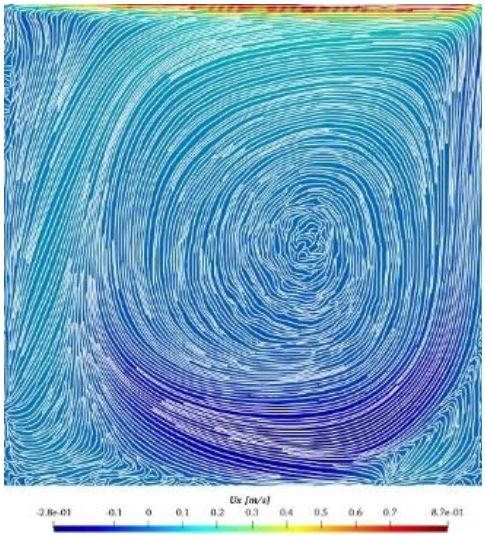

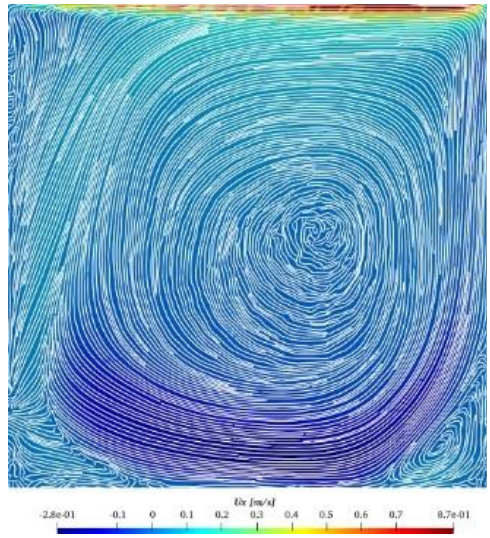

(b) t=200.0s (c) t=300.0s

Figure. 3.17 Streamline with x-directional velocity (DVM)

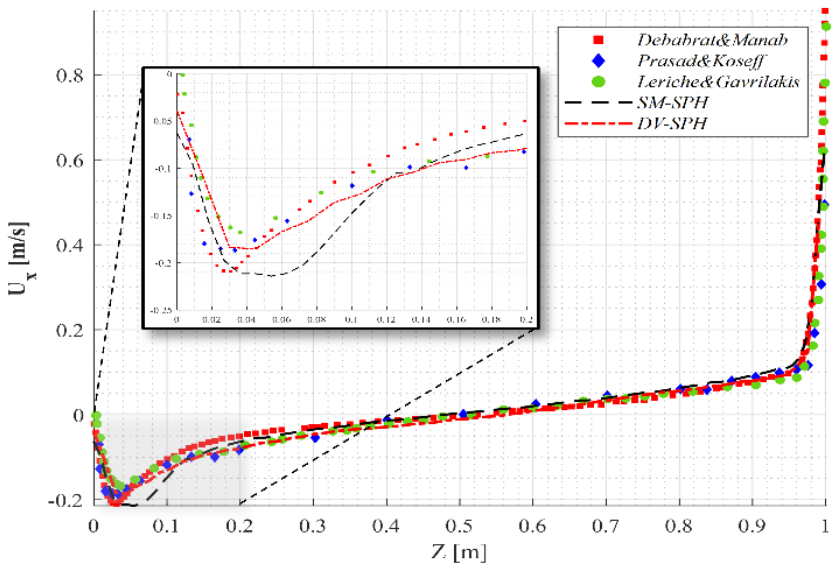

(a)Averaged x directinal velocity at z=Z/2 in transverse mid-plane

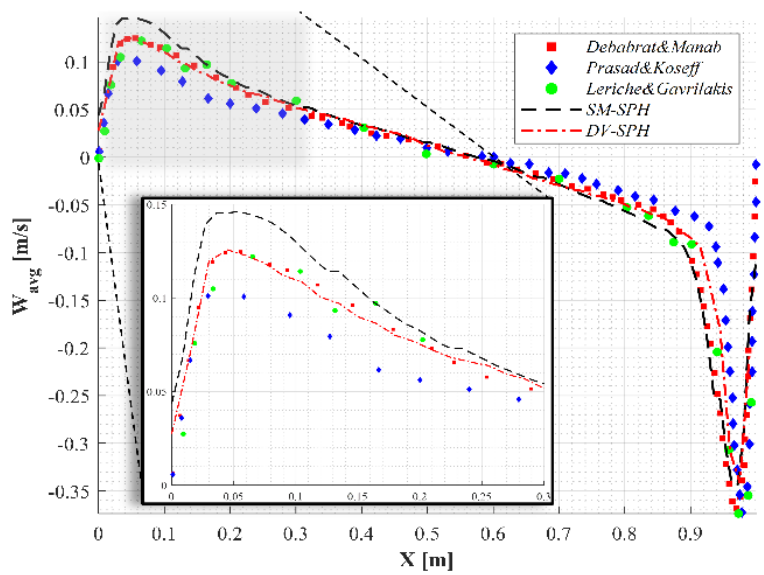

(b)Averaged z directinal velocity at x=L/2 in transverse mid-plane

Figure. 3.18. Averaged velocity profile at Re=12,000
(SM-SPH; Standard Smagorinsky model with SPH model, DV-SPH; Dynamic Vreman with SPH model)

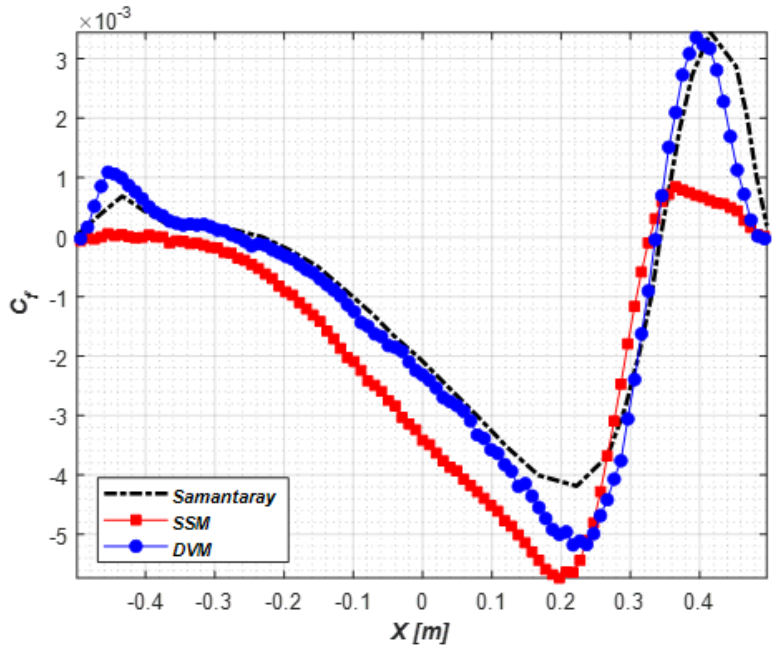

Figure. 3.19 Skin Friction Factor at the bottom (Re=12,000)

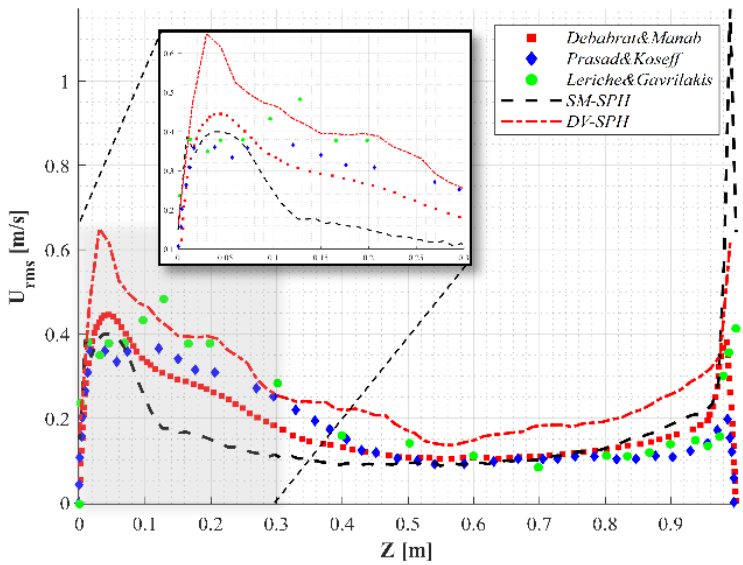

(a)Root mean square of x directinal velocity at z=Z/2 in transverse mid-plane

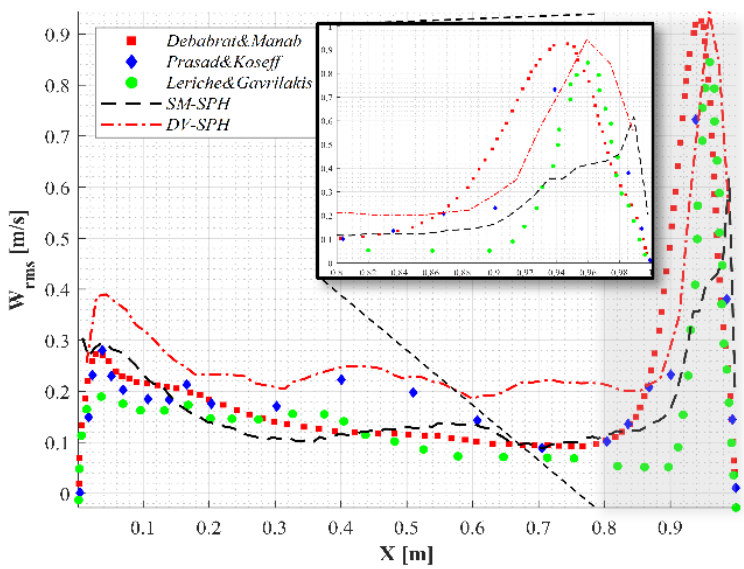

(b)Root mean square of z directinal velocity at x=L/2 in transverse mid-plane

Figure. 3.20. RMS velocity profile at Re=5,000
(SM-SPH; Standard Smagorinsky model with SPH model, DV-SPH; Dynamic Vreman with SPH model)

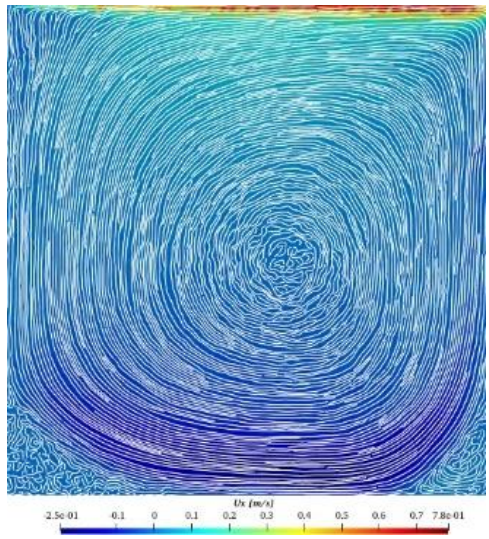

(a) t=100.0s

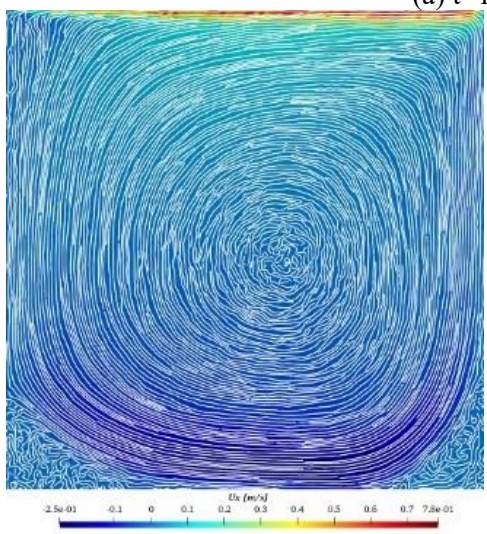

(b) t=200.0s

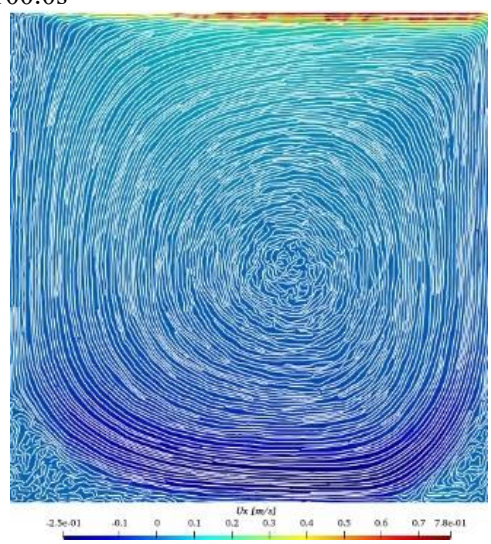

(c) t=300.0s

Figure. 3.21 Streamline with x-directional velocity (SSM)

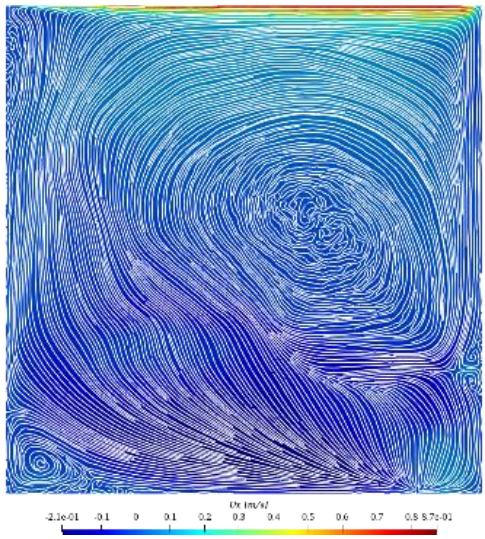

(a) t=100.0s

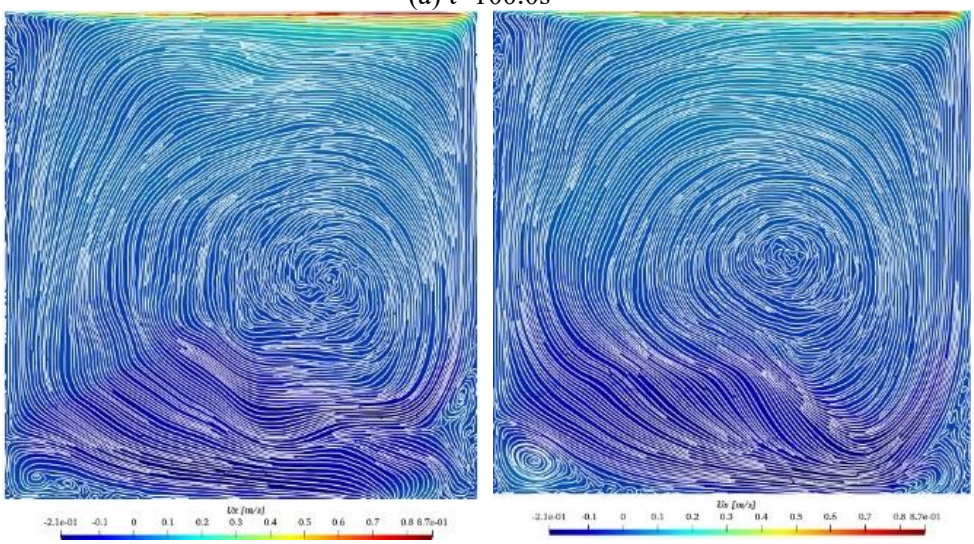

(b) t=200.0s (c) t=300.0s

Figure. 3.22 Streamline with x-directional velocity (DVM)

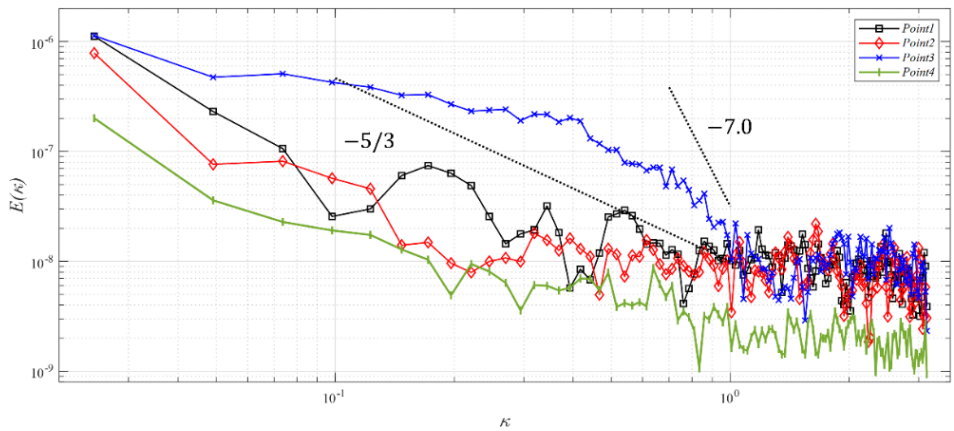

Figure 3.23. Spectral analysis of simulation result of SSM

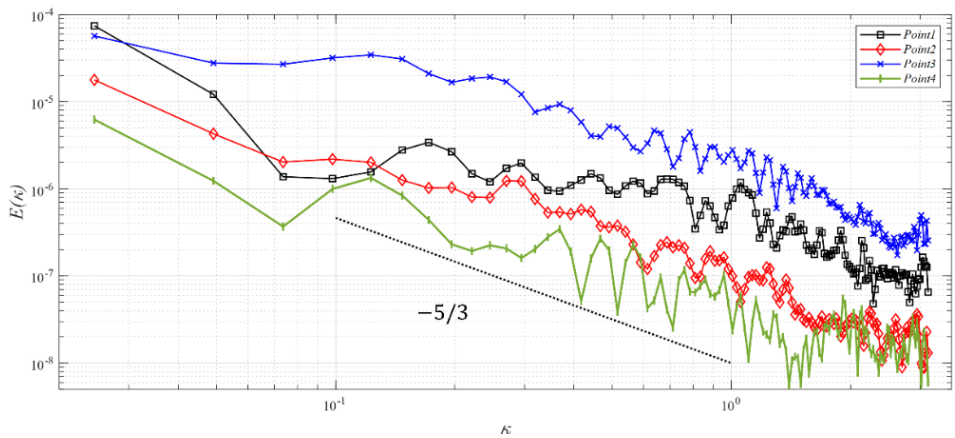

Figure 3.24. Spectral analysis of simulation result of DVM

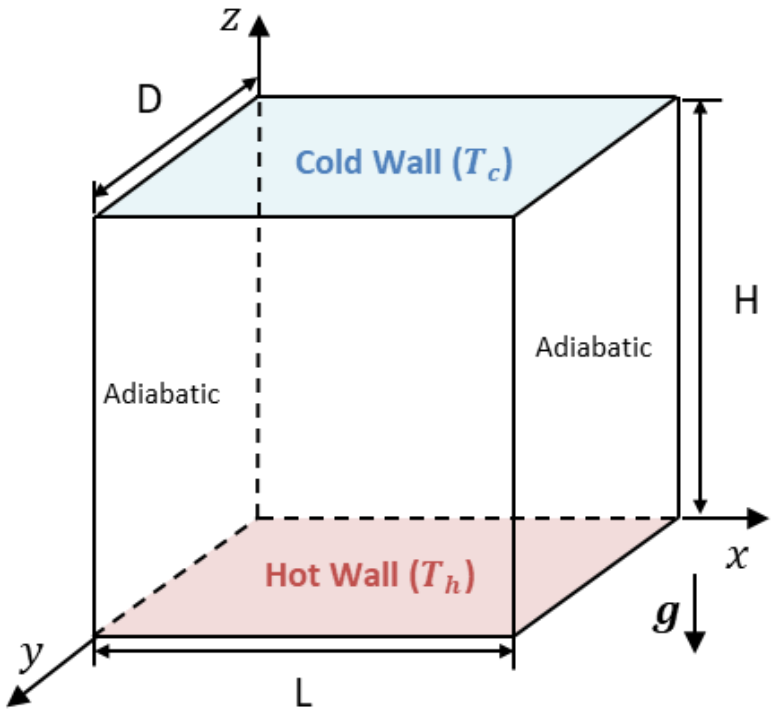

Figure. 3.25 Schematic of Rayleigh-Benard Convection

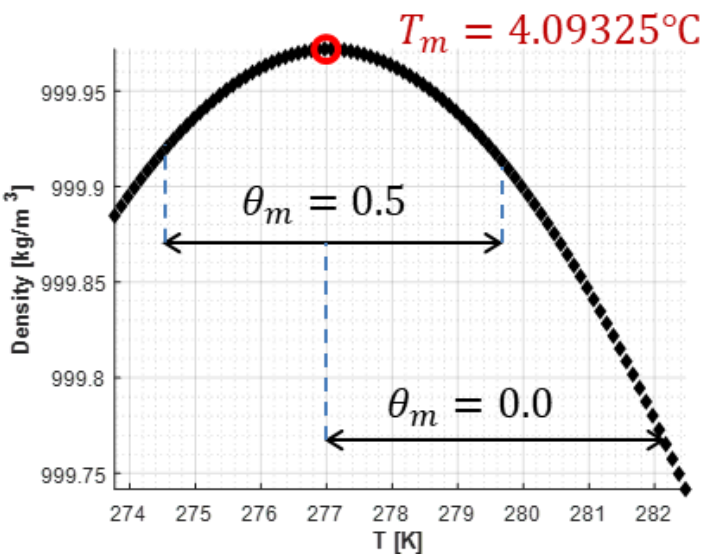

Figure. 3.26 Temperature-Density distribution of water

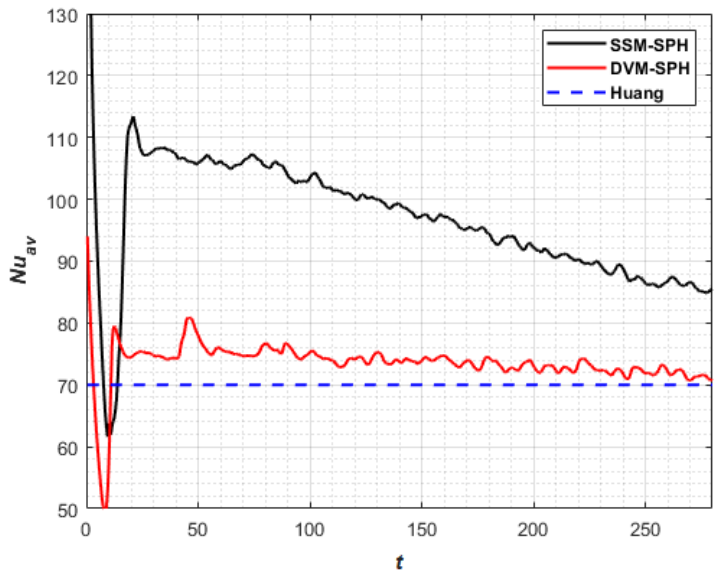

Figure. 3.27 Averaged Nussult number distribution over time (inversion paramter of 0.0)

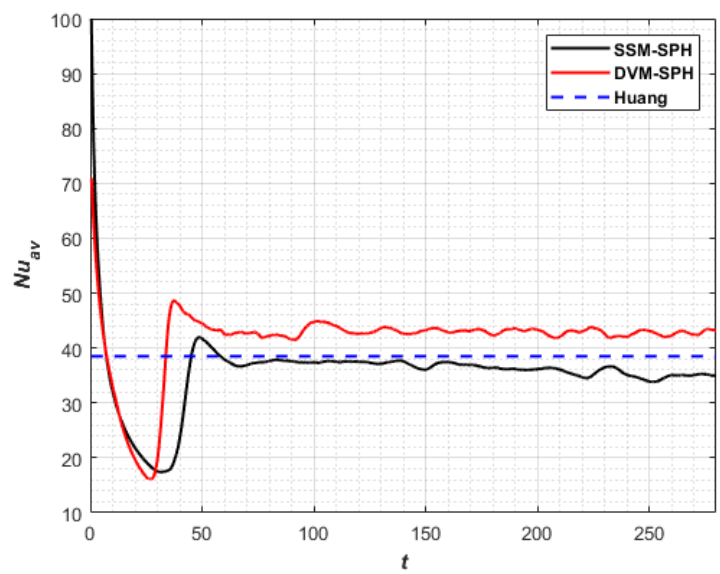

Figure. 3.28 Averaged Nussult number distribution over time (inversion paramter of 0.5)

Table 3.1. RMSE of double filtered derivative method

	X direction	**y direction**	**z direction**
Equation 3.10	0.0487	0.0911	0.1506
Equation 3.11	0.0335	0.0642	0.1185

Table 3.2. SPH discretization of DSM in grid filter scale

Grid Filter Scale	**SPH discretization**
	$\bar{u}_{a,i}$ $\quad \bar{u}_{a,i} = \sum_{j \in f} \frac{m_j}{\rho_j}(u_{b,j}) W_{ij,g} \Big/ \sum_{j \in f} \frac{m_j}{\rho_j} W_{ij,g}$
$\tau_{ab} = 2C_d \alpha_{ab}$	$\lvert\bar{S}\rvert_i$ $\quad \lvert\bar{S}\rvert_i = \sqrt{2\bar{S}_{ab,i}\bar{S}_{ab,i}}$
$\alpha_{ab} = h^2 \lvert\bar{S}\rvert \bar{S}_{ab}$	$\bar{S}_{ab,i}$ $\quad \bar{S}_{ab,i} = \frac{1}{2}\left\{ \sum_{j \in f} \frac{m_j}{\rho_j}(u_{a,j} - u_{a,i}) \nabla_i W_{ij,g} + \sum_{j \in f} \frac{m_j}{\rho_j}(u_{b,j} - u_{b,j}) \nabla_i W_{ij,g} \right\}$

Table 3.3. SPH discretization of DSM model in test filter scale

Test Filter Scale	**SPH discretization**	
$T_{ab} = 2C_d\beta_{ab}$	$\tilde{\bar{u}}_{a,i}$	$\tilde{\bar{u}}_{a,i} = \sum_{j\in f}\frac{m_j}{\rho_j}(\bar{u}_{a,j})W_{ij,t}\Big/\sum_{j\in f}\frac{m_j}{\rho_j}W_{ij,t}$
$\beta_{ab} = \tilde{h}^2\tilde{\bar{S}}\tilde{\bar{S}}_{ab}$	$\widetilde{\bar{u}_{a,\iota}\bar{u}_{a,\iota}}$	$\sum_{j\in f}\frac{m_j}{\rho_j}(\bar{u}_{a,j}\bar{u}_{b,j})W_{ij,t}\Big/\sum_{j\in f}\frac{m_j}{\rho_j}W_{ij,t}$
$L_{ab} = \widetilde{\bar{u}_a\bar{u}_b} - \tilde{\bar{u}}_a\tilde{\bar{u}}_b = 2C_d\Delta^2 M_{ab}$	$\tilde{\bar{S}}_{ab,i}$	$\tilde{\bar{S}}_{ij} = \sum_{j\in f}\frac{m_j}{\rho_j}(\bar{S}_{ab,j})W_{ij,t}\Big/\sum_{j\in f}\frac{m_j}{\rho_j}W_{ij,t}$
	$\lvert\tilde{\bar{S}}\rvert_i$	$\lvert\tilde{\bar{S}}\rvert_i = \sqrt{2\tilde{\bar{S}}_{ab,i}\tilde{\bar{S}}_{ab,i}}$
$M_{ab} = (\tilde{h}^2/\ h^2)\lvert\tilde{\bar{S}}\rvert\tilde{\bar{S}}_{ab} - \widetilde{\lvert\bar{S}\rvert\bar{S}_{ab}}$	$\widetilde{\lvert\bar{S}\rvert_\iota\bar{S}_{ab,\iota}}$	$\widetilde{\lvert\bar{S}\rvert_\iota\bar{S}_{ab,\iota}} = \sum_{j\in f}\frac{m_j}{\rho_j}(\lvert\bar{S}\rvert_j\bar{S}_{ab,j})W_{ij,t}\Big/\sum_{j\in f}\frac{m_j}{\rho_j}W_{ij,t}$

Table 3.4. Volume averaging method in DSM model

Volume Averaging	**SPH discretization**
$C_d h^2 = \left\langle\frac{1}{2}\frac{L_{ab}M_{ab}}{M_{ab}M_{ab}}\right\rangle_{\boldsymbol{V}}$	$f_j = \frac{1}{2}\frac{L_{ab}M_{ab}}{M_{ab}M_{ab}}, \qquad C_d h^2 = \frac{\sum_j \frac{m_j}{\rho_j} f_j W_{ij,g}}{\sum_j \frac{m_j}{\rho_j} W_{ij,g}}$

Table 3.5. SPH discretization of DVM in grid filter scale.

Grid Filter Scale	**SPH discretization**	
$\bar{\alpha}_{ab} = \frac{\partial\bar{u}_b}{\partial x_a}$	$\bar{\alpha}_{ab,i}$	$\bar{\alpha}_{ab,i} = \sum_{j\in f}\frac{m_j}{\rho_j}\left(u_{b,j} + u_{b,i}\right)\frac{\partial W_{ij,g}}{\partial x_a}$
$\overline{\frac{\partial\theta}{\partial x_a}}$	$\overline{\frac{\partial\theta}{\partial x_a}}$	$\overline{\frac{\partial\theta}{\partial x_a}} = \sum_{j\in f}\frac{m_j}{\rho_j}\left(\theta_j + \theta_i\right)\frac{\partial W_{ij,g}}{\partial x_a}$

Table 3.6. SPH discretization of DVM in test filter scale.

Test Filter Scale	SPH discretization	
$\hat{\bar{\alpha}}_{ab}$	$\hat{\bar{\alpha}}_{ab}$	$\hat{\bar{\alpha}}_{ab,i} = \sum_{j\in f} \frac{m_j}{\rho_j}(\bar{\alpha}_{ab,j})W_{ij,t} \Big/ \sum_{j\in f} \frac{m_j}{\rho_j} W_{ij,t}$
$\widehat{\bar{\alpha}_{ab}\bar{\alpha}_{ab}}$	$\widehat{\bar{\alpha}_{ab}\bar{\alpha}_{ab}}$	$\sum_{j\in f} \frac{m_j}{\rho_j}(\bar{\alpha}_{ab,j}\bar{\alpha}_{ab,j})W_{ij,t} \Big/ \sum_{j\in f} \frac{m_j}{\rho_j} W_{ij,t}$
$\hat{\bar{S}}_{ab}$	$\hat{\bar{S}}_{ab}$	$\hat{\bar{S}}_{ab} = \sum_{j\in f} \frac{m_j}{\rho_j}(\bar{S}_{ab,j})W_{ij,t} \Big/ \sum_{j\in f} \frac{m_j}{\rho_j} W_{ij,t}$
$\Pi^g \widehat{\bar{S}_{ab}\bar{S}_{ab}}$	$\Pi^g \widehat{\bar{S}_{ab}\bar{S}_{ab}}$	$\sum_{j\in f} \frac{m_j}{\rho_j}\left(\Pi_j^g \bar{S}_{ab,j}\bar{S}_{ab,j}\right)W_{ij,t} \Big/ \sum_{j\in f} \frac{m_j}{\rho_j} W_{ij,t}$
$\widehat{\frac{\partial\bar{\theta}}{\partial x_a}}$	$\widehat{\frac{\partial\bar{\theta}}{\partial x_a}}$	$\widehat{\frac{\partial\bar{\theta}}{\partial x_a}} = \sum_{j\in f} \frac{m_j}{\rho_j}\left(\frac{\partial\bar{\theta}}{\partial x_a}\right)W_{ij,t} \Big/ \sum_{j\in f} \frac{m_j}{\rho_j} W_{ij,t}$
$\widehat{\frac{\partial\bar{\theta}}{\partial x_a}\frac{\partial\bar{\theta}}{\partial x_a}}$	$\widehat{\frac{\partial\bar{\theta}}{\partial x_a}\frac{\partial\bar{\theta}}{\partial x_a}}$	$\widehat{\frac{\partial\bar{\theta}}{\partial x_a}\frac{\partial\bar{\theta}}{\partial x_a}} = \sum_{j\in f} \frac{m_j}{\rho_j}\left(\frac{\partial\bar{\theta}}{\partial x_a}\frac{\partial\bar{\theta}}{\partial x_a}\right)W_{ij,t} \Big/ \sum_{j\in f} \frac{m_j}{\rho_j} W_{ij,t}$
$\Pi^g \widehat{\frac{\partial\bar{\theta}}{\partial x_a}\frac{\partial\bar{\theta}}{\partial x_a}}$	$\Pi^g \widehat{\frac{\partial\bar{\theta}}{\partial x_a}\frac{\partial\bar{\theta}}{\partial x_a}}$	$\Pi^g \widehat{\frac{\partial\bar{\theta}}{\partial x_a}\frac{\partial\bar{\theta}}{\partial x_a}} = \sum_{j\in f} \frac{m_j}{\rho_j}\Pi^g \frac{\partial\bar{\theta}}{\partial x_a}\frac{\partial\bar{\theta}}{\partial x_a} W_{ij,t} \Big/ \sum_{j\in f} \frac{m_j}{\rho_j} W_{ij,t}$

Table 3.7. Volume averaging method in DSM model

Volume Averaging	SPH discretization
$\langle f \rangle_V$	$N_V = \begin{cases} \frac{m_i}{\rho_i} f_i & if\ i \in fluid \\ 0 & if\ i \notin fluid \end{cases}$ $D_V = \begin{cases} \frac{m_i}{\rho_i} & if\ i \in fluid \\ 0 & if\ i \notin fluid \end{cases}$ $\langle f \rangle_V = \frac{\sum_j N_{V,j}}{\sum_j D_{V,j}}$

Table 3.8. Global model for turbulent *Pr* model

Author	Pr_t Model
Aoki (1963)	$Pr_t^{-1} = 0.014Re^{0.45}Pr^{0.2}\left[1 - \exp\left(-\frac{1}{0.014Re^{0.45}Pr^{0.2}}\right)\right]$
Reynolds (1975)	$Pr_t = (1 + 100Pe^{-0.5})\left(\frac{1}{1 + 120Re^{-0.5}} - 0.15\right)$
Jischa and Rieke (1979)	$Pr_t = 0.9 + \frac{182.4}{PrRe^{0.884}}$ (For liquid Sodium, Pr = 0.007)
Myong (1989)	$Pr_t = 0.75 + \frac{1.63}{\ln(1 + Pr/0.0015)}$
Cheng&Tak (2006)	$Pr_t = \begin{cases} 4.12 & (Pe \le 1{,}000) \\ \frac{0.01Pe}{[0.018Pe^{0.8} - (7.0 - A)]^{1.25}} & (1{,}000 < Pe \le 6{,}000) \end{cases}$ $A = \begin{cases} 5.4 - 9 \times 10^{-4} & (1{,}000 < Pe \le 2{,}000) \\ 3.6 & (2{,}000 < Pe \le 6{,}000) \end{cases}$
Dawid Taler (2018)	$Pr_t^{-1} = 0.01592Re^{0.45}Pr^{0.2}\left[1 - exp\left(-\frac{1}{0.01592Re^{0.45}Pr^{0.2}}\right)\right]$

Table 3.9. Local model for turbulent *Pr* model

Author	Pr_t Model
Hollingsworth (1989)	$Pr_t = 1.85 - \tanh[0.2(y^+ - 7.5)]$ (For water)
Kays and Crawford (1993)	$Pr_t = \frac{1}{0.5882 + 0.228\frac{\mu_t}{\mu} - 0.0441\left(\frac{\mu_t}{\mu}\right)^2\left[1 - exp\left(-\frac{5.165}{\mu_t/\mu}\right)\right]}$
Kays (1994)	$Pr_t = \begin{cases} 1.07 & \mu_t/\mu < 0.2 \\ 0.85 + \frac{2}{Pe_t} & \mu_t/\mu \ge 0.2 \end{cases}$

Table 3.10 Simulation condition of RB convection

$\boldsymbol{Ra}$	$\boldsymbol{Pr}$	
1.0×10^9	11.573	
$\boldsymbol{\theta_m}$	$\boldsymbol{T_h}$ $[\boldsymbol{K}]$	$\boldsymbol{T_c}$ $[\boldsymbol{K}]$
0.0	282.52	277.18
0.5	279.85	274.51

Table 3.11 Initial condition of RB convection

$\boldsymbol{\theta_m}$	**Particle Size**	$\boldsymbol{T_{init}}$ $\boldsymbol{[K]}$ $\boldsymbol{at\ \theta_m = 0.0}$	$\boldsymbol{T_{init}}$ $\boldsymbol{[K]}$ $\boldsymbol{at\ \theta_m = 0.5}$
SSM-SPH	$L/200$	277.18 ($\theta_i = 0.0$)	277.18 ($\theta_i = 0.0$)
DVM-SPH	$L/125$	279.85 ($\theta_i = 0.5$)	277.71 ($\theta_i = 0.6$

Chapter 4 Phase Change Model for SPH

4.1. Enthalpy-Based Phase Change Model for SPH

A phase change model based on enthalpy was implemented to determine the particle phase and analyze thermal ablation. Compared to a temperature-based phase change model (Farrokhpanah, 2017), this method has the advantage of not requiring a numerical melting temperature range and not having concerns about bypassing latent heat due to large temperature changes when using relatively large timesteps (Wang, 2020). Figure 4.1(a) depicts the temperature-based phase change model, while Figure 4.2(b) illustrates the enthalpy-based phase change model.

The SPH particles in the latent heat range were identified as particles undergoing phase change. The physical properties such as thermal conductivity and thermal diffusivity of the SPH particles located at the phase interface were linearly interpolated based on the liquid and solid properties at the melting temperature, with enthalpy as the reference parameter.

4.1.1 PPE Analysis for SPH Phase-Change Model

In this research, EISPH is used as a pressure solver to obtain the pressure field of the fluid by solving Equation 2.18 (Barcarolo, 2013). The Density Invariance (DI) method, described by Equation 2.22, is employed as a discretization for the PPE source term, assuming that the particle distribution in the previous step is in a completely incompressible state.

However, in the case of natural convection accompanying thermal ablation, SPH particles continuously move in a specific direction. Due to the nature of the explicit PPE solver, a minor numerical error in particle incompressibility, as shown in Figure 4.2, can occur. This compressed particle distribution is then used as the reference distribution assuming incompressibility in the DI source term for the next timestep, leading to an intensified flow compression. As the compression intensifies, fluid SPH particles can experience penetration at the solid-liquid boundary, resulting in distorted flow analysis.

Therefore, in this study, the DI source term in the PPE is modified as shown in Equation 4.1. The superscript f denotes a filter, and unlike Equation 2.22, which calculates the term using the particle distribution of each step, the term in Equation 4.1 is updated at each filtering frequency to improve incompressibility maintenance according to the particle distribution.

$$\nabla^2 P^{n+1} = \frac{\rho_0 - \rho^{pr}}{\Delta t^2} = \frac{\rho_0 \left[1 - \frac{\sum_j W(\boldsymbol{x}_{ij}^{pr}, h) \frac{m_j}{\rho_j}}{\sum_j W\left(x_{ij}^{f}, h\right) \frac{m_j}{\rho_j}} \right]}{\Delta t^2} \tag{4.1}$$

By updating reference particle position at each filtering frequency, the incompressibility maintenance based on the particle distribution was improved, and in this study, reference particle position is updated every two time-steps.

4.1.2 Enthalpy-Porosity Model For Mushy Zone

In previous research (Russel, 2018; Wang, 2020; Cummins, 2021) on phase change using SPH method, viscosity and thermal conductivity modeling based on enthalpy or temperature were performed to analyze the flow in the mushy zone.

However, the accuracy of flow analysis at the phase interface can vary depending on the viscosity modeling approach, and excessive turbulent effects may occur when applying turbulent models such as the DVM. Therefore, in this study, the Enthalpy-Porosity Model (EPM), commonly used in conventional CFD for mushy zone analysis, was introduced to analyze the behavior of particle undergoing phase change.

In the mushy zone as shown in Figure 4.3, it is in a two-phase state with a mixture of liquid and solid, and the EPM assumes it as a porous media for flow analysis. In conventional CFD research using EPM (Brent, 1988), the Kozeny-Carman equation, commonly used for momentum sink modeling in porous media, was applied as the momentum sink term in the mushy zone, and the momentum and energy transfer equation were implicitly solved. The momentum sink term is given by Equation 4.2, where C_k is the model coefficient, superscript fpr denotes momentum sink term by EPM, and γ represents porosity, defined in Equation 4.3. L, H_l and H denote latent heat, saturated liquid enthalpy and enthalpy of SPH particle.

$$\left(\frac{Du}{Dt}\right)_i^{fpr} = -\frac{C_k(1-\gamma)^2 u_i^n}{\gamma^3 \rho} \tag{4.2}$$

$$\gamma = \frac{(H - H_l)}{L} \tag{4.3}$$

In this study, where an explicit ISPH solver is adopted using the projection time integration method, the momentum sink term can be applied in the projection time step or correction time step, as shown in Table 4.1 and Table 4.2.

When applied in the projection step, an increase in the model coefficient

C_k can lead to non-physical results, where the effect of the momentum sink term becomes dominant over viscous force and other body forces. This requires very fine time resolution or small model coefficient for a stable analysis. To address this limitation, the present study incorporates the momentum sink term in the correction step and models the term as an attenuation factor acting on the velocity in the next time step. With this explicit EPM for SPH method, it was confirmed that stable and accurate analysis can be achieved within the model coefficient range ($C_k > 10^5$) proposed in conventional CFD method.

4.2. Validation and Verification

4.2.1 2D Stefan Solidification Problem

A solidification problem of a 2D square (Farrokhpanah, 2017) has been analyzed. This benchmark was conducted to validate the method for defining the position phase interface. Abrupt temperature drop in external square below melting point leads to solidification and transient change in phase front. This analysis solely considers heat transfer through conduction and doesn't include thermal flow analysis.

The analysis conditions are determined by the properties and temperature boundary condition of working fluid and the schematic is presented in Figure 4.3. To determine the analysis conditions, non-dimensional temperature (T_i^*), distance (x^*), and Stefan number (St) are used, which are given by Equation 4.4 to 4.6. Here, T_m and T_w represent the melting temperature and wall temperature.

$$T_i^* = \frac{k_l}{k_s}\frac{T_i - T_m}{T_m - T_w} \tag{4.4}$$

$$x^* = \frac{x}{(4\alpha t)^{0.5}} \tag{4.5}$$

$$\beta^* = \frac{1}{St} = \frac{L}{C_{p,s}(T_m - T_w)} \tag{4.6}$$

The analysis conditions are set as follows : $T_i^* = 0.3,\ \beta^* = 0.25,\ {}^{k_l}/_{k_s} = 1.0$. The analytic solution for the non-dimensional phase front is given by Equation 4.7, where the constant was set as follow: $C = 0.159,\ m^* = 5.02$ and $\lambda = 0.708$. The position of the phase front in the diagonal direction is determined by Equation 4.8.

$$f(x^*) = \left[\lambda^{m^*} + \frac{C}{x^* m^* - \lambda^{m^*}}\right]^{\frac{1}{m^*}} \tag{4.7}$$

$$f(x^*) = 0.8958 \tag{4.8}$$

A sensitivity study on the spatial resolution was performed for $(2a/dx, 2a/dy)$ values of (100,100), (200,200), and (250, 250). In Fig. 4.4, the position of the phase front in the diagonal direction of the analysis domain was plotted over time, demonstrating that the definition method for position of phase front in this study was appropriate, and results of all spatial resolutions showed the same trend as the analytic solution. In Figure 4.5, the phase front over time was displayed for the entire analytical domain, and the sensitivity of the simulation results to the spatial resolution in all directions was examined.

4.2.2 2D Thermal ablation with natural convection

The 2D melting phenomenon with natural convection under laminar conditions was investigated to validate the thermal flow analysis and phase change modeling framework based on EISPH solver. The analytic results were compared and verified against the previous research obtained through conventional CFD (Mencinger, 2004) and WCSPH solver (Wang, 2020).

The analytical configuration is illustrated in Figure 4.7, where a square solid is heated near the left wall to a temperature (T_h) above the melting temperature (T_m), resulting in the occurrence of the melting phenomenon. The right wall is maintained at the melting temperature, while the top and bottom walls are subjected to adiabatic thermal boundary conditions. The natural convection of the fluid was analyzed based on the Boussinesq assumption.

The flow conditions and fluid properties were set using non-dimensional numbers such as Prandtl (Pr), Rayleigh (Ra), and Stefan number (St). The detailed conditions are listed in Table 4.3. The material properties were assumed to remain constant before and after phase change.

The analysis results were compared and verified with previous studies regarding the position of the phase front and heat transfer characteristics at the hot wall surface. The location of the phase front and flow field for non-dimensional time t^* of 4.0, 10.0, 20.0 and 30.0 were presented in Fig. 4.8. The analysis results of the phase front location exhibited a similar trend to previous studies, as confirmed in Fig 4.9 where the contours of temperature field and phase front are shown.

After onset of melting, the transfer of energy occurs through conduction and convection. To investigate temporal evolution of the heat transfer mechanisms, the

Nusselt number was calculated. The averaged Nusselt number $(\overline{Nu})$ was measured at the hot wall surface. The local Nusselt number (Nu) was computed using Equation 4.9, and $\overline{Nu}$ was obtained using Equation 4.10.

$$Nu = \frac{dT}{dx}\Big|_{x=0} \tag{4.9}$$

$$f\overline{Nu} = \frac{1}{L}\int_0^L Nu(y)dy \tag{4.10}$$

As the liquid fraction increases within the analysis domain, the phase front and natural circulation position also shift towards the right, and the influence of heat transfer by natural convection increases. This trend is consistent with the results of previous studies, as shown in Figure 4.10. The increase in liquid fraction can also be observed in Figure. 4.11 and is consistent with the previous studies.

Through this analysis, it was confirmed that the proposed ISPH-based framework can accurately interpret laminar thermal flow and solid-liquid phase change analysis.

4.2.3 3D Thermal ablation with transition natural convection

To validate and verify integrated LES-SPH and phase change model, a 3D analysis of pure gallium melting with transitional natural convection was conducted. The analysis was based on the experiment by Gau(1986), and the schematic is depicted in Figure 4.12. The left wall is a high-temperature boundary, while the right wall maintains the initial temperature condition. The other walls form adiabatic conditions, and detailed material properties and initial conditions are summarized in Table 4.4.

■ **Sensitivity study on the particle size**

A sensitivity study was conducted to investigate the effect of particle size. Large particle size and kernel function length can lead to inaccurate heat transfer analysis. In order to determine the suitable particle size, the number of particles in the y-direction was used as a reference, and analyses were conducted for particle sizes of $L_y/20$, $L_y/40$, $L_y/60$, $L_y/80$ and $L_y/100$. The number and size of particles are summarized in Table 4.5. The convergence of the simulation results was verified based on (1) the position of the interface over time and (2) the liquid fraction.

Figure 4.13 to 4.15 illustrates the interface position at 125.0s, 225.0s and 325.0 with different spatial resolutions. It was confirmed that the sensitivity to particle size in terms of quantitatively assessing the convergence of the interface position was found to minor.

The liquid fraction for all analysis domain was calculated based on the initial volume of solid gallium as shown in Equation 4.11, where Lq, V_l, V_0, N_f, N_p and N_t denote liquid fraction, liquid gallium volume, initial gallium volume, number of fluid particles, number of particles undergoing phase change and number of total SPH particles. The number of particles undergoing phase change was calculated according to Equation 4.12, where subscript j represents particle undergoing phase change, and γ is porosity.

$$Lq(t) = \frac{V_l}{V_0} = \frac{N_f + N_p}{N_t} \tag{4.11}$$

$$N_p = \sum_j \gamma_j \tag{4.12}$$

The SPH simulation results and experimental correlation (Gau, 1986) for volume fraction at 325 seconds is shown in Figure. 4.16. The Gau's correlation is shown in Equation 4.13, where $\boldsymbol{\tau}$ and $\boldsymbol{A}$ denote non-dimensional time and aspect ratio which are defined in Equation 4.14 and 4.15.

$$\boldsymbol{Lq}(\boldsymbol{\tau}) = 2.708\boldsymbol{\tau}^{\mathbf{0.843}}\boldsymbol{Ra}^{0.0504}\boldsymbol{A}^{-0.14} \tag{4.13}$$

$$\boldsymbol{\tau} = \frac{\alpha t}{L_x^2}\frac{C_p(T_h - T_m)}{L} \tag{4.14}$$

$$A = L_z/L_x \tag{4.15}$$

It was observed that the SPH result exhibited a similar trend to the experimental correlation, and the liquid fraction converged rapidly after $L_y/60$. To assess the convergence of the liquid fraction over the time, the normalized liquid fraction was calculated. The normalized liquid fraction was computed as Equation 4.16 and presented in Figure. 4.17.

$$\overline{Lq}(t) = \frac{Lq(t)}{Lq(t = 325.0)} \tag{4.16}$$

For all cases, it was observed that the liquid fraction converges rapidly after $L_y/60$, and sensitivity to particle size decreased as analysis time progressed. These results can be attributed to the dominance of conduction in the early stage of the analysis, while the effect of natural convection became dominant in the later stage. At *t*=225.0s, 275.0s and 325.0s, there were cases where the normalized liquid fraction exceeded 1.0 at the $L_y/80$. However, these values were relatively small and didn't raise concerns about convergence. Therefore, in this study, to consider computational cost, the thermal analysis using the dynamic LES-SPH model was

performed with a resolution of $L_y/60$.

■ 3D Gallium thermal ablation simulation results

To validate the 3D gallium thermal ablation simulation using LES-SPH with phase change model, two parameters were investigated: 1) the temporal evolution of phase interface position at the gallium center plane ($y = 0.001905$ m) and 2) the temporal liquid fraction, both of which were compared and validated against the experimental data obtained by Gau (1986) at 120.0s, 180.0s, 360.0s, 480.0s, 600.0s 750.0s and 900.0s as shown in Figure 4.18. During the initial stage of the analysis ($t < 360.0$s), it was observed that the SPH results exhibited an excessive prediction of the gallium melting. This discrepancy can be attributed to the issue arising from the recognition of the particles slightly exceeding the enthalpy criterion for melting as fluid particles. On the other hands, as the analysis progressed and natural convection became more pronounced, leading to enhanced heat transfer, this discrepancy decreased. Figure 4.19 shows the particle porosity distribution at t=120.0s and t=900.0s prior to image rendering. In Figure 4.19(a), it can be confirmed that near the solid-liquid interface, there are three layer of particles which porosity is under 0.2, causing an overprediction of liquid phase boundary by approximately 2mm. The temporal liquid fraction is depicted in Figure 4.20. For each analysis time, the SPH analysis slightly overestimated the liquid fraction compared to the experimental results, however, this deviation was not significant.

In this chapter, the development and validation of SPH-based phase change model were performed, and it was confirmed that the integrated model with dynamic LES-SPH model accurately analyze phase change phenomenon accompanied by transitional thermal flow.

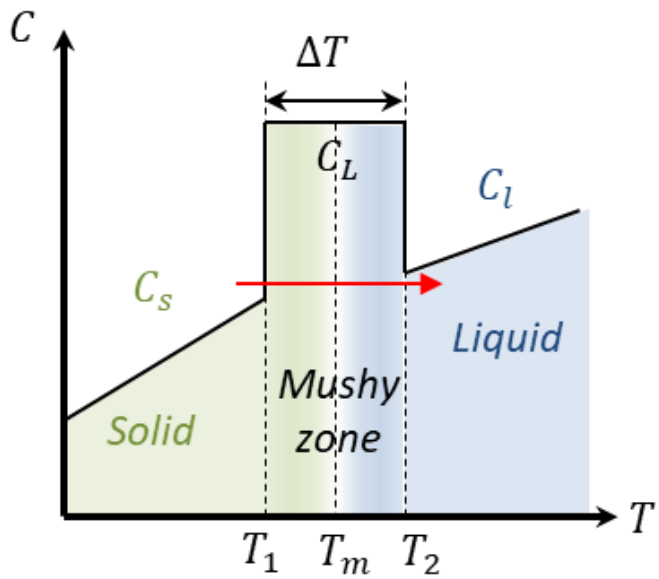

(a) A temperature-based phase change model

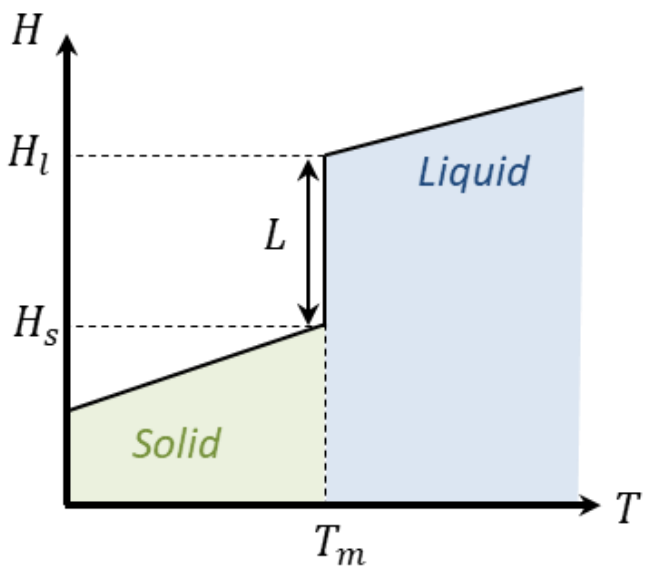

(b) An enthalpy-based phase change model

Figure 4.1. Phase Change Model

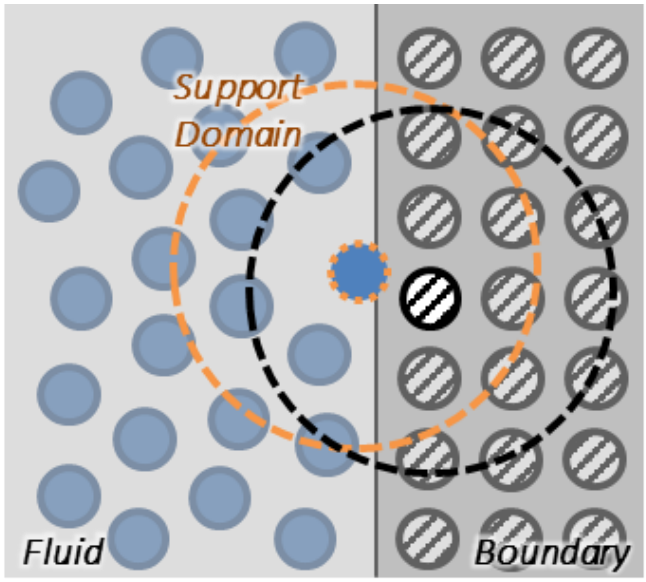

Figure 4.2. Compressed particle distribution near boundary

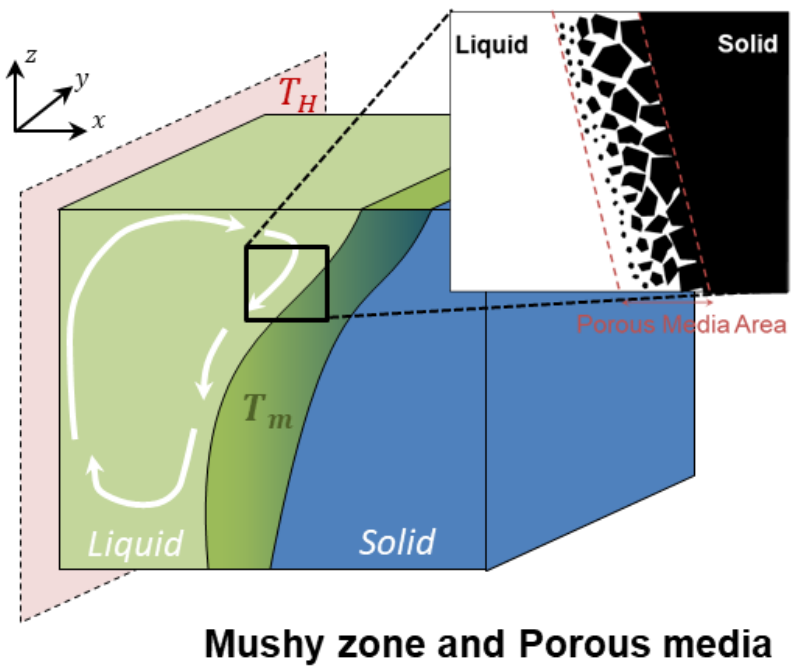

Figure 4.3. Mushy zone and porous media

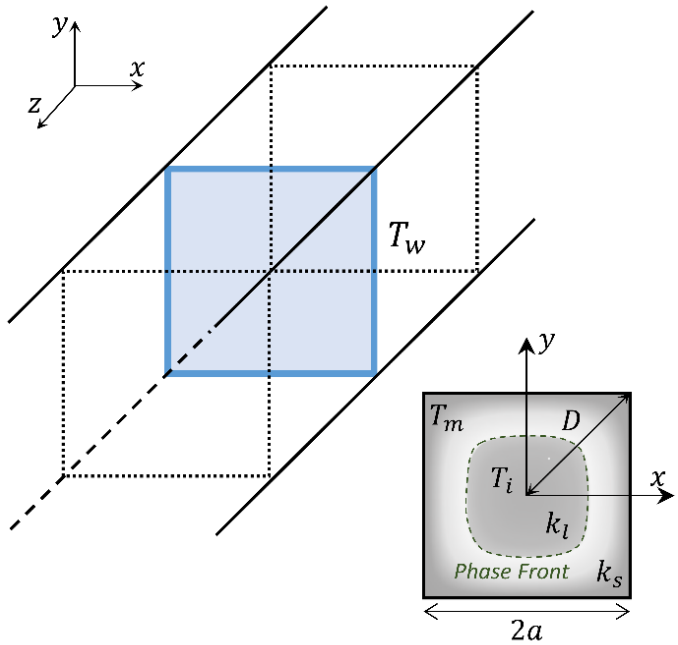

Figure 4.4. Schematic of 2D solidification simulation

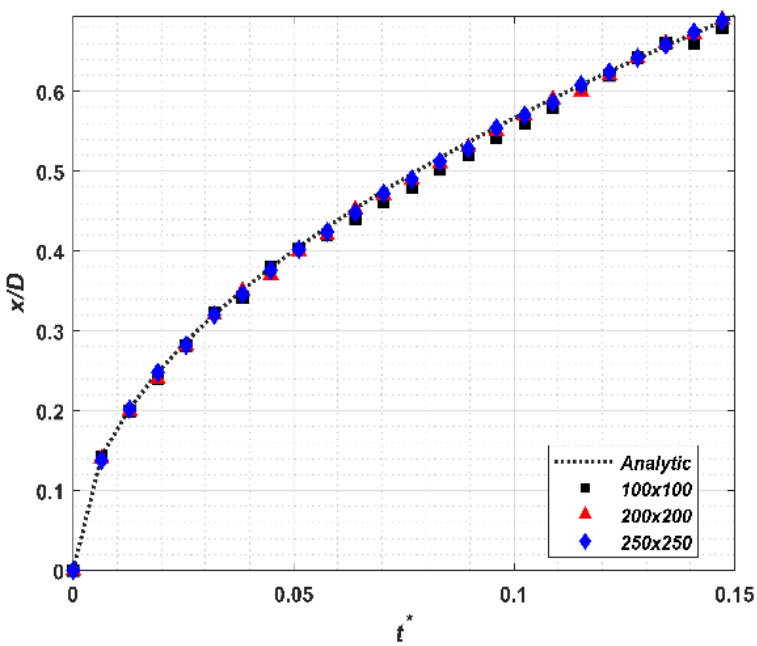

Figure 4.5. The position of phase front in diagonal direction

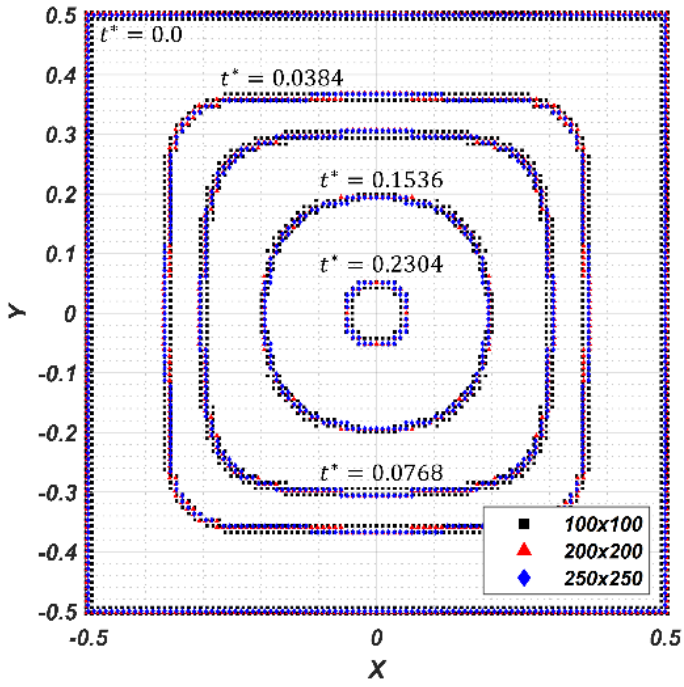

Figure 4.6. The position of phase front over time

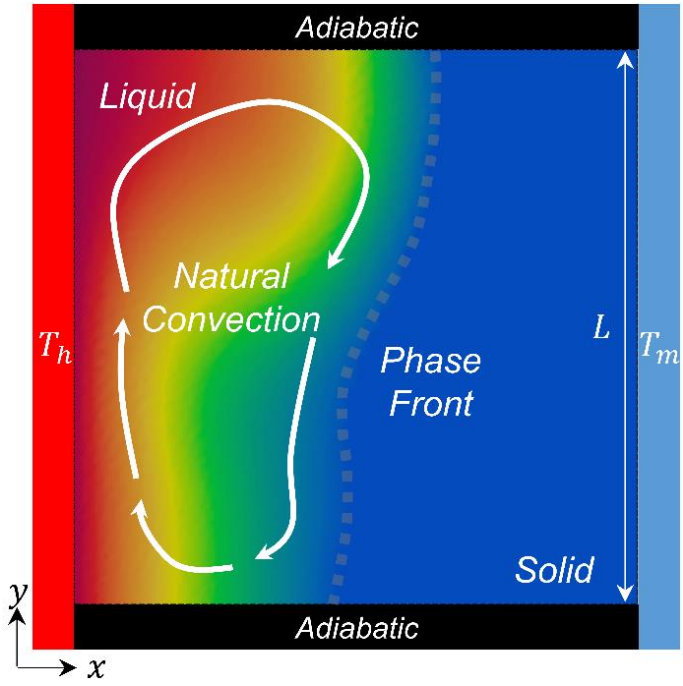

Figure 4.7. Schematic of 2D melting simulation

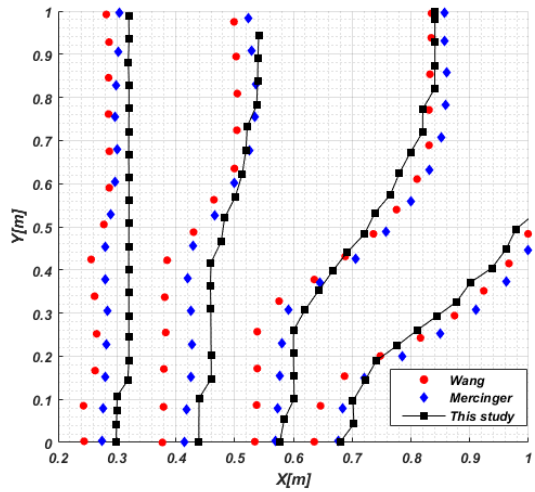

Figure 4.8. The position of phase front of 2D Melting Simulation

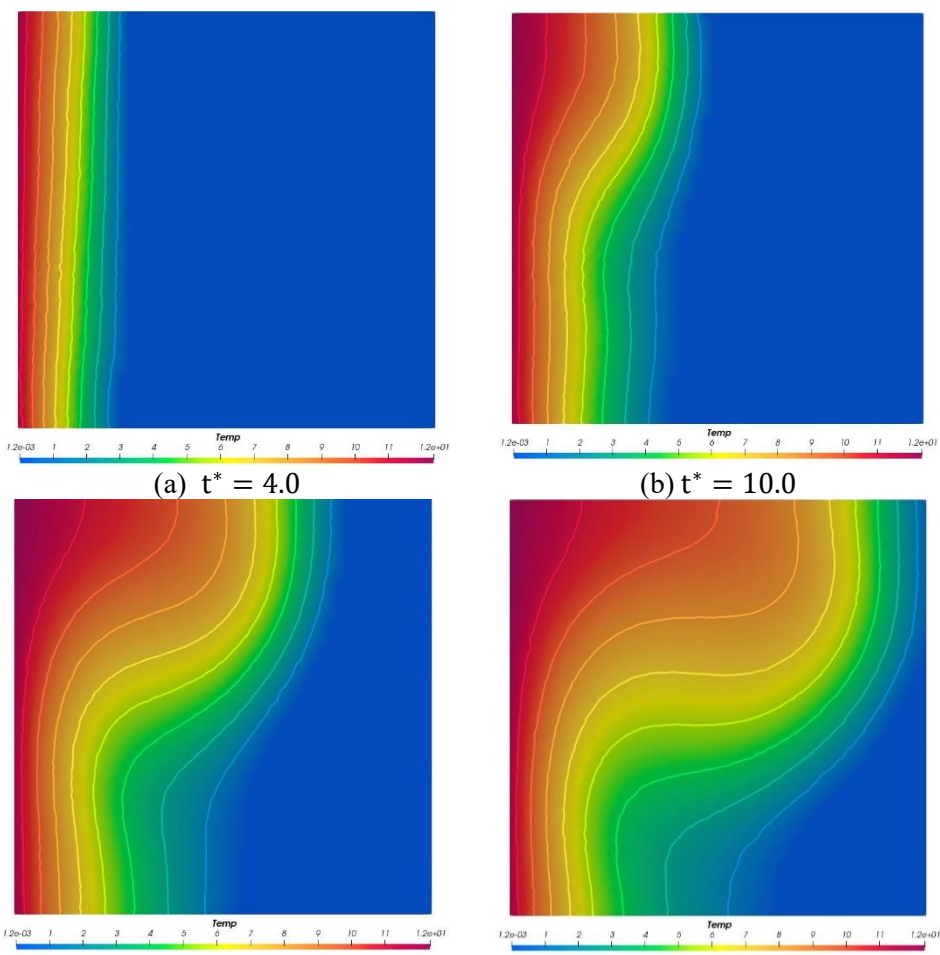

(a) $t^* = 4.0$ (b) $t^* = 10.0$

(c) $t^* = 20.0$ (d) $t^* = 30.0$

Figure. 4.9 Temperature distribution of 2D melting simulation

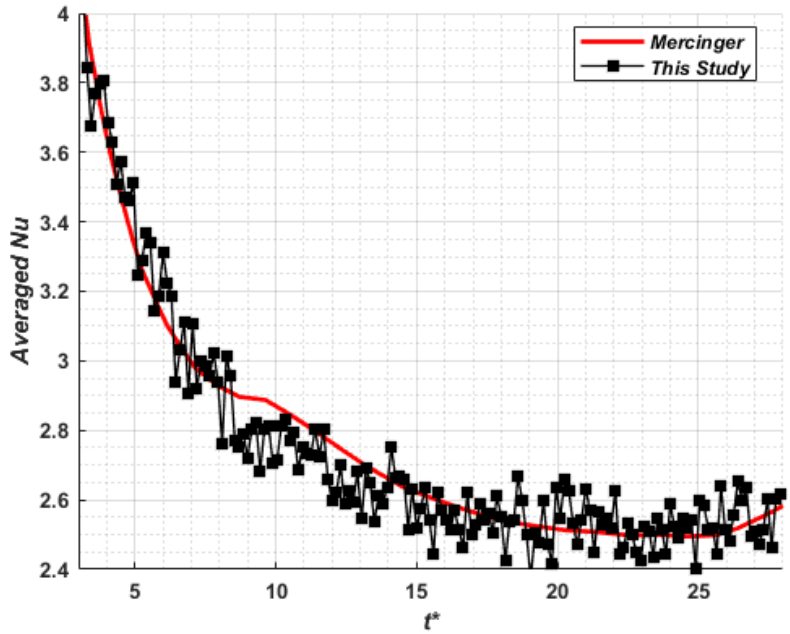

Figure 4.10. Averaged Nusselt number at hot wall surface

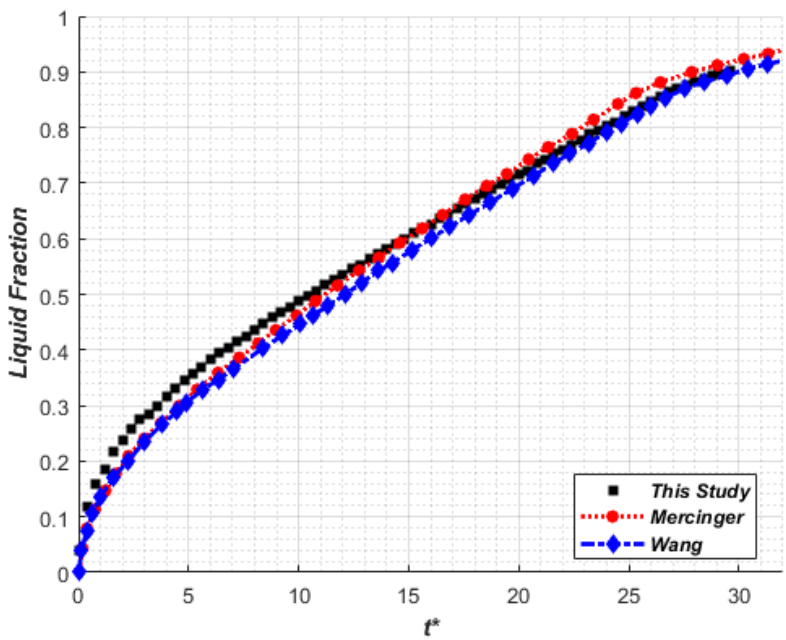

Figure 4.11. Liquid fraction in entire domain over time

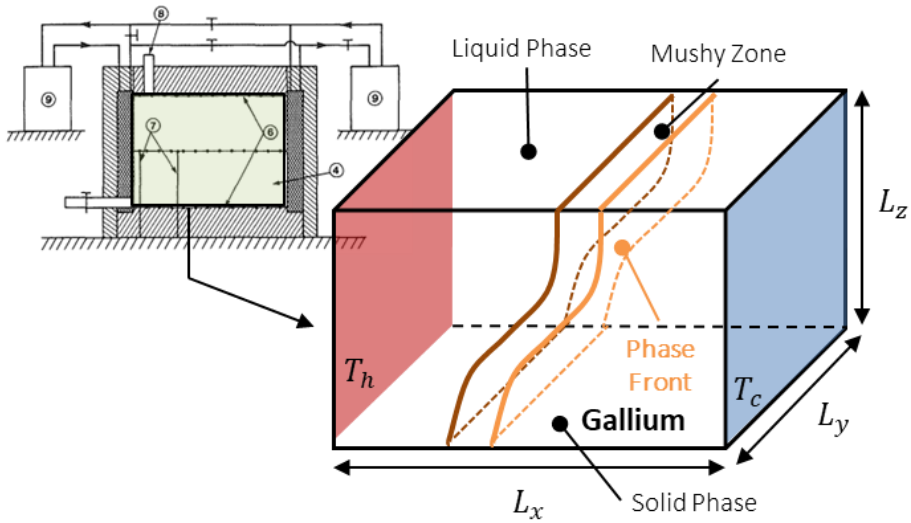

Figure 4.12. Schematic of gallium melting experiment

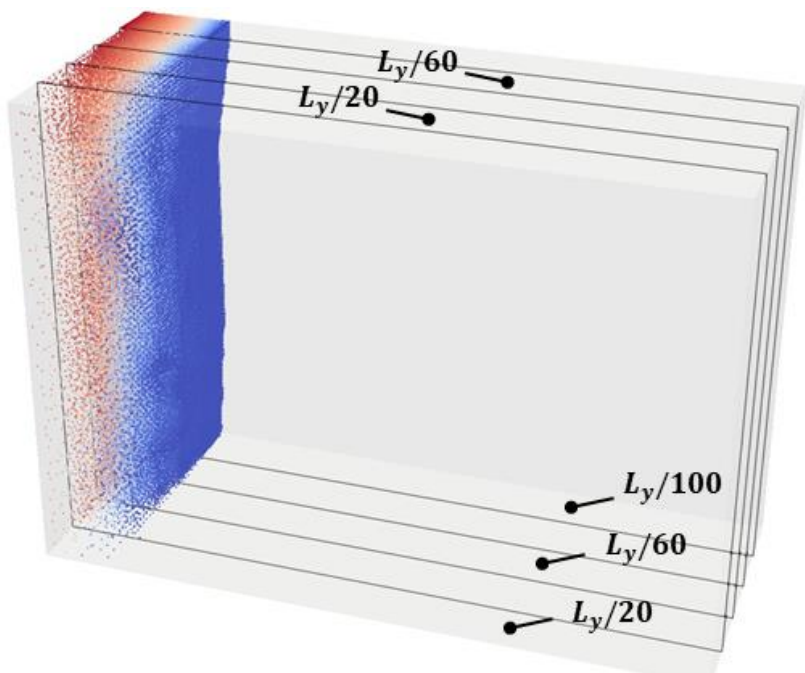

Figure 4.13. Phase interface at t=125.0 s with various resolutions

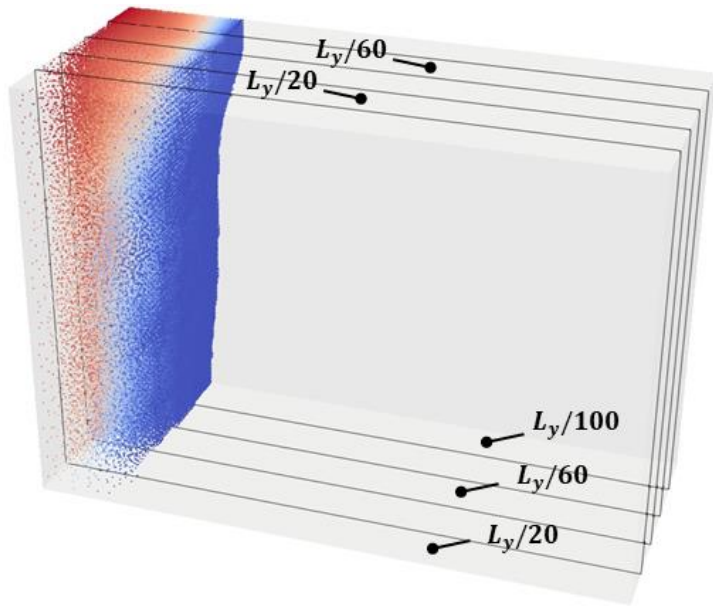

Figure 4.14. Phase interface at t=225.0 s with various resolutions

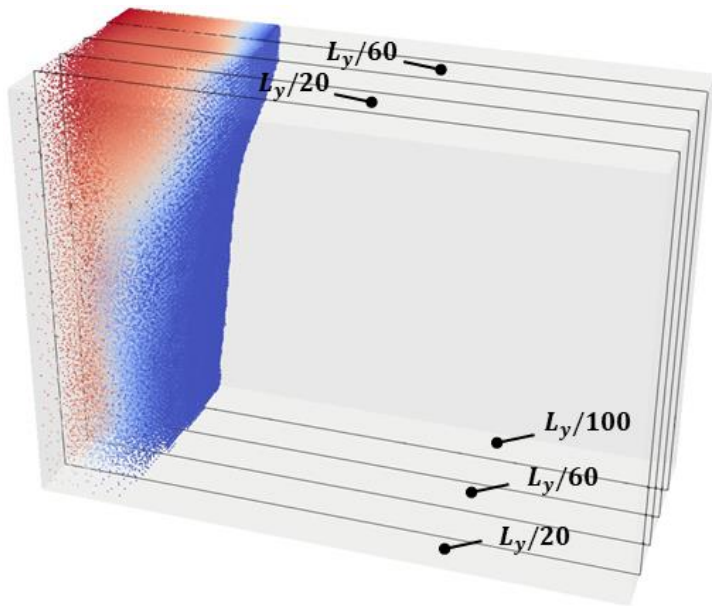

Figure 4.15. Phase interface at t=325.0 s with various resolutions

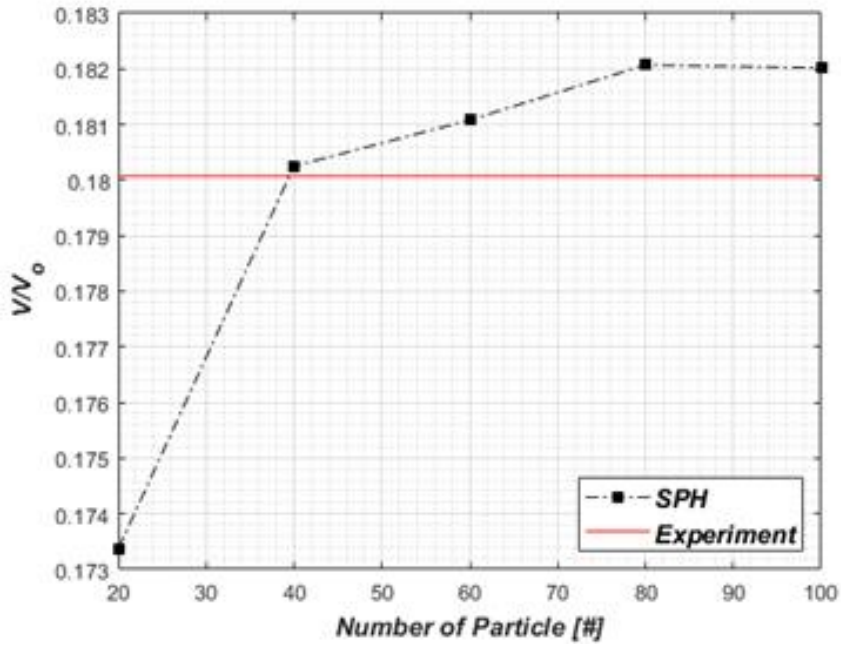

Figure 4.16. Liquid fraction at 325.s with various resolution

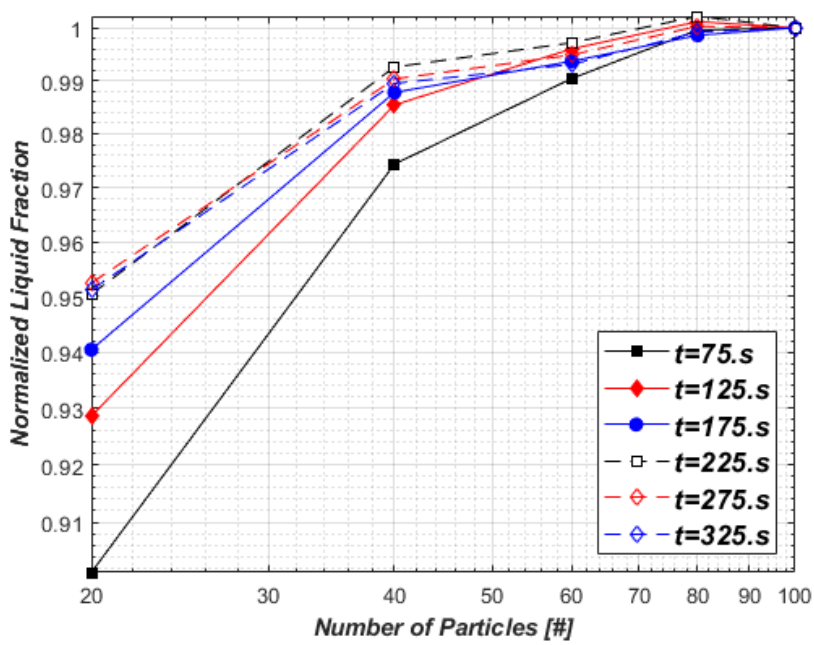

Figure 4.17. Normalized liquid fraction

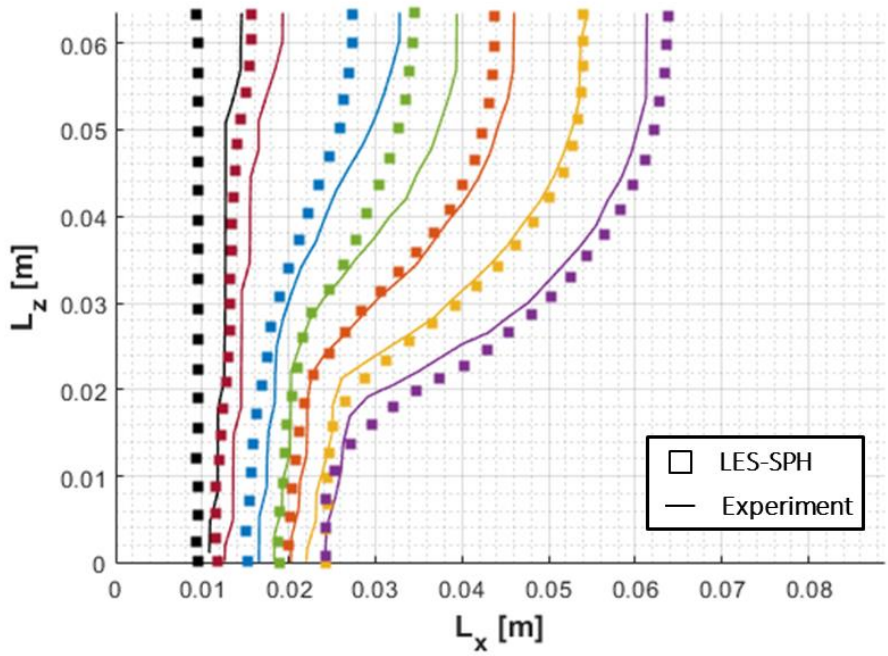

Figure 4.18. Phase interface position over time at 120.0s, 180.0s, 360.0s, 480.0s, 600.0s 750.0s and 900.0s

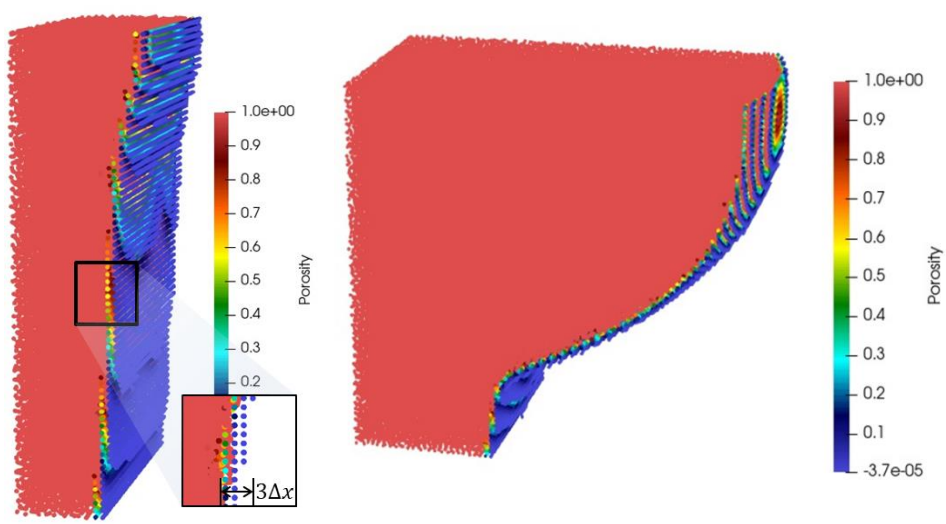

(a) t=120.0s (b) t=900.0s

Figure 4.19 Enthalpy-porosity distribution at each time step

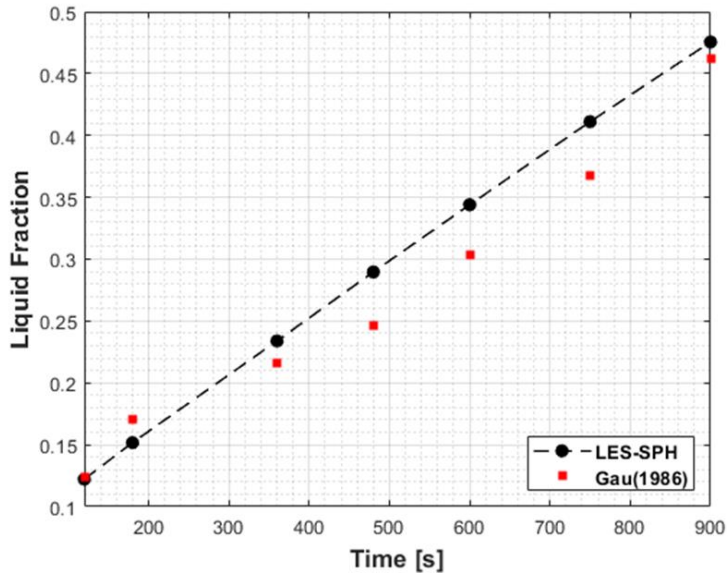

Figure 4.20. Total Liquid fraction over time

Table. 4.1. EPM application in projection step

	Momentum equation for EPM model
Projection Step	$\left\langle \frac{D(\boldsymbol{u^{pr}}-\boldsymbol{u^{n}})}{Dt} \right\rangle_i = \left(\frac{D\boldsymbol{u}}{Dt}\right)^{fv} + \left(\frac{D\boldsymbol{u}}{Dt}\right)^{fb} + \left(\frac{D\boldsymbol{u}}{Dt}\right)^{fpr}$ $\left(\frac{D\boldsymbol{u}}{Dt}\right)^{fpr} = -\frac{C(1-\gamma)^2\boldsymbol{u^{n}}}{\gamma^3}$
Correction Step	$\frac{(\boldsymbol{u^{n+1}}-\boldsymbol{u^{pr}})}{\Delta t} = \left(\frac{D\boldsymbol{u}}{Dt}\right)^{fp}$

Table. 4.2. EPM application in correction step

	Momentum equation for EPM model
Projection Step	$\left\langle \frac{D(\boldsymbol{u^{pr}}-\boldsymbol{u^{n}})}{Dt} \right\rangle_i = \left(\frac{D\boldsymbol{u}}{Dt}\right)^{fv} + \left(\frac{D\boldsymbol{u}}{Dt}\right)^{fb} + \left(\frac{D\boldsymbol{u}}{Dt}\right)^{fpr}$
Correction Step	$\frac{(\boldsymbol{u^{n+1}}-\boldsymbol{u^{pr}})}{\Delta t} = \left(\frac{D\boldsymbol{u}}{Dt}\right)^{fp} + \left(\frac{D\boldsymbol{u}}{Dt}\right)^{fpr}$ $\frac{(\boldsymbol{u^{n+1}}-\boldsymbol{u^{pr}})}{\Delta t} = \left(\frac{D\boldsymbol{u}}{Dt}\right)^{fp} - \frac{C(1-\gamma)^2\boldsymbol{u}^{n+1}}{\gamma^3}$ $\boldsymbol{u}^{n+1} = \frac{\boldsymbol{u}^{pr} + \left(\frac{D\boldsymbol{u}}{Dt}\right)^{fp}}{1 + \frac{\Delta t C(1-\gamma)^2}{\gamma^3}}$

Table. 4.3. Modeling conditions for 2D melting simulation

Parameter		**Value**	**Parameter**		**Value**
Pr		0.02	Ra		$2.5e+4$
C_p	$[J/kgK]$	$1.0e-4$	L_p	$[J/kg]$	0.125
β	$[K^{-1}]$	$1.0e-4$	ν	$[m^2/s]$	0.125
T_m	$[K]$	0.0	T_h	$[K]$	12.5
St		0.01	L	$[m]$	1.0
k	$[W/m \cdot K]$	$5.0e-4$	ρ	$[kg/m^3]$	1000.0

Table. 4.4. Simulation conditions for thermal ablation of gallium.

$\boldsymbol{L_x, L_y, L_z}$ $[\boldsymbol{cm}]$	(8.89, 3.81, 6.35)	$\mathbf{T_h, T_m, T_c}$ $[\boldsymbol{K}]$	(311.15, 303.00, 301.15)
$\boldsymbol{\rho}$ $[\boldsymbol{kg/m^3}]$	6093	$\boldsymbol{k}$ $[\boldsymbol{W/m \cdot K}]$	32.0
$\boldsymbol{L}$ $[\boldsymbol{J/kg}]$	80160	$\boldsymbol{C_p}$ $[\boldsymbol{J/kg \cdot K}]$	381.5
$\boldsymbol{\beta}$ $[\boldsymbol{1/K}]$	1.24	$\boldsymbol{\mu}$ $[\boldsymbol{kg/m \cdot s}]$	1.81×10^{-3}
SPH particle [#]	1,021,416	**particle Spacing** $[\boldsymbol{m}]$	6.35×10^{-4}
Time Step $[\boldsymbol{s}]$	5.0×10^{-4}	**Simulation Time** $[\boldsymbol{s}]$	900

Table. 4.5. Initial condition for sensitivity study

$\mathbf{L_y/\Delta x}$	$\mathbf{N_x}$ [#]	$\mathbf{N_y}$ [#]	$\mathbf{N_z}$ [#]	$\mathbf{\Delta x}$ [m]
20	47	20	34	1.90e-3
40	94	40	67	9.50e-4
60	140	60	100	6.35e-4
80	187	80	134	4.76e-4
100	234	100	167	3.81e-4

Chapter 5 Analysis of IVR-ERVC

The previous chapters focused on the development and validation of a dynamic LES-SPH model capable of analyzing thermal flow under various flow conditions. Additionally, advancements were achieved in the SPH-based phase change model and its integration was performed with the dynamic LES-SPH model. In this chapter, the integrated LES-SPH with phase change model is applied to analyze a severe accident scenario under Full-scale IVR-ERVC conditions.

5.1. Full-Scale Analysis of IVR-ERVC

The IVR-ERVC strategy was widely implemented as an effective means for maintaining the integrity during severe accident in low-power density reactors, such as AP600, AP1000 and SMART (Theofanous, 1996, 1997; Rempe, 2008). Recently, it has also been applied in high-power density reactor like AP1400 and the strategy feasibility has been investigated using MERCOR code (Lim, 2017).

This study focused on the APR1400 as the reference reactor and utilize the results of MELCOR analysis (Lim, 2017) as the initial simulation conditions. To analyze corium behavior and RPV ablation at wet cavity condition, the MARS-SPH coupling model was adopted which was developed by Park (2021).

5.1.1. Severe Accident Scenario

The accident scenario for analysis is based on the cold leg Large-Break Loss

Of Coolant Accident (LB LOCA) with full depressurization and without safety injection. The detailed chronology of the events is presented in Table 5.1. The scenario assumes the presence of a two-layer molten pool consisting of an oxide layer and light metal layer. The analysis of this study focused on the behavior of the stratified molten corium pool, and RPV ablation considering following assumptions:

- No SPH particle composition changes occur during the simulation due to chemical reaction or material diffusion.
- Mixing between the ablated RPV metal and the metal layer is not considered.
- Additional oxidation of the stratified corium layer and considerations regarding the heavy metal layer are omitted.
- RPV structural deformation caused by thermal loads or stress is not considered.

5.1.2. Initial Condition for IVR-ERVC

The analysis geometry consists of a hemispherical PRV with an inner radius of 2.37m, an outer radius of 2.58m, and a thickness of 0.1775m, as shown in Figure 5.1. The RPV was filled with molten oxide layer up to 1.89m from the bottom, and the metal layer is located above oxide layer with 0.47 m depth. The material properties for each layer are adopted from Carenini's study (2020), and detailed analysis conditions for the corium layers are summarized from Table 5.2 to 5.5. The initial condition for bulk temperature and decay heat of the corium pool are obtained from MELCOR analysis (Lim, 2017) results at 35,000 seconds when the peak corium temperature occurs, with *Ra* numbers of 4.9×10^{11} and 4.05×10^{16} for the metal and oxide layers, respectively.

5.1.3. Simulation Setup

The initial configuration was generated using SPH particles, as depicted in Figure 5.2. Full-scale simulation for the corium pool behavior in hemispherical RPV were performed, with particle sizes of $8 \times 10^{-3} m$ and a total number of $51{,}939{,}440$ particles. For the external cooling analysis, the MARS-SPH module developed by Park (2021) was employed. Further details of the MARS-SPH method was summarized in Appendix. A.

5.2. Results and Discussion

For the RPV cross-section, the extent of thermal ablation over time is depicted in Figure 5.3. As shown Figure 5.3(a), ablation occurs in RPV adjacent to the metal corium layer under the initial analysis conditions, and ablation occurs on the entire inner surface of the RPV in less than 1.0 second as shown Figure 5.3(b). This simulation result differs from the research by Park(2021), which analyzed the IVR-ERVC using the SPH based on the standard k-ε model. Park (2021) confirmed ablation occurring at about 800.0 seconds. This is because Park (2021) assumed the initial condition with lower temperature and decay heat compared to this study.

The behavior of ablated metal over time varies depending on the location of the ablation position. Molten metal from ablation on the RPV surface in contact with metal layer $(\mathrm{z} > 1.6534\mathrm{m})$ stratified between the metal and oxide layer due to density gradient. Ablated metal formed at RPV surface adjacent to the oxide layer remains in a phase change state until t=20.0s. It was observed to stay on the RPV surface due to the effect of EPM momentum sink term. Preliminary analyses at a lower spatial resolution w/o EPM showed that ablated metal formed in the region in contact with oxide layer rose and penetrated the corium pool due to buoyancy effects.

The shape of the ablated RPV at 18.0 seconds for the initial configuration is depicted in Figure. 5.4 and the total mass of ablated metal over time is shown in Figure 5.5. Despite the short analysis time, strong ablation was observed in the RPV adjacent to the metal layer due to the focusing effect.

In the light metal layer, a cold plume develops near the free surface due to radiative heat transfer as shown in Figure 5.6(a). Subsequently, natural convection accompanied by small-scale eddies occurs. However, as the low-temperature ablated metal infiltrates the lower part of the light metal layer, the temperature gradient in the upper and lower regions of the metal layer decreases significantly, leading to a reduction in the strength of natural convection in the outer region of the corium pool. This trend can also be observed by examining the temperature distribution on the bottom surface of light metal layer. Figure 5.7 demonstrates the temperature distribution of light metal layer at 5.0s, 10.0s and 17.5s, showing that the development of Benard cell region is reduced toward the center of corium pool.

Near the surface of oxide layer, cold plumes attempting to develop can be observed at t=20.0 as demonstrated in Figure 5.6(d). Although further investigation is required with longer simulation time, this phenomenon was not observed in the finding of Park (2021). Possible causes can be attributed to two main factors : 1) Differences arising from the initial condition of this study which temperature and decay heat are higher compared to Park (2021)'s study, and 2) underestimation of vertical heat transfer in the stratified corium pool due to the use of the Standard k-ε model, which does not account for the vertical direction of heat transfer accurately (Dinh, 1997), compared to the results of this study obtained by using .

The temperature fields over time are presented in Figure. 5.6. The oxide layer corium, cooled and descended on the curved RPV inner surface, undergoes stable stratification while maintaining a low-temperature, a high-density state on the

PRV bottom. During this process, the crust formation on the bottom can be observed.

By applying the dynamic LES-SPH with phase-change model, transient phenomena that were not observed in previous CFD studies were identified. The findings are as follows:

- It was observed that another liquid metal layer, which is formed from the thermal ablation of RPV, stratifies between the oxide and metal corium layer due to density gradient. Furthermore, this layer with low-temperature weakens the intensity of natural convection in the light metal layer.
- By utilizing the EPM to restrict the movement of particles undergoing phase-change, it was confirmed that the ablated metal formed near the oxide layer stagnates on the RPV surface. In the absence of the EPM model, the ablated metal can penetrate the oxide layer due to buoyancy effects, causing distortions in the turbulent heat transfer process.
- In the corium pool, transient changes of stratified corium interface were observed. The occurrence of a parabolic corium interface can be attributed to two main factors: 1) natural convection within the corium pool and 2) the formation of an ablated metal layer. Natural convection is induced by cooling at the ex-vessel and the decay heat from the oxide layer, resulting in a descending interface towards the outer periphery of the lower plenum. Moreover, the interface morphology undergoes changes due to the stratification of ablated metal from the RPV at the outer periphery of the lower plenum, between the oxide layer and metal layer. Additionally, the lower temperature of the ablated metal enhances the downwards flow of the oxide layer. These alterations in the corium interface should be considered when evaluating the inter-layer heat transfer mechanism.
- Lastly, the presence of crust formation on the bottom surface was confirmed, and through long-term analyses, it is expected to analyze the developmental process of the crust layer over time.

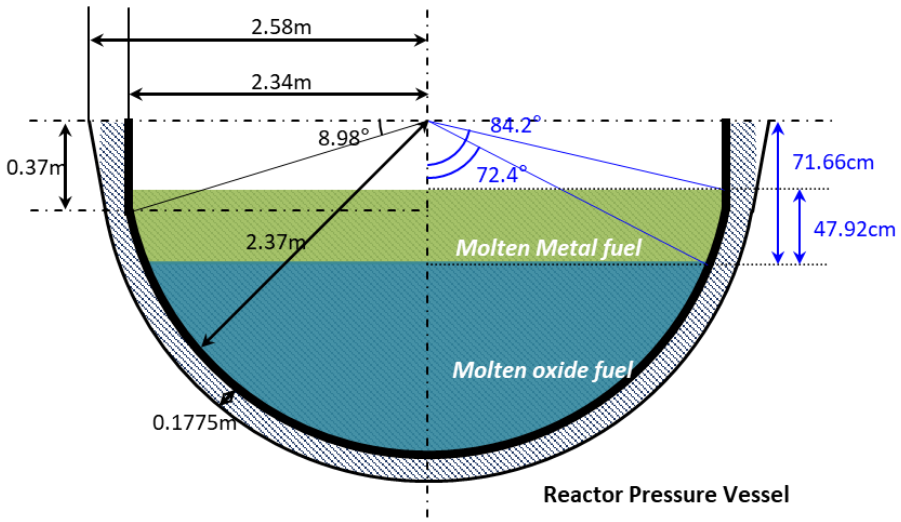

Figure 5.1. Initial configuration of IVR-ERVC simulation

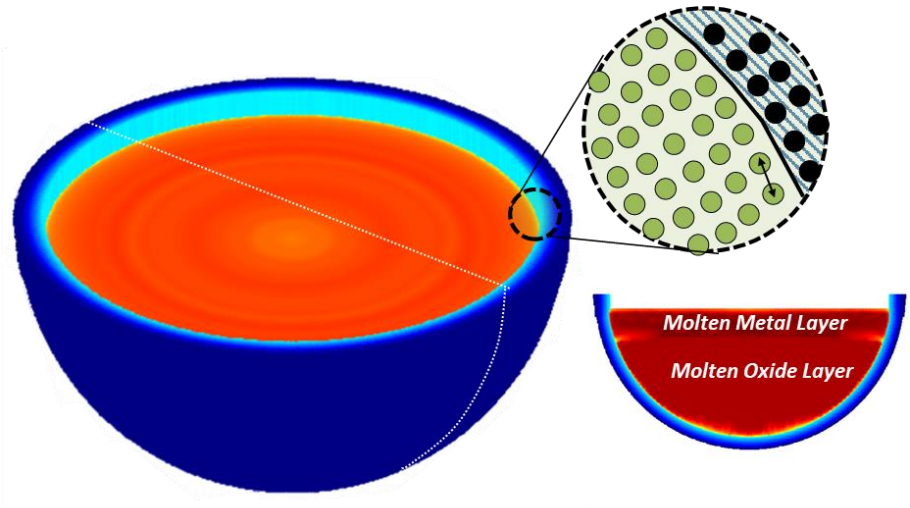

Figure 5.2. SPH input configuration for IVR-ERVC

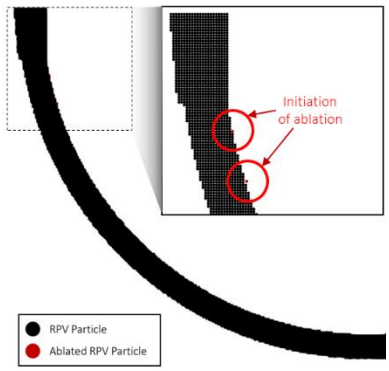

(a) t=0.0 s

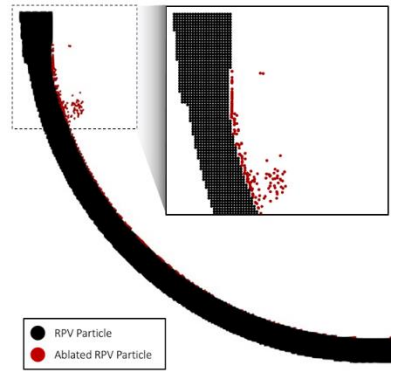

(b) t=4.0 s

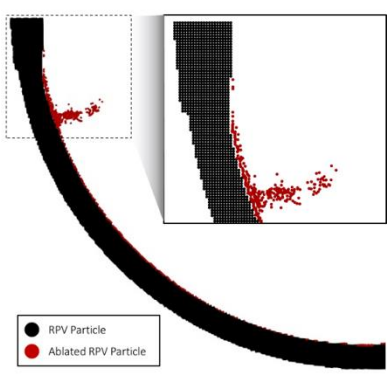

(c) t=8.0s

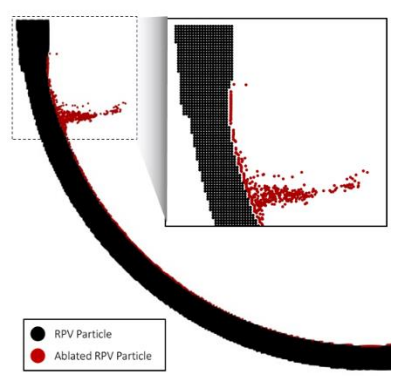

(d) t=12.0s

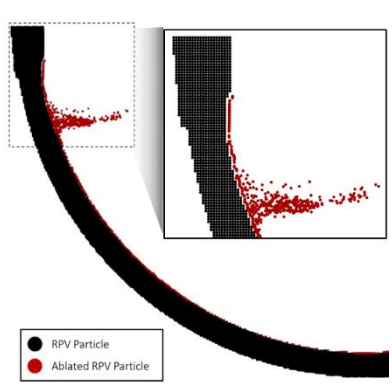

(e) t=16.0s

Figure 5.3. RPV and ablated metal behavior over time

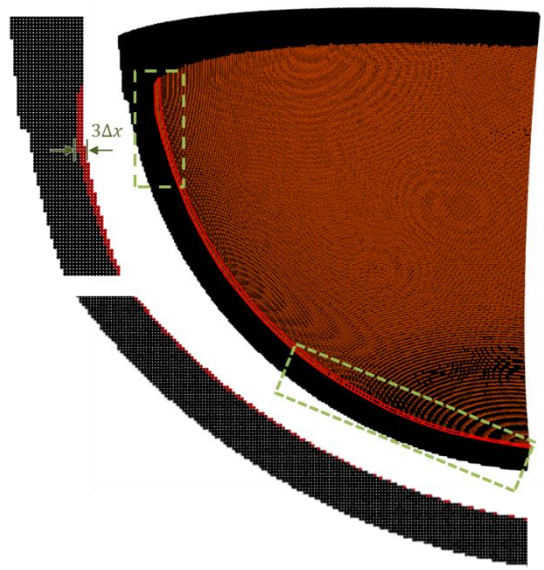

Figure 5.4. RPV configuration at 18.0 second
(Red particle : Ablated liquid metal, Black particle : Reactor pressure vessel)

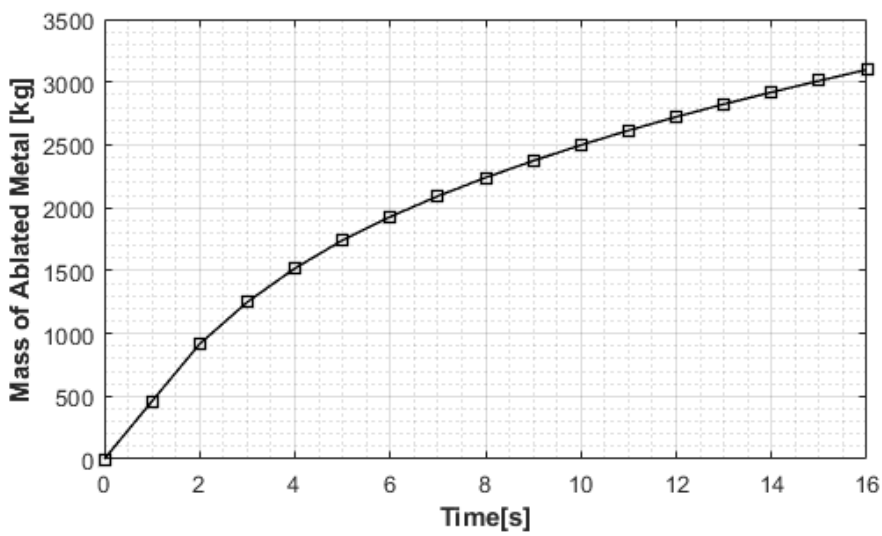

Figure 5.5. Total mass of ablated metal over time

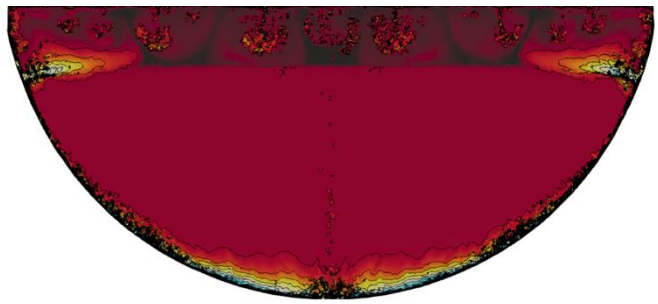

(a) t=5.0 second

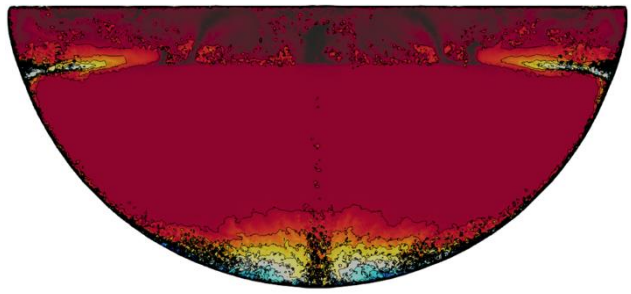

(b) t=10.0 second

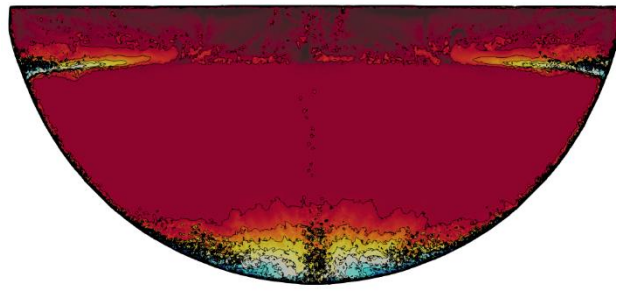

(c) t=15.0 second

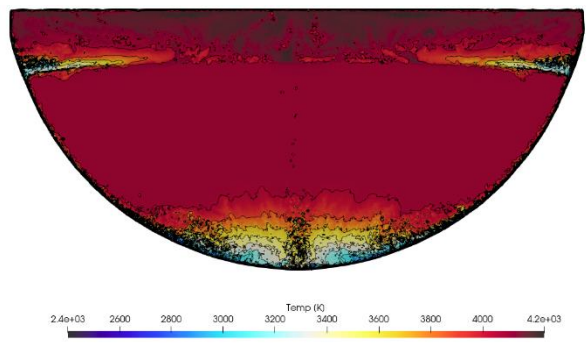

(d) t=20.0 second

Figure 5.6 Temperature distribution over time at x=0.0 m

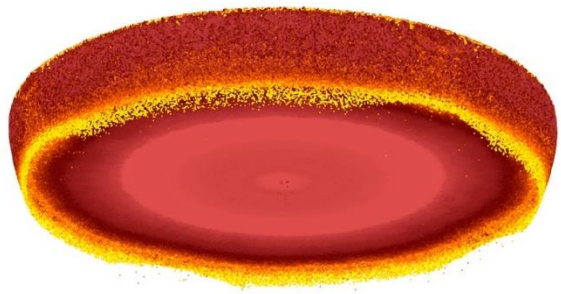

(a) t=5.0 second

(b) t=10.0 second

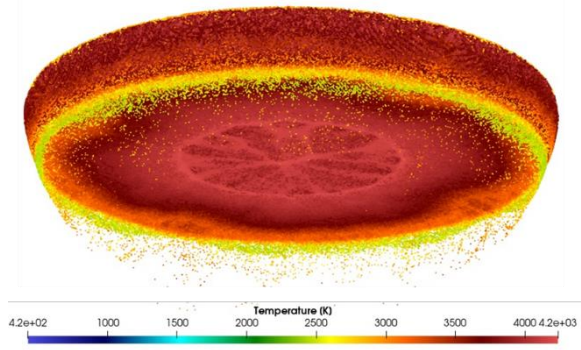

(c) t=16.5 second

Figure 5.7 Temperature distribution at the bottom of light metal layer

Table 5.1. Chronology of events in severe accident (Lim,2017)

Times [s]	Event
0.0	Occurrence of LOCA
0.5	Reactor trip
2.97	Start of core uncovering
10.02	Start of safety injection
92.7	Stop of safety injection
1358	Start of core support structure failure
2239	Start of fuel cladding melting
5584	Start of debris quench
5850	Core support plate failure
6920	Bottom plate failure
7430	ICI nozzle support plate failure
7610	Exhaustion of coolant in the reactor
8286	End of debris quench

Table 5.2. Material Properties of metal layer

Metal layer		
Density	kg/m^3	6899.2
Thermal conductivity	*W/mK*	25
Dynamic viscosity	m^2/s	4.07E-3
Specific heat capacity	*J/kgK*	789.5
Thermal expansion coefficient	*/K*	1.11E-4
Melting temperature	*K*	1778
Emissivity		0.4

Table 5.3. Initial condition of metal layer

Metal layer		
Volume	m^3	8.06
Depth	*m*	0.4792
Pool angle	*deg*	84.2
Bulk temperature	*K*	2934.3
Ra number		4.19E+11

Table 5.4. Material Properties of oxide layer

Oxide layer		
Density	kg/m^3	8191
Thermal conductivity	*W/mK*	5.3
Dynamic viscosity	m^2/s	4.67E-3
Specific heat capacity	*J/kgK*	533.2
Thermal expansion coefficient	*/K*	1.05E-4
Melting temperature	*K*	2950

Table 5.5. Initial condition of oxide layer

Oxide layer		
Volume	m^3	15.60
Depth	*m*	1.6534
Pool angle	*deg*	72.4
Volumetric heat generation	W/m^3	1.93E+06
Bulk temperature	*K*	3015.7
Ra number		4.05E+16

Chapter 6 Summary

6.1. Summary

In this study, a SPH based computational framework for analyzing thermal ablation accompanied by various natural convection conditions, ranging from laminar to turbulence, has been developed. An advanced Turbulence-SPH model based on the dynamic LES approach was developed and validated, considering integration feasibility with SPH and computational load. The phase change model for SPH was refined, verified and integrated with the turbulence-SPH model. To evaluate the performance and feasibility of the integrated model, an analysis of IVR-ERVC was performed under hypothesis severe accident scenario. The results, achievement, and findings of the study are summarized as follows.

1. Enhancement of computational efficiency and accuracy using the EISPH.

- A computational framework based on the explicit incompressible SPH was developed for saving computational cost and stable pressure field.
- Numerical corrections for SPH derivative discretization were introduced to improve analysis accuracy of momentum and energy transfer at boundary layer.

2. Development of the Turbulence-SPH model using the Dynamic LES approach.

- To analyze natural convection under various flow conditions ranging from laminar to turbulence with high *Ra* numbers, the dynamic LES-SPH was

developed.

- Considering the direct resolving capability for boundary layers, computational load, and integration feasibility with SPH method, dynamic Smagorinsky and dynamic Vreman model were selected, which is suitable for analyzing natural convection with highly stratified temperature and flow fields.
- SPH formulation method for the single/double filtering process in dynamic Smagorinsky and Vreman models was developed, and the filtering process was carried out based on the link-list NNPS method.
- The dynamic LES-SPH model was developed based on the EISPH solver, and turbulent Prandtl number modeling method was introduced for analyzing turbulent energy transfer of low Prandtl number fluids using the dynamic Smagorinsky model.
- Verification and performance evaluation of turbulence models regarding momentum and energy transfer in laminar, transitional and turbulent flows were conducted, and the accuracy of the dynamic Vreman model was confirmed.

3. Advanced EPM based SPH phase change model

- A fully explicit EPM-SPH model was developed to analyzing phase change phenomenon.
- The pressure field of particles in mushy zone was calculated stably by improving the pressure Poisson equation discretization method in EISPH solver.
- By adopting EPM-SPH phase change model, governing equations are formulated without numerical modification of particle physical properties such as viscosity and conductivity. The developed EPM-SPH model was integrated into the dynamic LES-SPH framework.

- The performance of phase change model was evaluated and validated against various numerical and experimental research, which is for phase change with accompanied by laminar and transitional thermal flow.

4. Analysis of IVR-ERVC using the integrated turbulent-SPH phase change model

- To verify the feasibility and applicability of the integrated SPH model, the behavior of corium pool and RPV ablation was analyzed for the scenario of a LB LOCA in a prototype APR1400.
- The thermal ablation of RPV was observed to occur from the beginning of the analysis in the vicinity of the metal layer, and RPV adjacent to the oxide layer was weakly ablated.
- The ablated metal infiltrates between the oxide and light metal layers due to the density gradient, leading to a transition from two-layer stratification to partial three-layer stratification.
- The formation of low-temperature ablated metal layer results in temperature gradient changes and variations in natural convection intensity.
- The composition change of corium pool and transient corium interlayer was identified due to the formation of ablated metal layer.
- By introducing the EPM, the upward movement of ablated metal in the oxide layer was restricted. The flow of ablated metal penetrating the oxide layer is expected to induce mixing phenomena within the oxide pool.

By utilizing the developed particle-based turbulence and phase change models, transient behavior of RPV ablation, corium pool and interface can be analyzed which has been challenging to conventional CFD. Furthermore, it is expected that this developed model will contribute to the analysis in various severe accident in the future.

6.2. Recommendation for Future Work

The dynamic LES-SPH model has been validated and verified for turbulent momentum and energy transfer through transition/turbulent lid-driven flow and turbulent Rayleigh-Benard convection, while validation for the laminar to turbulent or re-laminar transition processes and budget of turbulent intensity and heat flux was not performed. Therefore, additional validation and verification is planned to assess the performance of the dynamic LES-SPH model in the flow development process with transient flow characteristics. The validation plan is organized into two phases as depicted in Figure. 6.1. Phase 2 will primarily focus on the validation of the model's thermal flow analysis capability. Phase 3 will involve the utilization of the validated code to analyze experimental studies related to corium pool behavior and crust formation.

Validation Phase 2

In phase 2, the rigorous validation and verification of the dynamic LES-SPH model capability on the thermal flow analysis will be carried out through the following benchmark simulations.

Validation Phase 2.1. Heated Channel Flow

This benchmark involves turbulent flow in a channel with imposed heat flux at the top and bottom walls. In this benchmark, the dynamic LES-SPH code will be verified and validated on statistical variables such as turbulent kinetic intensity, Reynolds-averaged velocity, and time-averaged Nusselt number against previous DNS and LES analysis results. Additionally, the model's capability to analyze wall-normal turbulent heat flux and streamwise heat flux, which are critical for evaluating turbulent heat transfer characteristics in the boundary layer, will be assessed.

Furthermore, budget analysis of heat flux and temperature variance will be conducted for a comprehensive evaluation of the performance of the dynamic LES-SPH model.

Validation Phase 2.2. Tall cavity turbulent natural convection

The Tall Cavity Flow benchmark represents a flow configuration with two vertical boundary layers, one near the hot wall and one near the cold wall, in a highly stratified environment. The flow remains stagnant at the center of the cavity, while the upstream ends of the walls have thinner boundary layers that smoothly reattach the streamlines to the opposite wall, indicating re-laminarization. Downstream, recirculation zones form, disrupting the laminar boundary layers and leading to the ejection of large swirling eddies toward the center, resulting in intense mixing. The transition in the flow structure is evident in time-averaged dynamic LES simulation data, showing recirculation regions. Additionally, the expulsion of unsteady eddies along the walls enhances mixing and creates a highly stratified temperature distribution in the center of the cavity. By comparing and validating the results obtained from the LES-SPH code with previous LES and experimental results, the performance of the dynamic LES-SPH model for high Rayleigh number natural convection, which includes various flow conditions, can be assessed.

Validation Phase 3

Validation phase 3 aims to verify and validate the dynamic LES-SPH model through benchmark simulations of corium pool behavior under IVR-ERVC conditions.

Validation Phase 3.1. BALI Experiment

In severe accident, understanding the heat transfer characteristics and critical heat flux (CHF) limit in corium pools is crucial for corium retention and designing safety margins for the RPV. In this context, the BALI experiment was conducted employing a simulant fluid under the thermal condition of internal heat sources and constant wall temperature.

Measurements were performed to observe the lateral and upward heat transfer phenomena induced by natural convection at Rayleigh numbers ranging from 10^{15} to 10^{17} in a slice geometry. Correlation equations for heat transfer were proposed based on the experimental data. The dynamic LES-SPH analysis will be compared and validated against the temperature distribution along the depth and the heat transfer patterns at the upper and lateral surfaces with the experimental and numerical results.

Validation Phase 3.2. BALI Experiment

The LIVE-L4 experiment, conducted at FzK, aimed to understand the behavior of corium melt using a 3D hemispherical configuration. A simulant fluid consisting of KNO3-NaNO3 and water was used to mimic the corium behavior. The experiment focused on investigating the formation process of a crust layer on the RPV and the associated heat transfer phenomena.

Measurements were performed to observe the formation of a crust layer ranging from 11.7 mm to 70.7 mm on the surface of the RPV hemisphere. Additionally, the temperature distribution within the corium pool and the transient and steady-state heat transfer rates on the RPV wall were measured.

Through the analysis of the LIVE-L4 experiment using dynamic LES-SPH and phase change models, the validation of crust formation extent and heat transfer

characteristics towards the RPV under high Rayleigh number conditions will be performed.

Moreover, there are future plans to apply the dynamic LES-SPH model to IVR-ERVC conditions. Through the advanced understanding of thermal ablation of RPV and the behavior of the corium pool, it is expected to contribute to nuclear safety.

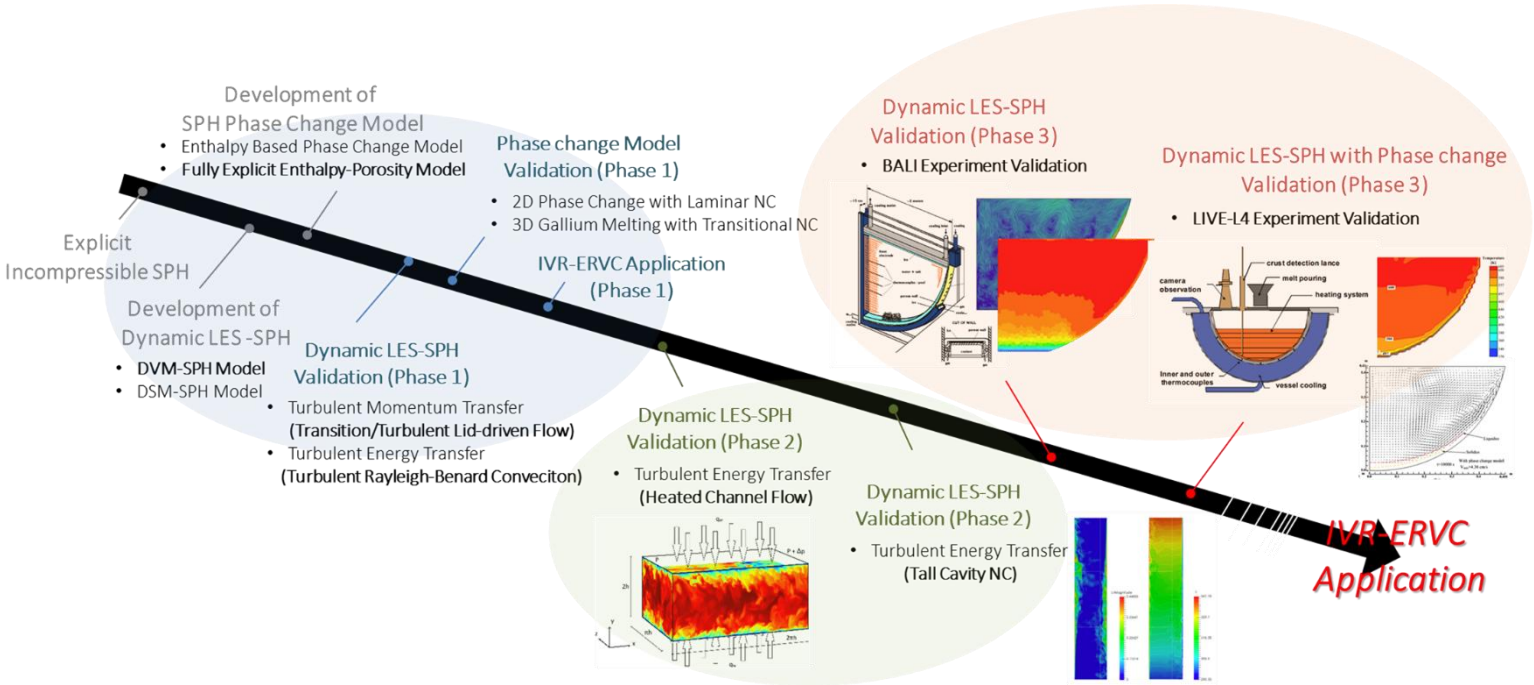

Figure. 6.1 Flow chart of Future work

References

Adami, S., Hu, X. Y., & Adams, N. A. (2012). A generalized wall boundary condition for smoothed particle hydrodynamics. *Journal of Computational Physics*, *231*(21), 7057-7075.

Amidu, M. A., Addad, Y., Lee, J. I., Kam, D. H., & Jeong, Y. H. (2021). Investigation of the pressure vessel lower head potential failure under IVR-ERVC condition during a severe accident scenario in APR1400 reactors. *Nuclear Engineering and Design*, *376*, 111107.

Aoki, S. (1963). A consideration on the heat transfer in liquid metal. *Bulletin of the Tokyo Institute of Technology*, (54).

Barcarolo, D. A. (2013). *Improvement of the precision and the efficiency of the SPH method: theoretical and numerical study* (Doctoral dissertation, Ecole Centrale de Nantes (ECN)).

Bonet, J., & Lok, T. S. (1999). Variational and momentum preservation aspects of smooth particle hydrodynamic formulations. *Computer Methods in applied mechanics and engineering*, *180*(1-2), 97-115.

Bonnet, J. M., Rouge, S., & Seiler, J. M. (1994). Large scale experiments for core melt retention: BALI: corium pool thermal hydraulics, SULTAN: boiling under natural convection.

Bouffanais, R., Deville, M. O., & Leriche, E. (2007). Large-eddy simulation of the flow in a lid-driven cubical cavity. Physics of Fluids, 19(5), 055108. https://doi.org/10.1063/1.2723153

Brent, A. D., Voller, V. R., & Reid, K. T. J. (1988). Enthalpy-porosity technique for modeling convection-diffusion phase change: application to the melting of a pure metal. *Numerical Heat Transfer, Part A Applications*, *13*(3), 297-318.

Carénini, L., Fichot, F., Bakouta, N., Filippov, A., Le Tellier, R., Viot, L., ... & Pandazis, P. (2020). Main outcomes from the IVR code benchmark performed in the European IVMR project. *Annals of Nuclear Energy*, *146*, 107612.

Chen, J. S., Pan, C., Wu, C. T., & Liu, W. K. (1996). Reproducing kernel particle methods for large deformation analysis of non-linear structures. *Computer methods in applied mechanics and engineering*, *139*(1-4), 195-227.

Cheng, X., & Tak, N. I. (2006). Investigation on turbulent heat transfer to lead–bismuth eutectic flows in circular tubes for nuclear applications. *Nuclear Engineering and Design*, *236*(4), 385-393.

Chiang, T. P., Sheu, W. H., & Hwang, R. R. (1998). Effect of Reynolds number on the eddy structure in a lid-driven cavity. International journal for numerical methods in fluids, 26(5), 557-579. https://doi.org/10.1002/(SICI)1097-0363(19980315)26:5<557::AID-FLD638>3.0.CO;2-R

Cummins, S. J., & Rudman, M. (1999). An SPH projection method. *Journal of computational physics*, *152*(2), 584-607

Cummins, S., Cleary, P. W., Delaney, G., Phua, A., Sinnott, M., Gunasegaram, D., & Davies, C. (2021). A coupled DEM/SPH computational model to simulate

microstructure evolution in Ti-6Al-4V laser powder bed fusion processes. *Metals*, *11*(6), 858.

Dalrymple, R. A., & Rogers, B. D. (2006). Numerical modeling of water waves with the SPH method. *Coastal engineering*, *53*(2-3), 141-147.

Daly, E., Grimaldi, S., & Bui, H. H. (2016). Explicit incompressible SPH algorithm for free-surface flow modelling: A comparison with weakly compressible schemes. *Advances in water resources*, *97*, 156-167.

Dinh, T. N., & Nourgaliev, R. R. (1997). Turbulence modelling for large volumetrically heated liquid pools. *Nuclear Engineering and Design*, *169*(1-3), 131-150.

Duan, G., Yamaji, A., & Sakai, M. (2022). A multiphase MPS method coupling fluid–solid interaction/phase-change models with application to debris remelting in reactor lower plenum. *Annals of Nuclear Energy*, *166*, 108697

Esmaili, H., & Khatib-Rahbar, M. (2004). Analysis of in-vessel retention and ex-vessel fuel coolant interaction for AP1000. Energy Research, Inc., ERI/NRC, 04-21.

Farrokhpanah, A., Bussmann, M., & Mostaghimi, J. (2017). New smoothed particle hydrodynamics (SPH) formulation for modeling heat conduction with solidification and melting. *Numerical Heat Transfer, Part B: Fundamentals*, *71*(4), 299-312.

Fatehi, R., & Manzari, M. T. (2011). Error estimation in smoothed particle hydrodynamics and a new scheme for second derivatives. Computers & Mathematics

with Applications, 61(2), 482-498. https://doi.org/10.1016/j.camwa.2010.11.028

Fichot, F., Carénini, L., Bakouta, N., Esmaili, H., Humphries, L., Laato, T., ... & Strizhov, V. (2020). Elaboration of a phenomena identification ranking table (PIRT) for the modelling of in-vessel retention. *Annals of Nuclear Energy*, *146*, 107617.

Fonty, T., Ferrand, M., Leroy, A., & Violeau, D. (2020). Air entrainment modeling in the SPH method: a two-phase mixture formulation with open boundaries. Flow, Turbulence and Combustion, 105(4), 1149-1195.

Gau, C., & Viskanta, R. (1986). Melting and solidification of a pure metal on a vertical wall

Germano, M., Piomelli, U., Moin, P., & Cabot, W. H. (1991). A dynamic subgrid-scale eddy viscosity model. Physics of Fluids A: Fluid Dynamics, 3(7), 1760-1765. https://doi.org/10.1063/1.857955

Gingold, R. A., & Monaghan, J. J. (1977). Smoothed particle hydrodynamics: theory and application to non-spherical stars. *Monthly notices of the royal astronomical society*, *181*(3), 375-389. https://doi.org/10.1093/mnras/181.3.375

Harish, R., Nimmagadda, R., & Reddy, S. R. (2022). Turbulent melting characteristics of hybrid nano-enhanced molten salt phase change material in rectangular enclosure. *Journal of Energy Storage, 54, 105328*

Hosseini, S. M., Manzari, M. T., & Hannani, S. K. (2007). A fully explicit three-step SPH algorithm for simulation of non-Newtonian fluid flow. *International Journal of Numerical Methods for Heat & Fluid Flow*, *17*(7), 715-735.

Huang, X. J., Li, Y. R., Zhang, L., & Hu, Y. P. (2018). Turbulent Rayleigh-Bénard convection in a cubical container filled with cold water near its maximum density. *International journal of heat and mass transfer*, *127*, 21-31.

Iwatsu, R., Ishii, K., Kawamura, T., Kuwahara, K., & Hyun, J. M. (1989). Numerical simulation of three-dimensional flow structure in a driven cavity. *Fluid Dynamics Research, 5(3), 173.*

Jeske, S. R., Bender, J., Bobzin, K., Heinemann, H., Jasutyn, K., Simon, M., ... & Reisgen, U. (2022). Application and benchmark of SPH for modeling the impact in thermal spraying. *Computational Particle Mechanics*, *9*(6), 1137-1152.

Jischa, M., & Rieke, H. B. (1979). About the prediction of turbulent Prandtl and Schmidt numbers from modeled transport equations. *International Journal of Heat and Mass Transfer*, *22*(11), 1547-1555.

Jo, Y. B., Park, S. H., Choi, H. Y., Jung, H. W., Kim, Y. J., & Kim, E. S. (2019). SOPHIA: Development of Lagrangian-based CFD code for nuclear thermal-hydraulics and safety applications. *Annals of Nuclear Energy*, *124*, 132-149.

KATO, Y., & TANAHASHI, T. (1992). Finite-Element Method for Three-Dimensional Incompressible Viscous Flow Using Simultaneous Relaxation of Velocity and Bernoulli Function: Flow in a Lid-Driven Cubic Cavity at Re= 5000. *JSME international journal. Ser. 2, Fluids engineering, heat transfer, power, combustion, thermophysical properties, 35(3), 346-353. https://doi.org/10.1299/jsmeb1988.35.3_346*

Kays, W. M. (1994). Turbulent Prandtl number. Where are we?. *ASME Journal of Heat Transfer*, *116*(2), 284-295.

Kays, W. M., Crawford, M. E., & Weigand, B. (1980). *Convective heat and mass transfer* (Vol. 4). New York: McGraw-Hill.

Kymäläinen, O., Tuomisto, H., Hongisto, O., & Theofanous, T. G. (1994). Heat flux distribution from a volumetrically heated pool with high Rayleigh number. *Nuclear Engineering and Design*, *149*(1-3), 401-408.

Leriche, E., & Gavrilakis, S. (2000). Direct numerical simulation of the flow in a lid-driven cubical cavity. *Physics of Fluids, 12(6), 1363-1376. https://doi.org/10.1063/1.870387*

Liang, H., Niu, J., & Gan, Y. (2020). Performance optimization for shell-and-tube PCM thermal energy storage. *Journal of Energy Storage*, *30*, 101421

Lim, K., Cho, Y., Whang, S., & Park, H. S. (2017). Evaluation of an IVR-ERVC strategy for a high power reactor using MELCOR 2.1. *Annals of Nuclear Energy*, *109*, 337-349.

Lind, S. J., Xu, R., Stansby, P. K., & Rogers, B. D. (2012). Incompressible smoothed particle hydrodynamics for free-surface flows: A generalized diffusion-based algorithm for stability and validations for impulsive flows and propagating waves. *Journal of Computational Physics, 231(4), 1499-1523. https://doi.org/10.1016/j.jcp.2011.10.027*

López, D., Marivela, R., & Garrote, L. (2010). Smoothed particle hydrodynamics model applied to hydraulic structures: a hydraulic jump test case. *Journal of*

Hydraulic Research, *48*(sup1), 142-158.

Mao, Z., Liu, G. R., & Dong, X. (2017). A comprehensive study on the parameters setting in smoothed particle hydrodynamics (SPH) method applied to hydrodynamics problems. *Computers and Geotechnics*, *92*, 77-95.

Mencinger, J. (2004). Numerical simulation of melting in two-dimensional cavity using adaptive grid. *Journal of Computational Physics*, *198*(1), 243-264.

Myong, H. K., Kasagi, N., & Hirata, M. (1989). Numerical prediction of turbulent pipe flow heat transfer for various Prandtl number fluids with the improved k-ε turbulence model. *JSME international journal. Ser. 2, Fluids engineering, heat transfer, power, combustion, thermophysical properties*, *32*(4), 613-622.

Najafabadi, M. F., Farhadi, M., & Rostami, H. T. (2022). Numerically analysis of a Phase-change Material in concentric double-pipe helical coil with turbulent flow as thermal storage unit in solar water heaters. *Journal of Energy Storage*, *55*, 105712.

Park, S. H. (2021). *Development of Lagrangian Particle-Based Methodology for In-Vessel Retention and External Reactor Vessel Cooling Application* (Doctoral dissertation, Ph. D. thesis], Seoul National University).

Prasad, A. K., & Koseff, J. R. (1989). Reynolds number and end-wall effects on a lid-driven cavity flow. *Physics of Fluids A: Fluid Dynamics, 1(2), 208-218. https://doi.org/10.1063/1.857491*

Ran, Q., Tong, J., Shao, S., Fu, X., & Xu, Y. (2015). Incompressible SPH scour model for movable bed dam break flows. *Advances in Water Resources*, *82*, 39-50.

Reynolds, A. J. (1975). The prediction of turbulent Prandtl and Schmidt numbers. *International Journal of heat and mass transfer*, *18*(9), 1055-1069.

Rogers, B. D., & Dalrymple, R. A. (2008). SPH modeling of tsunami waves. In *Advanced numerical models for simulating tsunami waves and runup* (pp. 75-100).

Russell, M. A., Souto-Iglesias, A., & Zohdi, T. (2018). Numerical simulation of Laser Fusion Additive Manufacturing processes using the SPH method. *Computer Methods in Applied Mechanics and Engineering, 341, 163-187.*

Samantaray, D., & Das, M. K. (2018). High Reynolds number incompressible turbulent flow inside a lid-driven cavity with multiple aspect ratios. *Physics of Fluids, 30(7), 075107.* https://doi.org/10.1063/1.5026662

Skillen, A., Lind, S., Stansby, P. K., & Rogers, B. D. (2013). Incompressible smoothed particle hydrodynamics (SPH) with reduced temporal noise and generalized Fickian smoothing applied to body–water slam and efficient wave–body interaction. *Computer Methods in Applied Mechanics and Engineering, 265, 163-173.* https://doi.org/10.1016/j.cma.2013.05.017

Smagorinsky, J. (1963). General circulation experiments with the primitive equations: *I. The basic experiment. Monthly weather review, 91(3), 99-164.* https://doi.org/10.1175/1520-0493(1963)091<0099:GCEWTP>2.3.CO;2

Tripepi, G., Aristodemo, F., Meringolo, D. D., Gurnari, L., & Filianoti, P. (2020). Hydrodynamic forces induced by a solitary wave interacting with a submerged square barrier: Physical tests and δ-LES-SPH simulations. *Coastal Engineering*, *158*, 103690.

Violeau, D., & Issa, R. (2007). Numerical modelling of complex turbulent free-surface flows with the SPH method: an overview. I*nternational Journal for Numerical Methods in Fluids, 53(2), 277-304. https://doi.org/10.1002/fld.1292*

Wang, J., & Zhang, X. (2020). Coupled solid-liquid phase change and thermal flow simulation by particle method. *International Communications in Heat and Mass Transfer*, *113*, 104519.

You, D., & Moin, P. (2007). A dynamic global-coefficient subgrid-scale eddy-viscosity model for large-eddy simulation in complex geometries. Physics of Fluids, 19(6), 065110. https://doi.org/10.1063/1.2739419

You, D., & Moin, P. (2009). A dynamic global-coefficient subgrid-scale model for large-eddy simulation of turbulent scalar transport in complex geometries. Physics of Fluids, 21(4), 045109. https://doi.org/10.1063/1.3115068

Zhang, G., Chen, J., Qi, Y., Li, J., & Xu, Q. (2021). Numerical simulation of landslide generated impulse waves using a δ+-LES-SPH model. *Advances in Water Resources*, *151*, 103890.

황석원, & 박현선. (2021). 가열 공동에서 자연 대류 유동에 대한 Dynamic Global-Coefficient 아격자 모델의 성능에 대한 수치 해석. *대한기계학회 논문집 B 권, 45(9), 487-491.*

Appendix. A.1 MARS-SPH Coupling for IVR-ERVC analysis

A.1.1. Introduction

To efficiently analyze the behavior of corium in RPV and ERVC, a coupling method between SPH and MARS was adopted which was developed by Park (2021). The MARS code allows for the individual component-wise analysis of reactor system and enables efficient ERVC analysis due to its inclusion of correlations for boiling heat transfer. As shown in Figure A.1.1, the corium flow within RPV is analyzed in detail using SPH code, while ERVC is analyzed using the system code.

A.1.2. MARS for External Reactor Vessel Cooling(ERVC) cooling

MARS code analyzes the coolant circulation and heat transfer rate between the reactor vessel wall and the insulator by considering the coolant flow rate, heat removal rate from the wall, coolant temperature and steam generation rate. To perform this analysis, node and junction structure are constructed as shown in Figure A.1.2.

The coolant circulation process is as follows: during a severe accident, coolant flows from IRWST to the cavity beneath the reactor vessel due to gravity (❼→❶). The coolant then flows through the inner channel between the reactor vessel and the insulation due to pressure gradient (❶→❷). As the coolant passes along the outer wall of RP, it heats up and undergoes boiling. The mixture of coolant and steam rises and passes through the upper venting damper (❷→❸→❹). Steam escapes to the free volume through the venting damper, while the coolant flows through the outer channel outside the insulation. (❹→❽ or ❺). The cooled coolant, with increased density, passes through the outer channel of the insulation and returns to the cavity. (❺→❻→❶).

To calculate heat transfer in the natural circulation loop, the Chen's correlation is utilized. The Chen's correlation consists of the Forster and Zuber correlation and the Dittus-Boelter correlation. Here, S and F represent the

suppression factor and Reynolds number factor. S represents the effective superheat of the wall's total superheat in nucleate boiling, while F is defined as the ratio of the two-phase Reynolds number to the liquid Reynolds number.

$$h = h_1 S + h_2 F \tag{A.1.1}$$

$$h_1 = 0.00122 \left(\frac{k_l^{0.79} C_{p,l}^{0.45} \rho_l^{0.49} g^{0.25}}{\sigma^{0.5} \mu_l^{0.29} h_{fg}^{0.25} \rho_g^{0.24}} \right) \Delta T_w^{0.24} \Delta P^{0.75} \tag{A.1.2}$$

$$h_2 = 0.023 Re_l^{0.8} Pr_l^{0.4} \frac{k_l}{D_e} \tag{A.1.3}$$

A.1.3. MARS-SPH Coupling Method

The MARS-SPH coupling is carried out using socket programming. Instead of directly connecting the SPH code and the MARS code, an interface code is utilized for data exchange, minimizing modification to the structure of each codes. The exchanged data between the coupling codes include the RPV outer temperature and heat flux.

To transfer information to the MARS code from SPH model, eight nodes (C220-1 to C240-2) are formed as thermal structures as shown in Figure A.1.3. The exchanged heat flux is determined by dividing the summation of the enthalpy change of the SPH particles near the thermal structure by the surface area of the nodes. Information exchange is performed considering the time step of SPH and MARS codes, with information exchange occurring every 100 time-step in the SPH code.

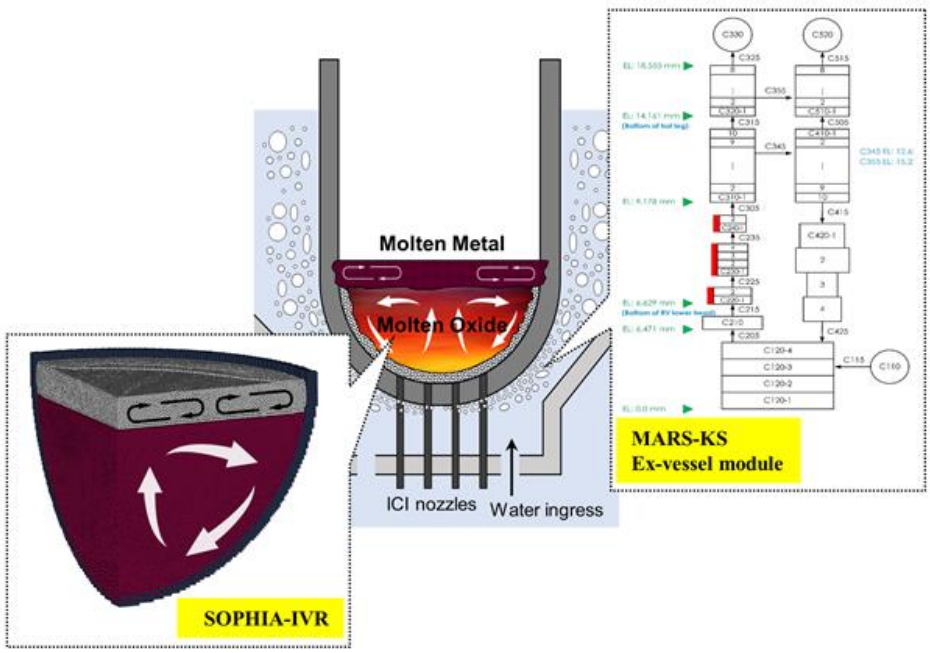

Figure. A.1.1. IVR-ERVC analysis with SPH-MARS coupling

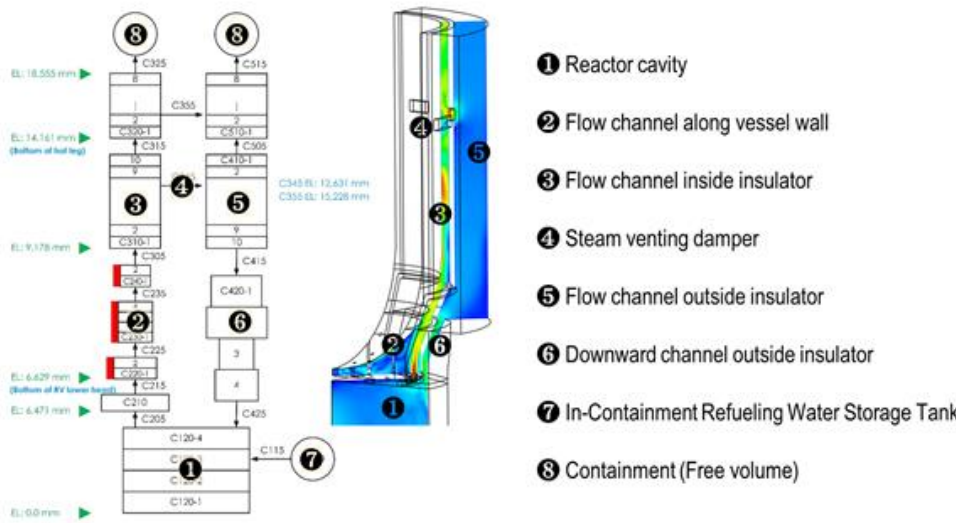

Figure.A.1.2. Node configuration of MARS-KS

국문초록

원자력 중대사고 완화전략에서는 노심용융물의 노내/노외에서의 효율적인 냉각을 통해 사고 진전 완화 및 핵분열물질의 유출방지를 목표로 한다. 그러나 노심용융물 붕괴열로 인해 압력경계의 열적 침식이 발생하며, 구조건전성로 인해 핵분열 생성물이 노외로 유출될 수 있다. 대표적인 사례로는 노내억류 전략에서 압력용기 용발, 노외억류 전략에서 MCCI 및 코어캐처 희생물질 열적 침식이 있다. 이때 압력경계의 열적 침식 정도는 노심용융물 열유동과 경계에서의 열유속에 의해 결정된다. 따라서 중대사고 완화 관점에서 열적 침식 현상과 상경계에서 노심용융물 거동에 대한 종합적인 이해가 필요하다. 그러나 극한 조건을 동반한 현상의 특징으로 인해, 실험적 해석에는 제한이 있고, 난류 자연대류를 동반한 노심용융물 거동, 고체-액체 상변화, 성층화된 노심용융물간 열유동 등의 거동 자체의 복잡성으로 인해 예측 및 평가에 불확실성이 존재한다.

노심용융물의 난류 자연대류 거동 및 압력경계 열적 침식 해석은 다른 중대사고와 마찬가지로, 모사실험 기반 경험적 접근 방식이나 성층화된 노심용융물 층의 유동특성을 고려한 전통적 전산 유체해석 방법론에 기반하였다. 노심용융물의 거동해석을 위해 고도화된 난류모델 개발 및 검증 연구가 진행되고 있으며, 최근에는 격자기반 상변화 해석을 포함한 종합적인 해석연구가 수행되었다. 이때 성층화된 노심용융물간 계면변화, 노심용융물의 자유표면 해석 및 상변화로 인한 해석영역의 변형 등의 영향을 모사하기 위해 수치적 가정들이 도입되었다.

한편, 최근 대규모 병렬계산을 위한 장비 및 소프트웨어의 발전에 힘입어, 입자법 기반 전산유체 해석 방법론이 원자력 안전 해석에 적

용하는 경우가 늘어나고 있다. 입자법은 격자 기반이 아닌, 물리량을 가진 입자의 움직임을 통해 유동을 해석하여, 다유체/다상 경계를 해석할 수 있으며, 상변화 및 자유표면을 다루는데 강점이 있다.

열적 침식 및 노심용융물 거동 관련 물리현상은 고체-액체 상변화현상으로 인한 해석계면 변형은 물론, 다물질 혼합물인 노심용융물 내에서 밀도차에 의한 성층화로 인한 다유체 열유동 해석등을 포함한다. 이러한 특징 때문에 입자법 기반 상변화 모델을 활용한 전산유체 해석방법론을 통해 효율적인 해석체계를 구축할 수 있다. 그러나 입자법 기반 전산유체 해석 방법론에서는 고도화된 난류모델을 통한 해석이 진행된 사례가 없으며, 따라서 난류 열유동을 동반한 열적 침식에 대한 해석 연구가 진행된 사례가 없다.

따라서, 본 연구에서는 대표적인 입자 기반 유체 해석 방법론인 완화입자유체동역학 (Smoothed Particle Hydrodynamics, SPH) 기반으로, 과도적인 층류, 전이 및 난류 유동 조건에 범용적으로 적용할 수 있는 난류모델을 개발하였다. 공간 가중함수를 활용하는 SPH 차분화 방법과, 공간 필터함수를 활용해 난류 유동 모델링을 수행하는 대와류모델 (Large Eddy Simulation, LES)의 공통점을 이용해, 추가적인 필터링 과정이 필요없는 LES-SPH 해석체계를 구축하였다. LES 모델의 수치 정확도 확보를 위해, SPH 차분화 수치 보정을 수행하였다. 또한 저 Pr 유체인 노심용융물 및 액체금속 열유동 해석을 위해, 난류 Pr수 모델링 및 동적 Vreman 모델을 도입하였다. 구축된 동적 LES-SPH 모델의 전이 및 난류 조건에서의 열유동 해석 능력 검증은 다양한 수치, 실험 연구들과 비교를 통해 수행되었다.

또한 양해법 SPH 해석체계를 활용한 열적 침식 해석을 위해, 엔탈피-다공성(Enthalpy-Porosity Model, EPM) 모델을 기반으로 상변화 모델을 고도화하였다. 상변화 구간에서 다공성 가정을 활용해 운동량 방정식

구성함으로써, 점성 등의 물성치에 대한 수치적 수정 없이 상변화 해석을 수행할 수 있다. 개발된 SPH 상변화 모델은 다양한 수치, 실험 연구와의 비교검증을 통해 상경계 및 열유동 해석 능력을 검증하였다.

마지막으로 개발된 LES-SPH 기반의 상변화 모델의 유용성 입증하기 위해 원자로 중대사고 완화전략인 노내억류 조건에서 노심용융물의 거동 및 압력용기의 열적 용발에 대한 해석을 수행하였다. 시간 및 위치에 따른 압력용기의 열적 용발 정도를 격자법 전산유체해석 방법론 및 선행 SPH 방법과 비교 검증하였다. 분석 결과, 본 연구에서 개발한 동적 LES-SPH 및 상변화 모델이 열적 침식을 동반한 난류 다유체 유동을 정성적으로 잘 해석하는 것을 확인하였다.

본 연구에서 개발한 입자법 기반 LES-SPH 상변화 해석체계는 원자로 중대사고 관점에서 기존 전산유체해석 기법을 통해 해석하기 어려웠던 현상들에 대한 직접 해석 방법론을 제안하였다는 의의가 있으며, 추후 전통적 유체해석 기법과 상호보완적 역할을 수행할 것으로 기대한다. 또한 개발된 LES-SPH 모델 및 상변화 모델에 대한 보다 엄밀한 검증 및 분석을 통해 신뢰성을 확보할 예정이다. 이를 통해 원자력 중대사고에서 실험결과가 없는 영역에 대한 상관식 개선 및 제안할 수 있으며, 원자력 안전 분야에 기여할 것으로 기대한다.

주요어 : 완화입자유체동역학, 동적 대와류 모델, 열적 침식, 상변화, 난류 모델, 상변화 모델, IVR-ERVC

학 번 : 2015-21333